

Raman imaging of carbon-based nano-materials and development of near-field Raman imaging techniques

You, Yu Meng

2009

You, Y. M. (2009). Raman imaging of carbon-based nano-materials and development of near-field raman imaging techniques. Raman imaging of carbon-based nano-materials and development of near-field raman imaging techniques.

<https://hdl.handle.net/10356/20867>

<https://doi.org/10.32657/10356/20867>



**NANYANG
TECHNOLOGICAL
UNIVERSITY**

**Raman imaging of carbon-based nano-materials
and development of near-field Raman imaging
techniques**

You YuMeng

School of Physical and Mathematical Sciences

2009

Raman imaging of carbon-based nano-materials and development of near-field Raman imaging techniques

You YuMeng

School of Physical and Mathematical Sciences

A thesis submitted to the Nanyang Technological University

in partial fulfillment of the requirement for the degree of

Doctor of Philosophy

2009

Acknowledgements

First of all, I would like to express my sincere gratitude and appreciation to my supervisors Prof. Shen Zexiang for his unfailing guidance and support throughout my PhD project.

Many thanks to all my colleagues, Dr Ni ZhenHua, Mr. Johnson Kasim, Dr Yu Ting, Ms. Ma Yun, Dr. Du ChaoLing, Mr. Zheng Zhe, Mr. Hu HaiLong, etc. from Raman Nanoscopy and Imaging Group, Division of Physics and Applied Physics of Nanyang Technological University, for their help during my PhD study.

Finally but most importantly, I would like to show my biggest thanks to my parents for their support and encouragement all the way.

Table of contents

Acknowledgements.....	ii
Table of contents.....	iii
Summary.....	vi
List of Figures.....	x
Publications.....	xvi

Chapter 1 Introduction

1.1 Motivation.....	1
1.1.1 Study on advanced Raman spectroscopy.....	1
1.1.2 Raman spectroscopy/imaging study on the carbon-based nano- materials.....	3
1.2 Objectives and significances of the studies.....	5
1.2.1 Study on advanced Raman spectroscopy.....	5
1.2.2 Raman study on carbon-based nano-materials.....	6

Chapter 2 Background and literature review

2.1 Raman spectroscopy and advanced Raman spectroscopy and imaging techniques.....	8
2.1.1 Raman spectroscopy.....	8
2.1.2 Surface enhanced Raman spectroscopy.....	13
2.1.3 Tip-enhanced Raman spectroscopy.....	20

2.1.4	Dielectric Microsphere-enhanced Raman spectroscopy/imaging.....	27
2.2	Carbon-based nano-materials.....	29
2.2.1	Carbon Nanotubes.....	29
2.2.2	Graphene.....	35

Chapter 3 SERS and TERS study of individual single crystalline silver nanowires

3.1	SERS study on individual single crystalline silver nanowires.....	41
3.1.1	Introduction.....	41
3.1.2	Experimental.....	42
3.1.3	Results and discussions.....	44
3.1.4	Conclusion.....	47
3.2	Tip-enhanced Raman scattering using individual single crystalline silver nanowire.....	47
3.2.1	Introduction.....	47
3.2.2	Preparation of NW attached TERS tip and experimental setup.....	50
3.2.3	Results and discussion.....	53
3.2.4	Conclusion.....	60

Chapter 4 Mechanically held microsphere-enhanced Raman spectroscopy and imaging

4.1	Introduction.....	62
4.2	Preliminary works.....	63
4.2.1	Experimental.....	64
4.2.2	Results and discussion.....	65
4.2.3	Conclusion of preliminary works.....	67
4.3	Raman enhancement study from mechanically held dielectric microspheres	67
4.3.1	Introduction.....	67

4.3.2	Attaching the sphere to the cantilever/tip.....	68
4.3.3	Microsphere-enhanced Raman imaging.....	73
4.4	Conclusion and future works.....	77
 Chapter 5 Visualization and investigation of Si-C covalent bonding of single carbon nanotube grown on silicon substrate		
5.1	Introduction.....	78
5.2	Experimental.....	79
5.3	Results and Discussions.....	83
5.4	Conclusion.....	89
 Chapter 6 Edge chirality determination of graphene by Raman spectroscopy and imaging		
6.1	Introduction.....	90
6.2	Experimental.....	94
6.3	Results and Discussions.....	94
6.4	Conclusion.....	101
 Chapter 7 Conclusion and future works		
7.1	Advanced Raman spectroscopy/imaging.....	102
7.2	Raman study on carbon related nanomaterials.....	103
7.3	Future work.....	104
 References		

Summary

This thesis presents the works I have accomplished in the period of my PhD study. The works can be divided into two parts: the first part is on the development of advanced near-field Raman spectroscopy/imaging techniques, and in the second part Raman imaging is used as a spectroscopic tool to study the carbon-based materials. The following is a summary of the two parts.

Part one

Being a conventional analysis tool widely used to probe the chemical and physical properties of materials, Raman spectroscopy is facing more and more challenges in modern researches featuring “nanometer-scale sciences and technologies”.

In my PhD work, we try to improve the conventional Raman spectroscopy/imaging technique from two aspects: the spatial resolution and signal intensity. Diffraction-limited spot size dictates that the laser spot size for Raman spectroscopy is in the order of 500nm which is far too big for the study of nano-devices and individual nano-materials such as nanowires (NWs). There are extensive works in recent years devoted to improve the spatial resolution to nanometer size but this field is still far from mature and there are still fundamental problems to overcome.

Due to its very small scattering cross section, Raman signal is intrinsically very weak which severely limits the applications of Raman scattering. The most promising method to improve the Raman signal is the surface enhanced Raman spectroscopy (SERS), which normally utilizes the effect induced by noble metal nanostructures. With

the help of the SERS effect, Raman signal enhancement can reach more than 10^{14} , which will allow even single molecule detection. We have studied the SERS effect from the individual silver NW. Our results show the great enhancement from the body of the wire, and first timely we observed the rapid enhancement from the apex of the NW. SERS experiments were carried out, as well as the numerical simulation by finite element method (FEM) using COMSOL MultiPhysics.

The enhancement from the apex of the NW inspired us to develop a new approach by using such method to carry out the tip-enhance Raman spectroscopy (TERS), also known as the apertureless scanning near-field optical microscope (apertureless-SNOM). In TERS, a sharp metal tip is brought very close to the sample surface, and incident laser can excite a very intensive localized electromagnetic (EM) field in the vicinity of the tip apex. The size of that EM field is in the same scale of the radius of curvature of the tip apex. By the help of the above effects, Raman signal can be greatly enhanced and the spatial resolution of conventional Raman imaging will also be dramatically improved. At the same time, TERS is bothered by several problems and is still one of the characterization techniques that are used by only a few in the research laboratories, as the experiments require very high degree of expertise and even though that the successful rate of TERS is still extremely low. In this thesis, our approach of using metal NW could overcome the problems of tip damaging and low repeatability in conventional TERS.

Besides the enhancement induced by the noble metal nanostructures, an alternative method using dielectric microspheres has also been invented by our group. With our experimental results and theoretical explanation, it is shown that the potential of such

dielectric microsphere-enhanced Raman spectroscopy/imaging technique in both high signal/noise ratio and spatial resolution. My contribution to this project is on the study of sphere holding method. The preliminary results of the microsphere-enhanced Raman imaging are also included in chapter 4.

Part two

Carbon has been considered one of the most important elements in nanometer-scaled materials. Besides the natural forms of carbon (diamond and graphite), nanometer-scaled forms (fullerene, carbon nanotubes and graphene) may be more valuable as the next generation materials.

Carbon nanotube (CNT) is a one-dimensional tubular nanostructure formed by wrapping up a single layer of graphite sheet. Single walled CNT (SWCNT) has a diameter ranging around 1 nm but whose length can be up to millimeter-scale. Such extreme aspect ratio and their unique sp^2 hybrid bonding bring it a lot of fascinating mechanical, chemical, physical, biological and electronic properties. By the help of those properties, CNT can be used as mechanical reinforcement materials, nano-resonator, advanced tip of atomic force microscope (AFM), field emission devices, gas sensing devices, drug delivery vessels, building block of the nano-electrical circuits, hydrogen storage, etc.

Theoretical study showed that by forming Si-C bonding between CNTs and the underlying Si substrate, the electronic properties of CNTs can be remarkably tuned. Thus, the realization of Si-CNT covalent bonding will benefit future applications of CNTs

devices. In this thesis, Raman imaging and spectroscopy are carried out to study the formation of the Si-C covalent bond between individual CNTs and silicon substrate. The results reveal that such Si-CNT was successfully synthesized, and our Raman imaging data first timely visualized such Si-CNT interaction.

As another nanometer-scale form of carbon, graphene is no doubt the most attractive material since its discovery in 2004. Such single layered carbon film with the atomic-scale thickness and area as large as millimeter-scale is favored for its extraordinary properties and applications in physics, chemistry, biology and electronics. In this part, Raman imaging of single layer micromechanical cleavage graphene (MCG) was carried out. The intensity of disorder-induced Raman feature (D band at $\sim 1350\text{ cm}^{-1}$) was found to be correlated to the edge chirality, e.g. zigzag or armchair: it is stronger at the armchair edge and weaker at the zigzag edge. This shows that Raman spectroscopy is a reliable and practical method to identify the chirality of graphene edge and hence the crystal orientation. The determination of graphene edge chirality is critically important for fundamental study of graphene as well as applications of graphene-based devices.

List of figures

- Figure 2.1 Diagram of the Raman scattering and Rayleigh scattering processes.
- Figure 2.2 Real part (left) and imaginary part (right) of the dielectric constant of gold, silver and copper.
- Figure 2.3 Calculated Raman enhancement of single metal nanoparticles in the function of excitation wavelength (energy)
- Figure 2.4 (a) Silver coated AFM tip. (b) Silver tip prepared by electrochemical etching.
- Figure 2.5 Experiment setup of TERS. (a) Back-reflection setup: the focused laser shines on the tip through a transparent substrate and excites the LSP. (b) Reflection mode: the incident laser illuminates the tip from side. (c) Top illumination setup: the incident laser is reflected by a parabolic mirror and shines on the tip.
- Figure 2.6 The near-field intensity distributions Photonic nanojets generated by illuminating a dielectric spheres with diameter of 1 μm .
- Figure 2.7 Diagram of CNTs rolling up by a piece of graphene sheet.
- Figure 2.8 A graphene lattice which forms a CNT by connecting point O and A, B and B'.
- Figure 2.9 A comparison of typical Raman spectra collected on graphene and CNT.
- Figure 3.1 (a) SEM image of as-prepared Ag NWs. (b) SEM image of a single crystalline Ag NW. The inset shows the zoom-in view of the apex of the wire. (c) TEM SAED pattern of individual Ag NW.

Figure 3.2 (a) and (c) are Raman images constructed by 4MBA Raman peak (located at 1591 cm^{-1}) with p-polarization and s-polarization, respectively. The white dash lines are guide for the eye showing the position of the NW. The white scale bar is $0.5\text{ }\mu\text{m}$. Comparison of FEM simulated field distribution in (b) p-polarization and (d) s-polarization. Please note the color scales are different for (b) and (d). (e) is the comparison of the Raman spectra collected at different positions with p-polarization. Figure (f) shows the simulation plot of the $|E_{\text{max}}|^4$ and FWHM of the localized EM field at the tip apex with p-polarization as a function of the function of the NW diameters.

Figure 3.3 (a) Illustration of the AC-DEP setup. (b), (c), SEM images of W tip with Ag NWs in different magnifications.

Figure 3.4 Schematic diagram of experiment setup for our TERS experiment.

Figure 3.5 Comparison of the Raman spectra. Tip in contact with sample surface with p-polarized incident laser (as red curve). Tip in contact with sample surface with s-polarized (as blue curve). Tip retracted about $1\text{ }\mu\text{m}$ from sample surface with p-polarized incident laser (as black curve).

Figure 3.6 Comparison between spectra obtained on bulk 4MBA molecule, TERS and SERS spectra on different spot of the Ag NW. All spectra are normalized by the Raman feature near 1590 cm^{-1} .

Figure 3.7 (a) An illustration of the approaching process. (b) A typical set of data collected while approaching sample towards the Ag NW tip. For a clear view, only data inside the far-field/near-field dominant region are plotted. (c)

Curve fitted Raman intensity of 4MBA Raman peak (1591 cm^{-1}) as a function of sample position. The black crosses are data obtained with tip in focus and the blue squares are data obtained with the absence of tip. The experiment data with tip is also fitted by function of exponential growth (red curve).

Figure 3.8 Comparison of spectra collected on the tip apex before and after a TERS approaching. The black curve is the spectrum collected on sample alone before the TERS experiment. The TERS spectrum obtained in the first approaching is shown in red color. Spectrum of the same Ag NW tip after the first approaching is shown in blue curve. Result acquired in second approaching is shown in purple color.

Figure 4.1 The schematic diagram of the microsphere enhanced Raman Spectroscopy (spheres trapped by optical tweezers)

Figure 4.2 The Raman spectra from (a) SiGe and (b) poly-Si lines with fitted peaks using Lorentzian function. In spectrum a, the Raman peak at 510.4 cm^{-1} corresponds to Si-Si phonon vibrations from SiGe, while the peaks at 518.9 and 520.6 cm^{-1} belong to tensile-strained Si just below the SiGe and the bulk Si substrate, respectively. In spectrum b, the Raman peaks at 516.3 , 520.6 and 522.1 cm^{-1} correspond to Si-Si phonon vibrations of poly-Si, bulk Si substrate and compressively strained Si in the channel region, respectively. (c) SEM image with cross-section view diagram of periodic tested structure. Line-profile of Raman Si-Si peak intensity from SiGe is

shown in yellow color, and the Si-Si peak position from the bulk Si is in purple color. The line scans show excellent correspondence with the structure.

Figure 4.3 Illustration of tailoring normal AFM tip by FIB.

Figure 4.4 Diagram of picking up microspheres by the W tip operated by nano-manipulators.

Figure 4.5 The sphere mounting process.

Figure 4.6 Optical images of the mounting process. Figure (a) and (b) show one microsphere is picked up by a W tip. (c) A W tip transferring a sphere to the end of the ATEC tip. The sphere attached (d) ATEC tip and (e) tailored AFM tip.

Figure 4.7 Spectrum collected on the as attached microsphere showing no obvious PL peak and no process induced Raman peak.

Figure 4.8 The cantilever holder is mounted on the objective lens. The cantilever can be moved by such holder in three directions under the microscope.

Figure 4.9 Illustration of the experiment setup. (a)The sphere mounted tailored AFM cantilever and (b) the sphere mounted ATEC tip.

Figure 4.10 Raman image constructed by intensity of Si peak (a) with using sphere attached cantilever and (b) without using any sphere. Both scale bars are 1 μm .

Figure 4.11 Illustration of the problem brought by the aperture on the cantilever.

Figure 5.1 The figures show the procedures of locating area of interests and the

correspondence of optical images and SEM images. Left column are SEM image with different magnification. Right column are optical images and Raman image constructed by G band intensity (lowest right figure) with different magnification. Same CNT in the SEM picture and Raman image is emphasized by dotted curves.

Figure 5.2 (a) SEM image showing an area of interest. Raman bands belonging to Si-C bonds can be detected on the CNT indicated by the dashed curve in red. (b) Comparison of Raman spectra obtained on normal CNTs (black spectrum), on the special CNT (red spectrum) and on bulk crystalline 4H SiC (blue spectrum). The dotted lines represent the CNT peak positions at the D band, G band and 2D band.

Figure 5.3 Raman images constructed using peak intensity of (a) G band of CNTs, (b) band I of Si-C at 1510 cm^{-1} , (c) band II of Si-C at 1692 cm^{-1} , (d) band III at 2392 cm^{-1} , and (e) band IV at 2620 cm^{-1} . The green arrow indicates the polarization of the incident laser. The blue dotted curves indicate the position and shape of the special CNT.

Figure 5.4 Polarized Raman spectra on the special CNT. Inset is the schematic of the configuration of the experiment.

Figure 5.5 Raman imaging with different incident polarization: (a) horizontal and (b) perpendicular. The blue dotted curves indicate the position and shape of the CNTs with Si-C bonds.

Figure 6.1 (a) Optical image of a typical MCG sheet and the angles between edges. (b)

The statistical results of the angle measurements. The standard deviation is 5.4° . (c) Illustration of the relationship between angles and the chirality of the adjacent edges.

Figure 6.2 Comparison of Raman spectra for different numbers of layers. (b) Zoom-in view of the Raman 2D band.

Figure 6.3 (a) Schematic illustration of the atomic structure of the armchair and zigzag edges and (b) first Brillouin zone of 2-D graphite, showing the double resonance mechanism for an armchair graphite edge.

Figure 6.4 (a) Raman image constructed by the intensity of G band with the expected arrangement in blue lines. Figure (b) and (c) are images constructed by the D band intensity with horizontal and vertical polarization, respectively. All images share the same scale bar as indicated in figure (b) which is $2\ \mu\text{m}$. (d) Raman spectra taken from edge 1 (spectrum a), and edge 2 (spectrum b), with horizontal laser polarization. Spectra c and d were also collected from edges 1 and 2 respectively, with vertical laser polarization. (e) The solid and dotted lines represent the D band intensity profile (solid/dash) plotted along the solid line on figure (b) and the dashed line on Figure (c), respectively.

Figure 6.4 Raman imaging results from edges with angles (a) 30° , (b) 60° (zigzag), (c) 90° and (d) 60° (armchair). The images constructed by the G band intensity show the positions and shapes of the SLG sheets. The laser polarization is indicated by the green arrows. The superimposed frameworks are guides for the eye indicating the edge chirality. Note that the edge chirality of (b) and

(d) were determined by the other pair of edges (not shown) with $30^\circ / 90^\circ$ on the same piece of SLG. The scale bar is $1\ \mu\text{m}$.

Publications

Publication in International Journals:

1. [You, Y. M.](#); Purnawirman; Kasim, J.; Yang, H. P.; Du, C. L.; Shen, Z. X.,
Tip-enhanced Raman spectroscopy using single-crystalline silver nanowire as tip.
(Journal of Raman spectroscopy, in press).
2. [You, Y. M.](#); Du, C. L.; Ma, Y.; Kasim, J.; Yu, T.; Shen, Z. X., Effect of near-field
coupling on far-field inelastic scattering imaging of gold nanoparticles.
Nanotechnology **2008**, 19, 395705.
3. [You, Y. M.](#); Ni, Z. H.; Yu, T.; Shen, Z. X., Edge chirality determination of graphene
by Raman spectroscopy. *Applied Physics Letters* **2008**, 93, 163112. Also selected for
the November 3, 2008 issue of *Virtual Journal of Nanoscale Science & Technology*.
4. [You, Y. M.](#); Yu, T.; Kasim, J.; Song, H.; Fan, X. F.; Ni, Z. H.; Cao, L. Z.; Jiang, H.;
Shen, D. Z.; Kuo, J.; Shen, Z. X., Visualization and investigation of Si-C covalent
bonding of single carbon nanotube grown on silicon substrate. *Applied Physics
Letters* **2008**, 93, 103111. Also selected for the September 22, 2008 issue of *Virtual
Journal of Nanoscale Science & Technology*.
5. Du, C. L.; [You, Y. M.](#); Zhang, X. J.; Kasim, J.; Shen, Z. X., Polarization-Dependent
Confocal Imaging of Individual Ag Nanorods and Nanoparticles, *Plasmonics*, **2009**,
published online.
6. Luo, Z. Q.; Yu, T.; Kim, K. J.; Ni, Z. H.; [You, Y. M.](#); Lim, S. H.; Shen, Z. X.; Wang,
S. Z.; Lin, J. Y., Thickness dependent reversible hydrogenation of graphene layers,
ACS NANO, **2009**, 3, 1781.

7. Yan, B.; Liao, L.; [You, Y. M.](#); Xiu, X. J.; Zheng, Z.; Shen, Z. X.; Ma, J.; Tong, L. M.; Yu, T., Single-crystalline V₂O₅ ultralong nanoribbon waveguides, *Advanced Materials*, **2009**, 21, 2436.
8. Yuan, S. N.; [You, Y. M.](#); Zhang, Q.; Shen, Z. X.; Gao, P. Q.; Shimamoto, D.; Endo, M., Correlation between in-situ Raman scattering and electrical conductance for an individual double-walled carbon nanotube. *Nano Letters*, **2008**, 9 (1), 383–387.
9. HJ Feng, YM Yang; [You, Y. M.](#), GP Li, J Guo, T Yu, ZX Shen, T Wu, BG Xing, Simple and Rapid Synthesis of Ultrathin Gold Nanowires, Their Self-Assembly and Application in Surface-Enhanced Raman Scattering. *Chemical Communication*, 15, 1984-1986.
10. Kasim, J.; Yu, T.; [You, Y. M.](#); Luo, J. P.; See, A.; Lee, L. J.; Shen, Z. X., Near-field Raman imaging using optically trapped dielectric microsphere. *Optics Express* **2008**, 16, 7976.
11. Ni, Z. H.; Wang, Y. Y.; Yu, T.; [You, Y. M.](#); Shen, Z. X., Reduction of Fermi velocity in folded graphene observed by resonance Raman spectroscopy. *Physical Review B* **2008**, 77, 235403.
12. Yu, T.; Ni, Z. H.; Du, C. L.; [You, Y. M.](#); Wang, Y. Y.; Shen, Z. X., Raman mapping investigation of graphene on transparent flexible substrate: The strain effect. *Journal of Physical Chemistry C* **2008**, 112, 12602.
13. Zheng, Z.; Yan, B.; Zhang, J.; [You, Y. M.](#); Lim, C. T.; Shen, Z. X.; Yu, T., Potassium tungsten bronze nanowires: Polarized micro-Raman scattering of individual nanowires and electron field emission from nanowire films. *Advanced Materials*

2008, 20, 352.

14. Du, C. L.; [You, Y. M.](#); Kasim, J.; Ni, Z. H.; Yu, T.; Wong, C. P.; Fan, H. M.; Shen, Z. X., Confocal white light reflection imaging for characterization of metal nanostructures. *Optics Communications* **2008**, 281, 5360.
15. Kasim, J.; Tee, X. Y.; [You, Y. M.](#); Ni, Z. H.; Setiawan, Y.; Lee, P. S.; Chan, L.; Shen, Z. X., Plasmon-enhanced polarized Raman spectroscopy for sensitive surface characterization. *Journal of Raman Spectroscopy* **2008**, 39, 1338.
16. Du, C. L.; Gu, Z. B.; [You, Y. M.](#); Kasim, J.; Yu, T.; Shen, Z. X.; Ni, Z. H.; Ma, Y.; Cheng, G. X.; Chen, Y. F., Resonant raman spectroscopy of (Mn,Co)-codoped ZnO films. *Journal of Applied Physics* **2008**, 103, 123515.
17. Luo, Z. Q.; Lim, S. H.; [You, Y. M.](#); Miao, J. M.; Gong, H.; Zhang, J. X.; Wang, S. Z.; Lin, J. Y.; Shen, Z. X., Effect of ion bombardment on the synthesis of vertically aligned single-walled carbon nanotubes by plasma-enhanced chemical vapor deposition. *Nanotechnology* **2008**, 19, 255607.
18. Ni, Z. H.; Fan, H. M.; Kasim, J.; [You, Y. M.](#); Feng, Y. P.; Han, M. Y.; Shen, Z. X., High pressure photoluminescence and Raman studies of $\text{Zn}_x\text{Cd}_{1-x}\text{Se}$ quantum dots. *Journal of Physics-Condensed Matter* **2008**, 20, 325214.

Manuscripts submitted/in press:

18. UK patent on the Raman enhance technique. (Under processing.)

Conference publication:

1. International Conference on Materials for Advanced Technologies, 2009, Singapore

Oral presentation “Edge Chirality Determination of Graphene by Raman Spectroscopy”

You, Y. M.; Ni, Z. H.; Yu, T.; Shen, Z. X.

Poster “From Surface Enhanced Raman Spectroscopy (SERS) to Tip Enhanced Raman Scattering (TERS): A Raman Enhancement Study Using Individual Single-crystalline Silver Nanowires” **Best Poster Award** in the symposium of “Plasmonics and Applications”.

You, Y. M.; Purnawirman; Kasim, J.; Yang, H. P.; Du, C. L.; Shen, Z. X.
2. MRS Fall Meeting 2008, Materials Research Society, Boston, U. S.

Oral presentation “From Surface Enhanced Raman Spectroscopy (SERS) to Tip Enhanced Raman Scattering (TERS): A Raman Enhancement Study Using Individual Single-crystalline Silver Nanowires”

You, Y. M.; Purnawirman; Kasim, J.; Yang, H. P.; Du, C. L.; Shen, Z. X.
3. 4th International Conference on Materials for Advanced Technologies, 2007, Singapore

Poster “Study of Raman spectroscopy enhancement on isolated metal nano-particles and metal nano-particles assemblies”

You, Y. M.; Pan, H.; Shen, Z. X.
4. Workshop on Nanoscale Spectroscopy and Nanotechnology, 2007, Kasetsart University, Bangkok, Thailand.

Invited talk on “Raman and Photoluminescence imaging of Gold Nano- Particles and

Hot Spots” and “Raman Imaging of Carbon Nanotube and Related Materials”

You, Y. M.; Du, C. L.; Ni, Z. H.; Kasim, J.; Yu, T.; Shen, Z. X.

5. 3rd International Conference on Materials for Advanced Technologies, 2005,
Singapore

Oral presentation “Raman microscopy and mapping of relaxed SiGe/Si
heterostructures”

You, Y. M.; Shen, Z. X.; Zhang, Z.; TOK, E. S.

6. 13th National Conference on Light Scattering in China, 24~27 October 2005,
Shanghai, China

Oral presentation “Raman microscopy and mapping of relaxed SiGe/Si
heterostructures with different excitation laser wavelength”

You, Y. M.; Shen, Z. X.; Zhang, Z.; TOK, E. S.

Chapter 1

Introduction

General introduction

After decade's development, Raman spectroscopy is now one of the routine spectral tools for its non-destructive, minimum sample preparation and capabilities in probing the information of the crystalline order, chemical composition, strain/stress, temperature and even electronic properties. With the help of the development of the microscopic instrument, the sensitivity and precision of Raman spectroscopy receive great improvement. This thesis is devoted to two aspects of the Raman spectroscopy: 1). the improvement of the Raman spectroscopy featuring researches on the advanced Raman spectroscopy/imaging techniques; 2). the application of Raman spectroscopic studies on the rapid developing carbon-based nano-materials, e.g. CNTs and graphene.

1.1 Motivation

1.1.1 Study on advanced Raman spectroscopy

As an optical method, the spatial resolution of Raman spectroscopy is greatly limited by the intrinsic property of light. This problem becomes more and more serious after the

emergence of the nano-sciences. The micro-scale spatial resolution of conventional Raman spectroscopy meets its bottleneck while studying the nano-scale materials. At the same time, the sensitivity of Raman spectroscopy also suffers from the extremely low signal throughput. In order to extend the application of Raman spectroscopy to the field of modern nano-sciences and nano-technologies, extensive efforts have been made to improve the spatial resolution as well as the sensitivity.

The localization and enhancement of the EM field induced by the noble metal nanostructures have received intensive attentions from 20th century. Such effects are due to the collective oscillations of the free electrons inside the noble metal nanostructures, known as the surface plasmon (SP). In SERS, the utilization of SP can enhance the Raman signal even in the order of twelve to sixteen, in which single molecule detection becomes possible.

Besides the enhancement of the sensitivity, localized surface plasmon (LSP) also helps for improving the spatial resolution of Raman spectroscopy. A sharp tip made of noble metal can concentrate EM field and the size of such field is in the scale of tens nanometers. In tip enhanced Raman spectroscopy (TERS, also as known as apertureless scanning near-field microscopy), the tip is scanned above the sample surface while Raman spectra are collected at each point. Spatial resolution of TERS can reach around 10 nm with single molecule sensitivity. This thesis presents studies of SERS and works on TERS based on individual silver NWs.

Recently, a new approach which employs a transparent dielectric microsphere is receiving intensive attention. Such dielectric microsphere works in near-field range as a

tiny lens to re-focus the incoming light as well as increasing the collection of the scattered Raman signal. By employing the microsphere, Raman spectroscopy with sub-diffraction-limit spatial resolution can be achieved. Our group has first timely demonstrated the less than 100 nm spatial resolution by employing an optically trapped microsphere, while this thesis dedicates another method to hold the microsphere in a more stable and controllable way by using AFM cantilever. Results and discussions about the study on the microsphere enhanced Raman spectroscopy are presented in this thesis in chapter 4.

1.1.2 Raman spectroscopy/imaging study on the carbon-based nano-materials

Carbon-based nano-materials, e.g. CNTs and graphene, have attracted great attentions due to its extraordinary physical, chemical and electronic properties. For decades, Raman spectroscopy has been playing an irreplaceable role in the study of carbon-based materials. By studying the Raman spectrum, people are able to extract information about the structure, crystal quality, electronic properties, etc. In this thesis we focus on Raman spectral study of the structural properties of such materials in the purpose of fundamental study and helping their future application in nanoelectronics.

Si-CNT structure studied by Raman spectroscopy

Because of their unique electronic properties, CNT has always been expected as the candidate of the building block of next generation electronic devices. Recently, theoretical calculation shows by forming covalent bonding to the Si atoms on the substrate, the electronic properties of CNT can be dramatically tuned. This discovery opens a new door of fabricating CNT devices by combining the mature Si based fabricating processes with the excellent properties of CNT. In order to study such special Si-CNT bonding, a characterization tool is necessary. In this thesis, we present the synthesis of such structure and Raman spectroscopy studies on the covalently bonded Si-CNT.

Determination of graphene edge chirality and crystallographic orientation by Raman spectroscopy

Graphene, a sheet of mono-layered graphite with carbon atoms arranging in a hexagonal structure, is the building block of CNTs and fullerene. Ever since its discovery, it has been receiving increasingly attentions. It is famous as a perfect two-dimensional nano-material with excellent mechanical and electronic properties. Information about the crystallographic orientation and the edge chirality (either zigzag or armchair) of graphene is very important for both fundamental study and their future applications. For example, the edge chirality strongly affects the electric properties of the performance of device fabricated by graphene nanoribbons (GNR).

In this thesis, Raman study was carried out to probe the edge chirality of the graphene sheet. Results shows that by monitoring the intensity of the defect induced Raman

feature, the edge chirality of graphene can be well assigned and the crystallographic orientation of graphene sheet can also be deduced.

1.2 Objectives and significances of the studies

1.2.1 Study on advanced Raman spectroscopy

(1). Study on the SERS of individual Ag NWs. The objectives of this part are:

- ◆ To study the SERS effect at the body and apex of individual single-crystalline Ag NWs.
- ◆ To study the polarization dependence of the enhancement on different part of the Ag NWs, e.g. body and apex.
- ◆ Use finite element method (FEM) to simulate and verify the experimental observation.

The study of Raman enhancement on the individual Ag NWs, especially on the apex of the NWs, provides a good chance to fundamentally understand of the SERS mechanism. The observation of SERS effect on the apex of the Ag NWs can also be applied to the application of high sensitivity Raman analysis.

(2). Study on the TERS of individual Ag NWs. The objectives of this part are:

- ◆ To fabricate Ag NW attached TERS tip.
- ◆ To perform TERS experiment with the fabricated Ag NW tip.

Such noble metal NW tip is expected to solve the problem of low reproducibility of

conventional TERS method, and furthermore, by combining the well developed metal NW synthesis methods, the spatial resolution and signal enhancement of TERS can be greatly improved.

(3). Study on mechanically held microsphere-enhanced Raman spectroscopy and imaging.

The objectives of this part are:

- ◆ To develop a method for mechanically holding the dielectric microsphere for Raman spectroscopy.
- ◆ Performing the Raman imaging with mechanically held microsphere.

By using the AFM cantilever to mechanically hold the microsphere, the drawback from the microsphere's Brownian motion in liquid can be avoided, thus further improves the spatial resolution of the microsphere enhanced Raman spectroscopy. Besides this, a liquid-free condition will also broaden the future application of such microsphere enhanced Raman spectroscopy.

1.2.2 Raman study on carbon-based nano-materials

1. Raman study on the Si-CNT structure

The objectives of this part are:

- ◆ To verify the Si-CNT covalent bonding, through the Raman spectroscopic study.
- ◆ Using Raman imaging technique to locate and visualize the CNT which forms

covalent bonding with the Si substrate.

- ◆ To study the structural properties of such Si-CNT bonding by polarized Raman spectroscopy.

The observations of this part show the capability of Raman imaging is a powerful tool for identifying of individual Si-CNTs bond formation. This is also crucial for the development of CNT based logic circuits with tunable electrical transport properties.

2. Determination of graphene edge chirality and crystallographic orientation by Raman spectroscopy

The objectives of this part are:

- ◆ To carry out Raman spectroscopy on the edge of graphene and study the defect induced Raman band
- ◆ To study the polarization dependence of the defect induced Raman band on the graphene edge
- ◆ To use the intensity of the defect induced Raman band determine the edge chirality of the graphene edge

The determination of the graphene edge chirality as well as the crystallographic orientation is of great significance for graphene researchers. As a non-destructive characterization tool, Raman spectroscopy also shows its great potential on studying the structural properties of carbon-based materials.

Chapter 2

Background and literature review

This chapter reviews the related literature and provides the basic background knowledge for two topics: 1) Raman spectroscopy and advanced Raman spectroscopic/imaging techniques and 2) Carbon-based nano-materials.

2.1 Raman spectroscopy and advanced Raman spectroscopy and imaging techniques

This section contains four parts. The first part introduces the basic knowledge of Raman spectroscopy in general, while other parts focus more on the advanced Raman spectroscopy techniques used in modern research. The common methodologies and experiment setup of surface-enhanced Raman spectroscopy (SERS), tip-enhanced Raman spectroscopy (TERS) and microsphere-enhanced Raman spectroscopy are described in part 2-4, respectively. The more general and comprehensive theory and experimental details can be found in the listed references.

2.1.1 Raman spectroscopy

The phenomena of inelastic scattering describe that the sample interacts with the

Chapter 2

Background and literature review

incident monochromatic light and scatters light of different wavelength. Raman scattering is one of the inelastic scattering effect, and is firstly found by C. V. Raman[1]. Usually, a monochromatic laser beam (in the range of 325 nm to 1 μm) shines on the sample. This laser light will interact with the sample, and such interaction changes the scattered light for certain energy. By detecting the scattered light, one may acquire the information of the phonon in the sample, which is closely related to the sample's intrinsic properties[2].

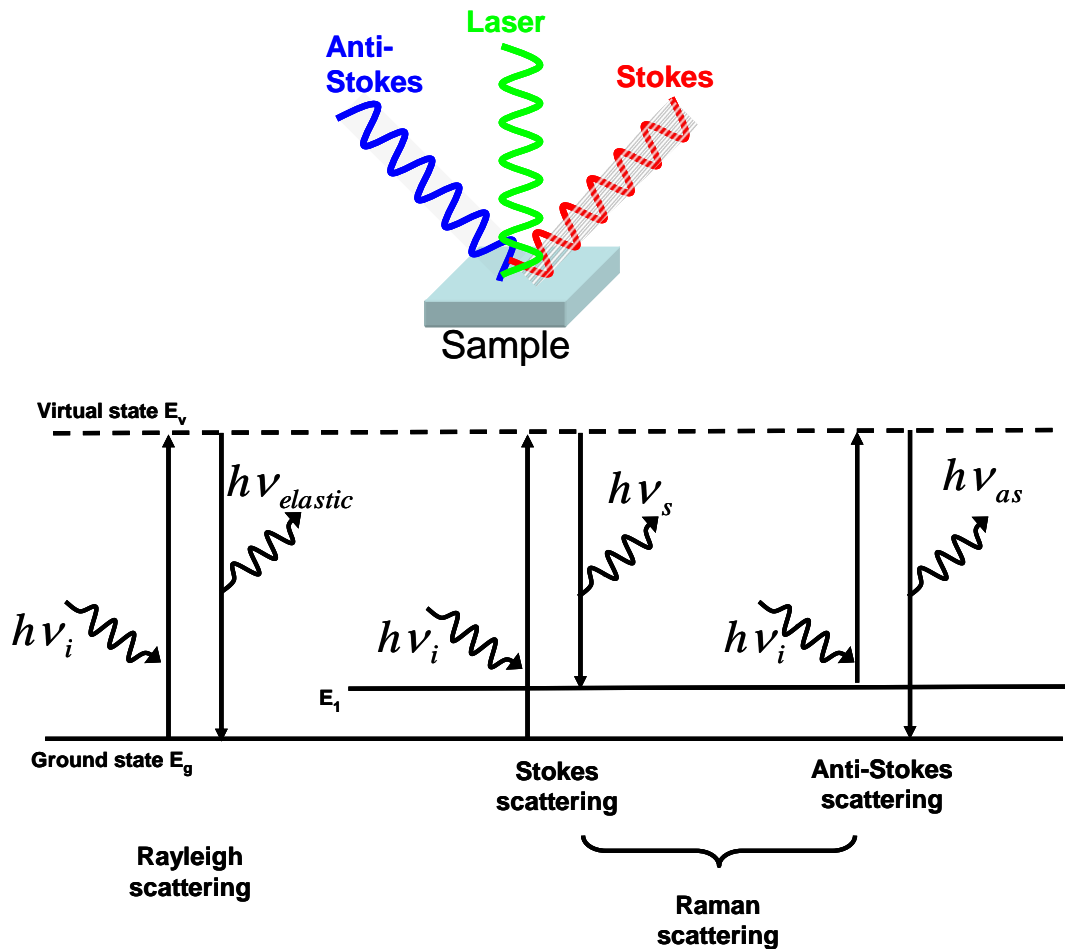


Figure 2.1 Diagram of the Raman scattering and Rayleigh scattering processes.

Chapter 2

Background and literature review

Raman effect can be understood in terms of quantum mechanics[2], as illustrated in figure 2.1. After absorbing an incident photon ($h\nu_i$), the sample is excited from electronic ground state (E_g) to an intermediate “virtual state” (E_v). In the case of elastic scattering, the sample then returns to the ground state with emitting a photon with same energy ($h\nu_{elastic} = h\nu_i$). On the other hand, in Raman scattering, after being excited to a “virtual state” the sample returns to a vibronically excited state (E_1) and emits a photon with different energy of the incident photon ($h(\nu_i - \nu_s)$), and this energy difference equals to the vibrational energy gap ($\Delta E = E_1 - E_g$). This process is also called Stokes scattering. The anti-stokes scattering can also be explained by the same process, except starting from a vibronically excited state (E_1) and finishing in the ground state (E_g) which produces a scattered photon ($h(\nu_i + \nu_s)$) with energy higher than the incident photon. The population of each energy state follows the Boltzmann distribution as indicated by the quantum mechanics, thus the ground state has a much higher population than that of the excited state in room temperature, leading to the fact that intensity of Stokes scattering signal is much stronger than that of anti-Stokes.

As a characterization tool, Raman spectroscopy probes the information of chemical composition, crystal structure and orientation, temperature, strain/stress and even electronic properties. Comparing to other surface analysis tools, like electron energy loss spectroscopy (EELS), auger electron spectroscopy (AES), X-ray photoelectron spectroscopy (XPS), secondary ion mass spectrometry (SIMS), Raman spectroscopy advantages in its non-destructivity, minimum-sample-preparation and no-requirements for vacuum. Raman spectroscopy meets the demand of material researches as a fast and

Chapter 2

Background and literature review

practical method. Besides this, because water produces extremely weak Raman signal, Raman spectroscopy serves as a very useful tool to character sample in liquid phase and is widely used in chemical and biological characterization.

Raman shift

Raman shift indicates the frequency shift of the scattered light as respected to the incident monochromatic light, and it is the most important quantity in the inelastic scattering. The unit of Raman shift is wavenumber (cm^{-1}). Raman shift reflects the intrinsic properties of the specimen but not the excitation source. As the fingerprint of materials, for different materials, or different vibration modes of same material, their Raman shifts are different.

Scattering cross section

In Raman scattering, cross section describes the probability of light-material-interaction and directly corresponds to the intensity of the Raman signal. The unit of the scattering cross section is cm^2 , which indicates the scattering coefficient of the specimen in a unit area. For comparison, the table 1 lists the scale of common scattering events[3].

Apparently, different scattering processes have different scattering cross sections. The cross section of Raman scattering is the smallest. At the same time, Mie's scattering, which describes the scattering process of particles larger than 1/10 the wavelength, covers the largest range of scattering cross section. Utilization of the large scattering

Chapter 2**Background and literature review**

cross-section of Mie's scattering will be discussed later in the SERS part.

Event	Scattering cross section (cm ²)
resonant absorption	10 ⁻¹⁶
Photoluminescence	10 ⁻¹⁶
Rayleigh scattering	10 ⁻²⁶
Raman scattering	10 ⁻²⁹
Mie's scattering	10 ⁻⁸ ~ 10 ⁻²⁶

Table 1, scattering cross section of different scattering processes.

Adapted from *Svanberg et al.*[3].

Scattering intensity

In the simple model of a molecule consists of two atoms, the molecular permanent dipole can be considered as a radiation oscillator[4]. The excitation light induces an induced dipole, which can also be considered as a radiation oscillator. The total intensity of the radiation is

$$I = \frac{16\pi^4 \cdot \nu^4}{3c^3} M_0^2 \quad (2.1)$$

In equation 2.1, ν is the oscillation frequency of the induced dipole, which is the frequency of the scattering light, and c is the speed of the light. M_0 is the magnitude of the induced dipole oscillation and the induced dipole can be described as $M = M_0 \cos(2\pi\nu t)$.

Depolarization ratio

The concept of depolarization is introduced for the reason that some fraction of the Raman scattering light has a polarization direction different from the excitation light. The value of depolarization ratio ρ is defined as

$$\rho = \frac{I_{\text{perpendicular}}}{I_{\text{parallel}}} \quad (2.2)$$

The depolarization ratio represents the anisotropy of the material, and is not only related to the average of polarizability but also depend on the anisotropy of the polarizability.

2.1.2 Surface enhanced Raman spectroscopy

The discovery of SERS

Although conventional Raman spectroscopy is an effective and practical characterization tool, there are certain drawbacks which limit its application in modern research. The biggest two bottlenecks are: 1) low sensitivity and 2) diffraction limited spatial resolution.

Nowadays, with the rapid development of the nano-sciences, people's interests move from the statistical behavior of the molecules or clusters of nanoparticles toward the properties of single molecule and individual nanoparticles. As discussed in 2.1.1, Raman scattering provides the smallest scattering cross section among all the scattering processes. Although it shows great power in the analytical study, limited by the poor throughput, conventional Raman scattering is not able to recognize neither single molecule nor individual nanoparticles.

The discovery of SERS phenomenon provided a great chance for solving the above

Chapter 2

Background and literature review

problem, thus it received intense attentions ever since its discovery. By the help of SERS effect, the scattering cross section has been improved up to 10^{14} times[5], which allows single molecular detection become possible[6-9].

SERS was firstly found by Fleischmann et al. in 1974[10]. They studied the Raman spectra of Hg_2Cl_2 adsorbed on rough Hg/Pt electrode and found a very strong Raman intensity considering the signal was collected from the surface adsorbed specimen. Then they extended their work to the pyridine adsorbed on rough silver electrode surface. In order to absorb more molecules to the electrode, the silver electrode was pre-roughened by electrochemical oxidization and reduction. By doing so, they acquired the Raman spectra of pyridine in a much better quality. In 1977, Van Duyne et al.[11] and Creighton et al.[12] repeated their experiments and found that the contribution of the molecules adsorbed on rough electrodes is 10^5 - 10^6 times stronger than that of the molecules in solution. By the help of scanning tunneling microscope (STM), it was possible for people to study the microscopic surface morphology of the rough electrodes. The STM results show that one cycle of oxidization-reduction roughening only increased 10-20% of the surface area. Even after several cycles of roughening, the increased surface area is still less than 10 times. In this sense, the increase of the amount of the molecule adsorbed on the electrode should also be less than 10 times. Thus the enhancement of the Raman signal should not be resulted from the molecule number increase. They concluded that there must be some new effects occur on the surface of the rough electrode, and named it as “surface enhanced Raman scattering” effect. It soon attracted the attention of researchers in the field of spectroscopy, electrochemistry and surface chemistry. Until

now, the study of SERS is still a very active field and receiving increasing interests.

The mechanism for SERS

After intensive experimental and theoretic study, some agreements about the mechanism of SERS effect are achieved:[13]

- (1) The SERS effect can be observed for many kinds of molecules, but only a few metal surfaces are SERS active. Nobel metals (gold, silver and copper) are most common SERS active materials, silver is the best among them due to its dielectric complex in visible light range leading to large surface plasmon absorption. Other than that, SERS effect has also been observed on lithium, sodium, potassium and some transitional metals (iron, cobalt and nickel).
- (2) In order to observe the SERS effect, the metal must have a submicroscopic surface roughness or atomic scale roughness. The submicroscopic surface roughness (10-100 nm) allows the EM enhancement of the Raman signal while the atomic scale roughness is necessary for chemical enhancement (adsorbing atoms and clusters).
- (3) SERS effect can be both long-ranged and short-ranged effect for different enhance mechanisms. For EM enhancement, even when the distance between the molecule and metal surface is in the scale of 10 nm, the Raman signal will still be enhanced. On the other hand, for chemical enhancement, the enhancement will vanish after the molecule leaves the metal surface about 0.1-0.2 nm.

Chapter 2

Background and literature review

- (4) In SERS experiment, all the Raman scattering light is depolarized, but in conventional Raman spectroscopy, the depolarization ratio is in between 0 and 0.75.
- (5) The SERS spectra are always observed as series of SERS peaks overlapped with a broad background (from $\sim 0\text{ cm}^{-1}$ to 4000 cm^{-1}). The origin of this broad background is believed to be the surface plasmon induced photoluminescence from the metal surface.
- (6) The Raman selection rule can be broken-down by SERS effect. Some IR-active modes and none Raman-active modes can be observed in the SERS spectra.
- (7) The enhancement factor varies for different molecular vibrational modes.

To study the relationship between the surface roughness and the Raman scattering factor and further understand the mechanism of SERS, many models have been raised. In principle, all the SERS models are started from the effect of rough metal surface to the local EM field and the molecular depolarization ratio. Raman scattering intensity is proportional to the square of induced molecular dipole P , in which $P = \alpha \times E$, α is the molecular polarizability tensor, and E is the incident electric field. Based on the above relationship, we can conclude that the SERS enhancement must be originated from the increase of incident electric field or the change of molecular polarizability. Thus the current SERS models can be divided into two groups, EM enhancement and chemical enhancement. Models of EM enhancement owe the SERS effect to enhancement of local EM field intensity which is induced by the localization of SP. On the other hand, chemical enhancement suggests the SERS is caused by the change of molecular

Chapter 2

Background and literature review

polarizability which is induced by the adsorption on the metal surface. Actually, the prevalent view is both two mechanisms are not independent and exclusive, but the EM mechanism is attributed as the dominant factor as well as chemical enhancement also plays an important role. Furthermore, the chemical enhancement can only occur for those molecules which fulfill the “charge transfer” process. But for EM mechanism, the enhancement factor mainly depends on the metal surface, thus it has the minimum requirement for the molecules and is closer to the universal application. In this work, we focus on studying physical mechanism of the SERS effect, so only the introduction of EM enhancement mechanism is provided here. A comprehensive introduction of the chemical enhancement can be found in the references[14-17].

Electromagnetic enhancement

EM mechanism describes enhancement brought by the collective oscillation of the free electron at the metal surface (as known as the surface plasmon) which is excited by the incident EM field[18]. For smooth metal surface, the surface plasmon (SP) is confined in the metal surface and appears as an evanescent wave, the amplitude of which decays exponentially away from the metal-surrounding interface. Under common conditions, the SP cannot be excited by light, as the wave vector of SP is larger than that of the light. But with the help of metal surface with submicroscopic roughness, the wave vector of the light is increased to match that of SP, and then the SP can be excited.

Chapter 2

Background and literature review

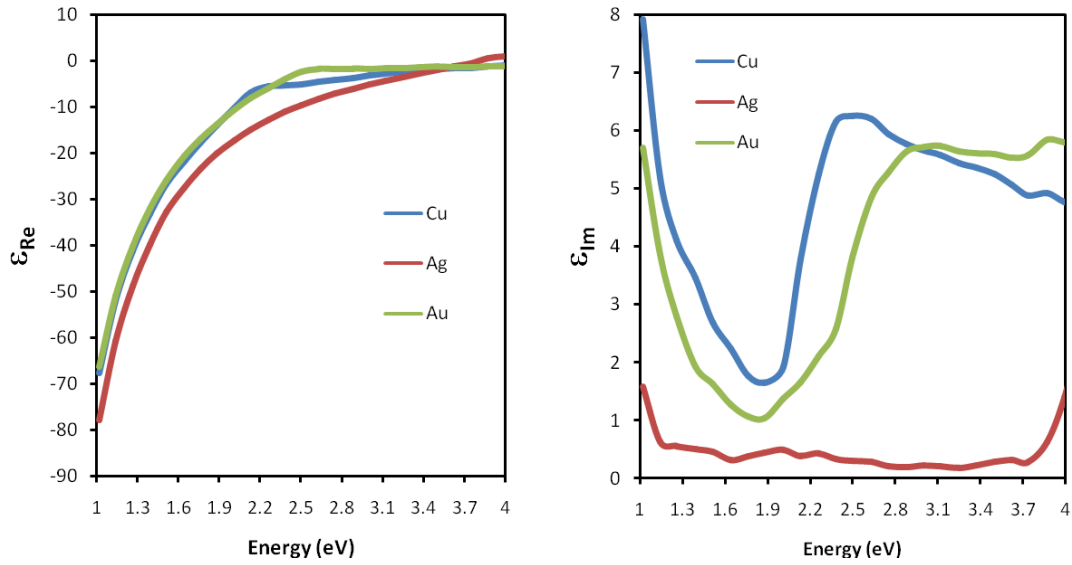


Figure 2.2 Real part (left) and imaginary part (right) of the dielectric constant of gold, silver and copper. Data adapted from Johnson, P. B. *et al.* [19]

The most basic and simplest model of EM mechanism is the SERS effect from a small metal sphere whose radius a is much smaller than the wavelength λ of incident light. As the energy of light is very high (1 eV to 4 eV), the metal is not a perfect conductor anymore. In contrast, it should be treated as dielectrics whose dielectric constant depends on the incident light wavelength, as $\epsilon_1 = \epsilon_1(\omega)$. The wavelength dependence of complex constant dielectric of gold, silver and copper is shown in figure 2.2. Considering such a metal sphere in the medium with a dielectric constant of ϵ_0 , and a spatially uniformly applied EM field E_0 which depends only on time,[20] from the classic electromagnetic theory, the electric field at the metal sphere/medium interface can be derived as[21]:

Chapter 2

Background and literature review

$$E_e = \frac{3\varepsilon_1}{\varepsilon_1 + 2\varepsilon_0} E_0 \quad (2.3)$$

And the enhancement factor $G = \left| \frac{E_e}{E_0} \right|^2$ can also be written as:

$$G = \left| \frac{3\varepsilon_1}{\varepsilon_1 + 2\varepsilon_0} \right|^2 = \frac{9(\text{Re } \varepsilon_1^2 + \text{Im } \varepsilon_1^2)}{(\text{Re } \varepsilon_1 + 2\varepsilon_0)^2 + \text{Im } \varepsilon_1^2} \quad (2.4)$$

Substituting the complex constant dielectric shown in figure 2.2 into equation 2.4, one can calculate the enhancement factor of the enhancement factors of these metal nanoparticles (radius around 50~100 nm) verses the incident light wavelength, while the surrounding by air or vacuum ($\varepsilon_0=1$), as shown in figure 2.3. For nanoparticles with bigger size, multipole responses of the nanoparticles appear which leads to a broadening of the enhancement profile.

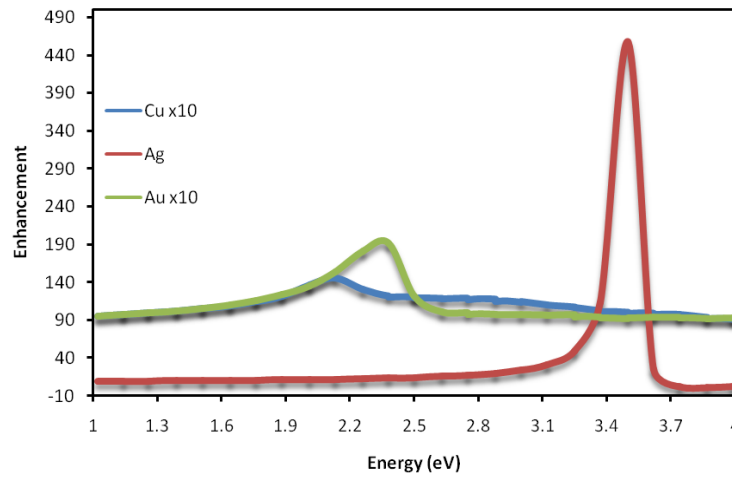


Figure 2.3 Calculated Raman enhancement of single metal nanoparticles in the function of excitation wavelength (energy).

The calculation results of the individual nanoparticles reveal some important properties, but this model is still a distance away from the real application of rough

Chapter 2

Background and literature review

metallic surfaces. As AFM results show that on the electrochemical roughed metallic surface, particles are not isolated, thus the inter-particle interaction is not negligible. By considering the EM coupling between the adjacent nanoparticles, the closely packed particles (inter-particle distance smaller than 10 nm), the SP is more confined and localized, inducing an enhancement factor as high as 10^{12} which is enough to detect a single molecule. In this manner, studies of SERS on single molecules have been carried out [6-9]. Series of works have been done to study the SERS dependence of physical environment, size, shape, materials and the inter-particle distance. In this period of time, SERS is on its way to become a practical characterization tool.

2.1.3 Tip-enhanced Raman spectroscopy

Background of TERS

Being an optical technique, the spatial resolution of conventional Raman microscopy is limited by the diffraction of light, as known as Rayleigh criterion $d = \frac{0.61\lambda}{NA}$, where d is the minimum distance between two points that an optical system can resolve, λ is the light wavelength, and NA (numerical aperture) is a parameter of the objective lens. For conventional Raman microscopy, which is utilizing light in the range of ~300 to 1000 nm, has the best resolution in hundreds of nanometer scale. Such spatial resolution is far away from the urgent demand of a nondestructive analysis method to resolve sub-10 nm features in the study of nanosciences, biological applications and semiconducting industry. Although using shorter wavelength light (e.g. deep ultraviolet light) can improve the spatial resolution to certain extent, the lack of

Chapter 2

Background and literature review

suitable light source and difficulty in lens fabrication make such approach an extreme difficult task.

Actually, the Rayleigh criterion arises from a far-field theory, in which the detection and illumination distances are much larger than the wavelength of light. Thus it is possible to bypass this criterion by applying a near-field setup, in which either detection or illumination happens in distance much smaller than incident wavelength, for example, less than several tens of nanometers.

One of the near-field approaches is aperture-scanning near-field optical microscope (aSNOM). In aSNOM, a tapered optical fiber with a small aperture (50–100 nm) is used to deliver the laser light and the fiber is kept at a close distance (~tens of nanometer) above the sample surface. In this manner, the small aperture acts as a near-field illumination source, and the spatial resolving capability of the aSNOM system is in the same scale of the aperture. However, this technique has been plagued for Raman study because of the very low throughput of the laser through metal-coated optical fibers (typically 100 nW) and the intrinsic weakness of the Raman scattering. A Raman imaging of decent signal/noise (S/N) ratio may cost more than 10 hours. Due to the above reasons, this technique is not widely used for Raman imaging now[22].

An alternative approach is to use apertureless technique, also called tip-enhanced Raman spectroscopy (TERS). In TERS, a sharp metal tip (radius of curvature <100 nm) is introduced instead of the “aperture”. By shining the laser on the apex of the tip, due to the shape of the tip, the LSP can be excited at the vicinity between the tip and sample and yield a much stronger Raman signal from that tiny probing volume, due to the

Chapter 2

Background and literature review

electrostatic lightning rod effect[23-25], surface plasmon resonance (SPR)[26-28] and even the gap-mode effect (while the presence of metallic substrate)[29-32]. Such highly confined EM field can yield a much stronger Raman signal (near-field signal) from the portion of the sample which is inside that tiny probing volume (10~100 nm). In this approach, the intensive enhancement of the EM field on the tip apex surpasses the disadvantage of the aSNOM, and makes the duration of a high spatial resolution Raman imaging within an acceptable time.

Instrumental details

In order to keep a constant tip-sample distance, TERS is normally modified from AFM or STM with an integrated optical microscope system and spectrometer.

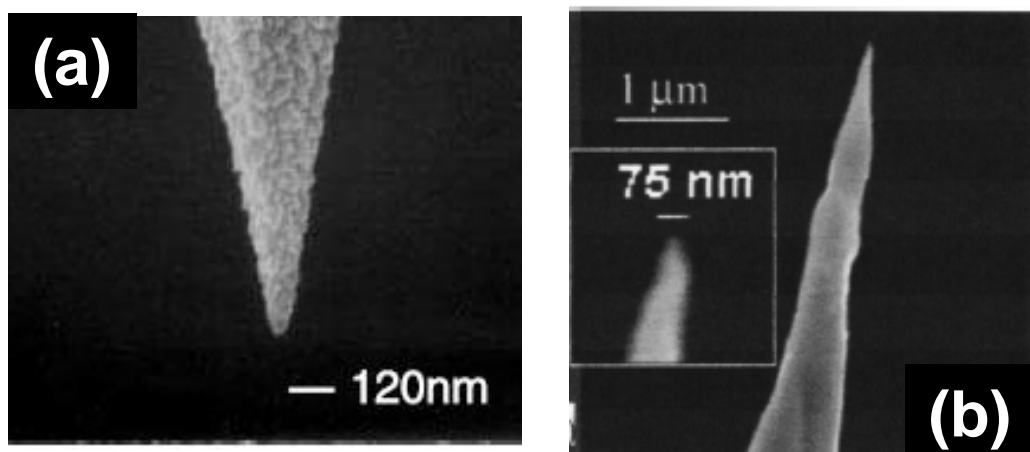


Figure 2.4 (a) Silver coated AFM tip. Adapted from Hayazawa *et al.*[33] (b) Silver tip prepared by electrochemical etching. Adapted from Ren *et al.*[34]

Many methods have been applied to fabricate a “hot” TERS tip. One method is

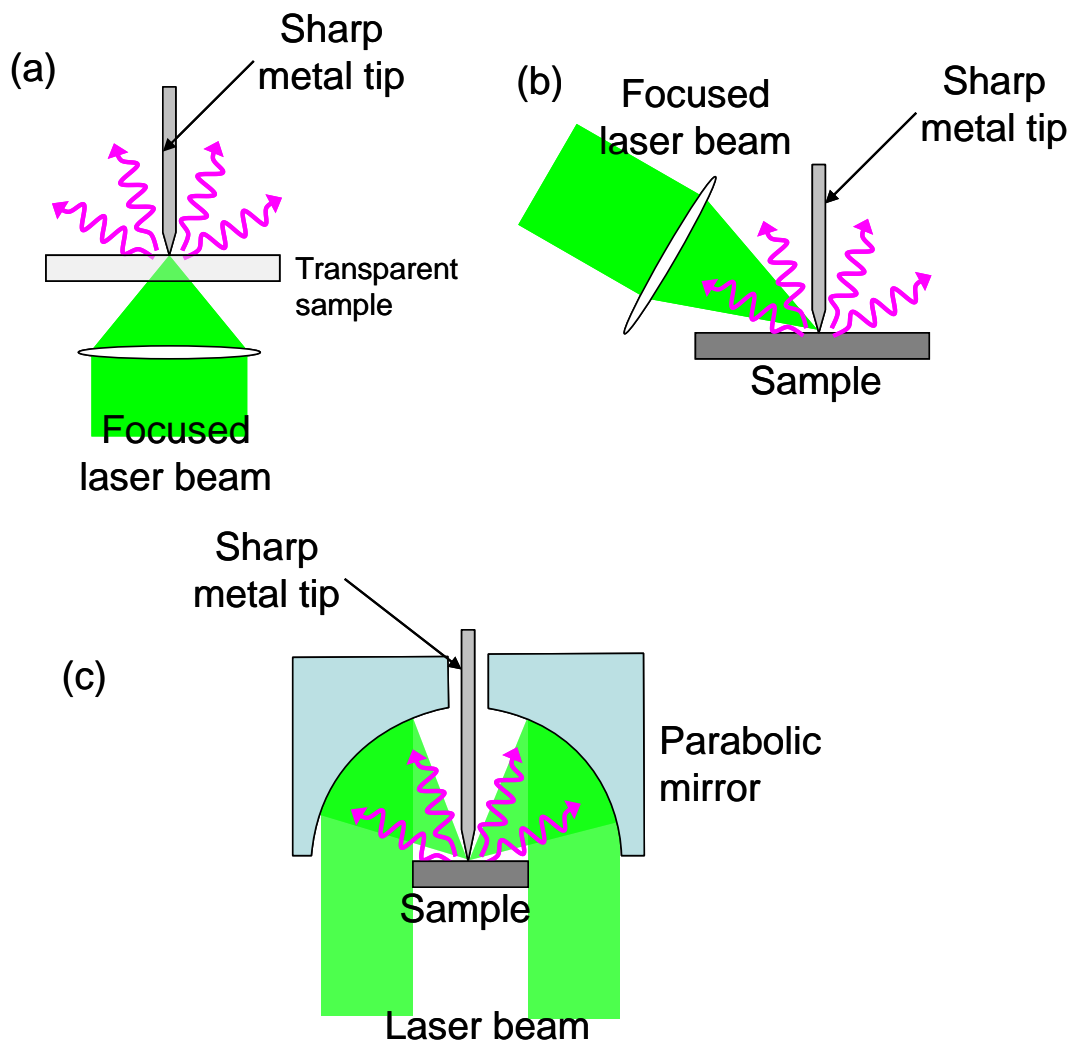


Figure 2.5 Experiment setup of TERS. (a) Back-reflection setup: the focused laser shines on the tip through a transparent substrate and excites the LSP. (b) Reflection mode: the incident laser illuminates the tip from side. (c) Top illumination setup: the incident laser is reflected by a parabolic mirror and shine on the tip.

coating a fine metal (e.g., silver or gold) film on an AFM tip, and the other method is directly fabricating the tip through an electrochemical etching process (figure 2.4). For metal coated tips, the smoothness is the main requirement and the size of the tip is

Chapter 2

Background and literature review

greatly limited by the thickness of coated film. But coating the tip with an ultra-thin (thickness < 5 nm) film with roughness less than 5 nm is quite challenging. Besides this, such a thin film is very easy to be worn off or oxidized after several scans. Although etched tips do not have such “worn off” problems, producing sharp tips with a smooth surface is always complicated and the etching process may involve toxic chemicals.

The TERS works in several different setups as shown in figure 2.5[35]. The back-reflection setup [figure 2.5(a)] is one of most commonly used setup, in which the focused laser shines on the tip through a transparent substrate and excites the LSP. In order to create an electric field parallel to the axis of the tip, a high NA objective lens must be employed to realize the longitudinal mode of the focused linearly polarized laser beam[36]. To further increase the field intensity of the longitudinal electric field, the radial polarized laser beam[37] can be used. Other than the back reflection mode, the other commonly used setup is reflection mode, as shown in figure 2.5(b). In this mode, the incident laser illuminates the tip from the side. It is much easier to create an electric field polarized along the tip axis, and by applying a polarizer, the signal to noise ratio will be greatly improved. Another alternative method, which combines the above two setups is shown in figure 2.5(c), is the top illumination setup, in which the incident laser is reflected by a parabolic mirror and shine on the tip. By using this setup, people can use opaque substrate with all the benefits from the reflection setup (e.g., high S/N ratio).

Recent development of TERS

Direct imaging of single molecule absorbed on gold surface

Chapter 2

Background and literature review

The prevalent statement is that in order to detect a single molecule, the enhancement factor should be in the order of 10^{14} , but with employing the metal tip only, the maximum enhancement factor of 10^6 . Thus a noble metal substrate is necessary to achieve a setup of “gap mode”, which dramatically boosts the enhancement factor. By the help of the “gap mode”, many people achieved the semi-single-molecule detection by observing the Raman peaks position/intensity fluctuation which is believed to be the characteristics of single molecule detection [38-42]. Recently, Pettinger et al. [43] demonstrated direct observation of a single molecule. As their TERS is modified from a STM, they can verify the number of the molecule detected by TERS using STM. STM imaging was employed firstly to locate the single BCB molecules absorbed on gold substrate, and then TERS spectrum of the single BCB molecule and TERS image of the same molecule are collected. Besides the 15 nm spatial resolution, characteristic Raman band of BCB is clearly observed in the spectrum with the integration time only 1 s. Although the resonant of the BCB molecule helps the enhancement factor, this observation surely shows the great potential of the TERS as a future surface analysis tool.

Bio-Materials

One of the hottest bio-materials nowadays is DNA. Using Raman spectroscopy to detect DNA bases and direct imaging on DNA have been studied since long time ago. People believe that one day, optically sequencing DNA is possible. But it is nearly impossible for conventional Raman spectroscopy to extract information from single DNA, as their Raman signal is too weak. By the help of the single-molecule-sensitivity

Chapter 2

Background and literature review

and nanometer-scale spatial resolution, the utilization of TERS brings us closer to our aim. Recent development of TERS study on DNA samples[44] and other biological samples as ommatidial surfaces[45], adenine molecule[46] and bacteria[47] shows the great potential of TERS in the biology study.

Strain/Stress measurement on semiconducting samples

After the introducing of the strained silicon, local strain/stress of the Si devices has been receiving more and more attention. By engineering local strain/stress, the electron/hole mobility and the device performance can be dramatically tuned, which is one of the solutions to follow the famous Moore's Law without shrinking the size of the individual transistor.

As the channel size has reached 46 nm, conventional Raman spectroscopy is no longer suitable to probe the local strain/stress, and this is the place where TERS comes into play. Saito et al. have demonstrated several TERS study on strained Si samples to probe the local strain distribution[48, 49]. All these efforts were dedicated TERS towards a routinely characterizing tool in modern semiconducting industry.

Limitation of TERS

Although TERS reveals promising application potential, it is currently still a technique which can only perform in a few specialized laboratories. The complicated SPM setup and poorly repeatable tip preparation process are the biggest issues to limit its future applications[50]. Thus our work dedicates to develop a rather simple and practical

method to reproducibly fabricate TERS tip, and further utilizing TERS for the daily characterization works.

2.1.4 Dielectric microsphere enhanced Raman spectroscopy/imaging

Dielectric microspheres, such as polystyrene (PS), silica (SiO_2) and titanium oxide (TiO_2) have been widely used in research areas of physics, chemistry, biology, material science, etc. Metal nanoparticles array with the size of each particle ranging from 10 nm to 100 nm can be fabricated by nanosphere lithography using self-assembly dielectric spheres[51]. The dielectric sphere is a basic component to perform optical tweezers. Such technique has been widely applied in manipulating micro/nano-scale objects, molecules and cells[52]. The optical whispering gallery mode in dielectric sphere has also attracted intensive attentions in these years[53-55].

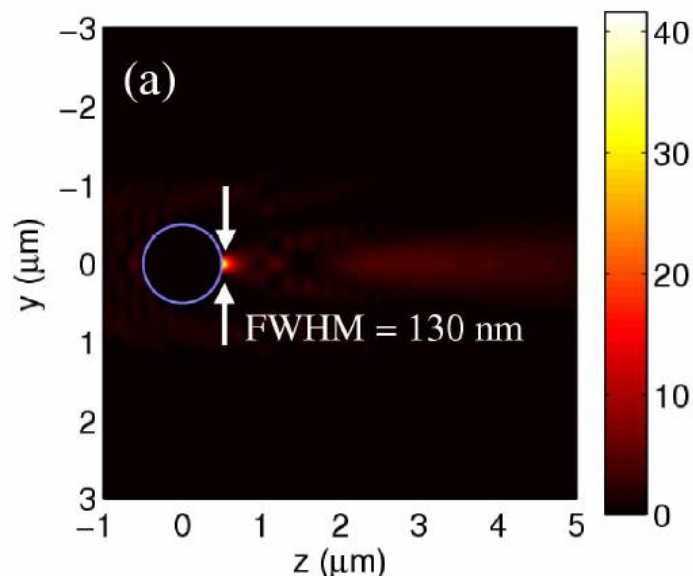


Figure 2.6 The near-field intensity distributions Photonic nanojets generated by illuminating a dielectric spheres with diameter of 1 μm .

Adapted from Li et al.[56].

Chapter 2

Background and literature review

Besides these, in 1997, Minoru et al. found, that under microscope, optically trapped dielectric microsphere can behave like micro-objective-lens[57]. With the help of the micro-objective-lens, they can observe features which conventional microscope cannot well observed. Inspired by that progress, many works have been carried out to study the optical properties of the microsphere in terms of light focusing capability. Theoretical simulation shows that the dielectric microsphere can focus light into a sub-diffraction-limited size, named photonic nanojets [56], as shown in figure 2.6. Such small beam size and highly intensive field strength will improve the spatial resolution to ~ 100 nm with visible light illuminating. Along with the spot size, three-dimensional properties of the photonic nanojets have also been studied both theoretically[58] and experimentally[59].

At the same time, applications inspired by the photonic nanojets, have been demonstrated, including backscattering enhancement[60], data storage[61], high resolution lithography[62], etc.

Motivated by these achievements, we developed the microsphere-enhanced Raman spectroscopy. The spatial resolution and signal of Raman spectroscopy can be dramatically improved by placing a dielectric microsphere between the objective lens and the sample. In our approach, the dielectric microsphere is held by either focused laser beam (optically) or cantilevers (mechanically). This approach advantages in highly repeatability, no far-field signal, minimum sample preparation and simplicity. In chapter 4, we will discuss the detailed experimental process and preliminary results.

2.2 Carbon-based nano-materials

The discovery and development of carbon-based nano-materials (e.g. C₆₀, CNTs, graphene, etc) are among the hottest topics in the material research field, and have attracted intensive attentions in 21st century. Because of their extraordinary physical, chemical and even mechanical properties, carbon-based nano-materials are believed to be the main building block for next generation electronics devices replacing the conventional silicon-based devices. Their nanoscale dimensions, simple structures and nearly perfect crystallinity also provide great models for researchers to exploit the size effects in a nanometer scale.

As our research focus on CNT and graphene, this chapter is divided into two parts, respectively. Background knowledge of the CNT and graphene will be provided and more details are referred to the cited journal articles and book chapters for a deep and comprehensive understanding of carbon-based nano-materials.

2.2.1 Carbon Nanotubes

Discovery of Carbon Nanotubes

CNT was first discovered by S. Iijima in 1991, in the carbon soot of an arc discharge experiment[63]. He observed some hollow coaxial multi-shelled tube-like structures with hexagonal arranged carbon atoms. It was then confirmed that they were multi-wall CNT (MCNT). Two years later, both S. Iijima[64] and D. Bethune[65]

Chapter 2

Background and literature review

successfully fabricated the SWCNT.

The discovery of CNT shows great significance in modern material research. Besides its fascinating properties, it also shows exciting application potential in clean energy, semiconducting, medicine, etc. The study of CNT is not limited in physics, chemistry and material sciences, but also attracted great interests from life sciences, electronic engineering, etc.

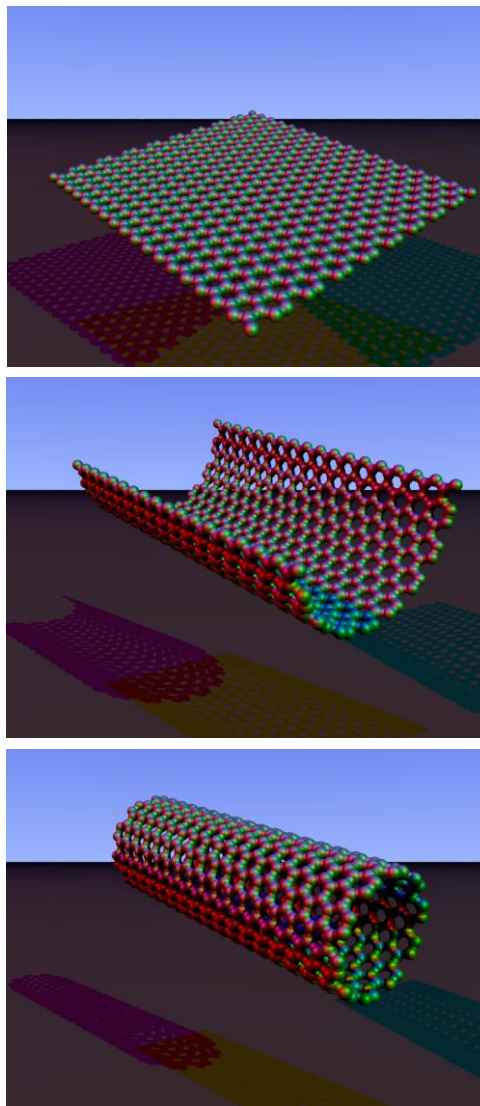


Figure 2.7 Diagram of CNTs rolling up by a piece of graphene sheet.

Adapted from internet website: <http://en.wikipedia.org>

Structures of carbon nanotubes

Most SWCNT have the diameter around 1 nm, and the length can be as long as several centimeters[66]. It can be considered as a product of seamless rolling up by a piece of single-layered graphite (also known as graphene), as shown in figure 2.7. Due to its extreme high aspect ratio, CNT is a perfect example of one-dimensional nanostructure with center axial-symmetry. It is easy to understand that for wrapping a piece of graphene along different direction, the final CNT will have certain spiral configuration, which is called chirality[67].

◆ Chirality vector \vec{C}_k and chirality angle θ

To define the chirality of CNT, here we introduce the chirality vector \vec{C}_k . An unrolled graphene sheet is shown in figure 2.8, vector \vec{OB} indicates the long axis of the CNT, and vector \vec{OA} is the rolling direction or the circumference of the tube. To form a CNT, imaging the graphene is rolled up along \vec{OA} seamlessly, so that point O and A coincide with each other and also point B and B'. \vec{OA} and \vec{OB} are defined as the chirality vector \vec{C}_k and the translational vector \vec{T} , respectively.

In the hexagonal lattice of graphene, lattice constant $a = |\vec{a}_1| = |\vec{a}_2| = 0.246\text{nm}$, where $\vec{a}_1 = (0.213, 0.123)\text{ nm}$, $\vec{a}_2 = (0.213, -0.123)\text{ nm}$. \vec{C}_k can be expressed as

$$\vec{C}_k = n \cdot \vec{a}_1 + m \cdot \vec{a}_2, \quad (2.5)$$

where m and n are integers, and $0 \leq |m| \leq n$. This expression can normally be simplified as $\vec{C}_k = (n, m)$. Once \vec{C}_k is established, the diameter D of a CNT can also be calculated by

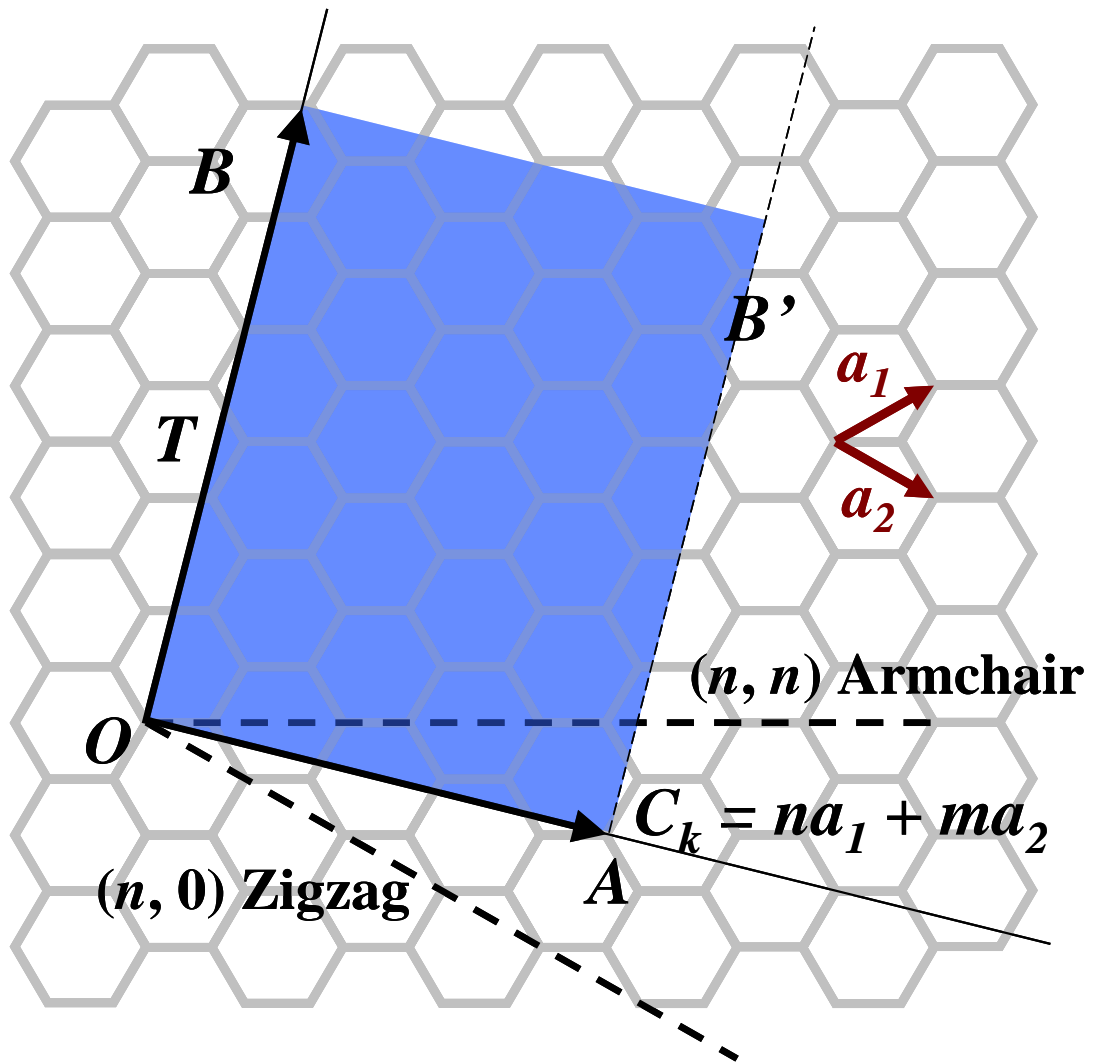


Figure 2.8 A graphene lattice which forms a CNT by connecting point O and A , B and B' .

Chapter 2

Background and literature review

$$D = \frac{L}{\pi} = \frac{|\vec{C}_k|}{\pi} = \frac{a}{\pi} \sqrt{m^2 + n^2 + mn} \quad (2.6)$$

The chirality angle θ is defined as the angle between the chirality vector \vec{C}_k and vector \vec{a}_1 (or \vec{a}_2), and $0^\circ \leq \theta \leq 30^\circ$, due to the six-fold degenerated symmetry of the honeycomb lattice structure. The chirality angle can also be expressed in term of n and m :

$$\theta = \tan^{-1} \left(\frac{\sqrt{3}m}{2n+m} \right) \quad (2.7)$$

In the case of $m = n$, the chirality angle $\theta = 30^\circ$, it is called armchair CNT. In the case of $m = 0$, $\theta = 0^\circ$ and a zigzag CNT is formed. CNT with all other (n, m) ($0^\circ < \theta < 30^\circ$) is called chiral CNT.

◆ Translational vector \vec{T}

The unit vector of a one-dimensional CNT is defined as the translational vector \vec{T} , which is parallel to the long axis of the CNT and perpendicular to the chirality vector \vec{C}_k , as shown in figure 2.8. \vec{T} can be expressed as:

$$\vec{T} = t_1 \vec{a}_1 + t_2 \vec{a}_2 \equiv (t_1, t_2), \quad t_1 \text{ and } t_2 \text{ are integers} \quad (2.8)$$

and again, t_1 and t_2 can be expressed in term of m and n :

$$t_1 = \frac{2m+n}{d_R}, \quad t_2 = -\frac{2n+m}{d_R}, \quad (2.9)$$

where $d_R = 3q$ if $n - m$ is multiple of $3q$, (q is the greatest common divisor of (n, m)), otherwise $d_R = q$. The magnitude of \vec{T} can then be expressed as:

$$|\vec{T}| = \frac{\sqrt{3}L}{d_R}, \quad (2.10)$$

where L is the magnitude of the chirality vector \vec{C}_k .

Synthesis of carbon nanotubes

The aims of the CNT fabrication are high purity and high throughput. As the synthesis is not the key point of this thesis, only some general information of the synthesis methods will be provided here. More details can refer to the listed references

Conventional methods to fabricate CNT are: 1) arc discharge[63-65], 2) laser ablation[68] and 3) chemical vapor deposition (CVD)[69]. To synthesize SWCNT, metallic catalyst as cobalt, nickel, iron, palladium, yttrium, etc. are always necessary. The size of the metal catalyst is also important as it affects the CNT's size and purity. For synthesizing MWCNT, such catalyst is not necessary.

In arc discharge methods, two graphite electrodes were placed in the center of the reaction chamber. Normally there is a groove on the cathode containing the metal catalyst. In the experiment, 200 A direct current of 20 V is applied between the electrodes to form arc discharge. Then the CNT will form on the surface of the cathode.

The laser ablation method uses focused pulsed laser to fabricate the CNT. In this method, a graphite target mixed with catalyst is placed in a quartz tube. When target is heated up for 1200 °C, with the help of the laser, carbon vapor mixed with catalyst are generated and flow to the low temperature zone, where CNTs are growing. By using this method, highly purified and graphitized SWCNT can be produced, but, restricted by the low throughput and high cost this method may not be commercialized.

CVD has become the most attractive synthesis method these years. In this method,

Chapter 2

Background and literature review

the hydrocarbon compound vapor decomposes and forms CNT with the presence of the catalyst. Comparing to arc discharge method, product of CVD is purer and the efficiency is higher. CVD also advantages in its lower growth temperature, simpler equipment and highly controllable process by comparing to laser ablation. Thus, CVD is attracting more and more attention and is believed to be the solution toward CNT mass production.

Properties and applications of carbon nanotubes

Due to the extreme aspect ratio for its one-dimensional structure, nano-scale dimension and unique bonding structures, CNTs own many extraordinary properties in five aspects: mechanical properties[70, 71], electronic properties[72-82], field emission properties[83-92], hydrogen storage properties[93-97] and electrochemical properties[98-104].

2.2.2 Graphene

Discovery of graphene

Graphene, known as the thinnest material which consists of one single layer of graphite, has become the focus point of the materials researchers ever since its appearing. Actually, people started to show interests on it long before its “existence”, and lots of calculation works had been done to study its fascinating electronic properties[105-109].

It was once believed that the free state planar graphene does not exist[110], as comparing to the curved form of carbon like fullerenes and CNT, the structure of

Chapter 2

Background and literature review

graphene is not stable. In addition, once graphene immobilized on substrate, such ultra-thin layer will be invisible. The visibility issue was settled in 2007, A. Geim et al. found that with the help of a 200 nm SiO_2/Si substrate, single layered graphene is observable under microscope [111-113]. People use sticky tape to “peel off” graphene from bulk graphite and transfer them to the SiO_2/Si substrate. The micromechanical cleavage graphene (MCG) is randomly distributed with varieties of layer number. By the help of the SiO_2/Si substrate, graphene with different numbers of layer can be easily found under microscope [114].

Although this method is not highly productive, it provides a comparably simple and effective way to produce pristine “free state” graphene. Furthermore, SiO_2/Si substrate is very friendly to the following device fabrication processes, and the SiO_2 layer can also serve as gate oxide for the graphene field effect transistor (FET). This method is widely adopted for graphene study in the research level.

Even the biggest MCG can be as big as 1 mm^2 , it is still not a mature method for future commercial application. Thus, finding a method which has a much higher yielding and more controllability is a job to be accomplished before the real application of graphene.

One alternative method is epitaxially growing graphene on SiC crystals and metallic substrate [115-119]. For example, by annealing the SiC substrate in high vacuum to evaporate the surface Si atom, graphene will form. The number of layer can be controlled by varying different annealing temperature and duration. This method appears to be very productive that even wafer-sized graphene is possible, but there are still some drawbacks.

Chapter 2

Background and literature review

To relax the strain and as the initial stage of the graphitization, a buffer layer which behaves like graphene but covalently bonded to the below SiC atoms, forms in the beginning of the growth. Such layer is difficult to remove and affects the performance of the graphene devices. Besides this, the high cost to fabricate the single crystalline SiC substrate is also a big problem.

On the other hand, synthesis graphene by chemical method[120] and CVD method[121-133] are the trend of the current research, because of their high productivity and controllability. Although their purity of product is still annoyingly low, these two methods are still believed to be the industrial practical approach in the future.

Properties and future applications of graphene

Graphene is called the “most extraordinary” material after the discovery of CNTs, as it reveals many fascinating properties.

It shows a very high spring constant ranging from 1-5 N/m and a Young's modulus in the TPa-scale. These mechanical properties make graphene an ultra strong and rigid material, which is ready for future nano-electromechanical application [134-136].

The extreme aspect ratio of graphene makes its highly sensitive to the surrounding environment. Gas sensing device made of graphene can even detect single molecule adsorbed on it[137].

Furthermore, at the two K points (K and K') in graphene's Brillouin zone, the conduction band touches the valence band, so, in the vicinity of these point, the electron behaves masslessly due to the linear relationship of the electron energy E and wavevector

k ($E = \hbar k V_t$) [105-108, 138]. Such linear relationship also leads to some fascinating phenomena like anomalous quantum Hall effect[112, 113], Klein tunneling,[139-141] valley polarization[142, 143], etc. Besides this, graphene displays the highest mobility ($\sim 120\,000\text{ cm}^2/\text{V}\cdot\text{s}$) in room temperature among all known semiconductor [144-147]. All these have made graphene a great candidate for the next generation semiconducting material and replace the current silicon devices. Detailed information could be found about the physics and structural/electronic properties of graphene from the review articles[138, 144, 148].

2.2.3 Raman spectrum of graphene and carbon nanotubes

Raman spectroscopy has been extensively used to probe structural and electronic characteristics of carbon materials, especially that of CNTs and graphene-related materials. In general, Raman spectroscopy is a characterization tool that provides information on the vibrational states of a bulk sample and it is normally neither sensitive to the surface nor to the electronic energy levels. However, in the study of graphene and carbon nanotubes, due to the strong resonance behavior for a large range of laser excitation wavelengths, Raman becomes a useful tool to study the electronic structure as well. The resonance effect also makes the Raman signal extremely strong, which making study of SWNT and single-layer graphene possible.

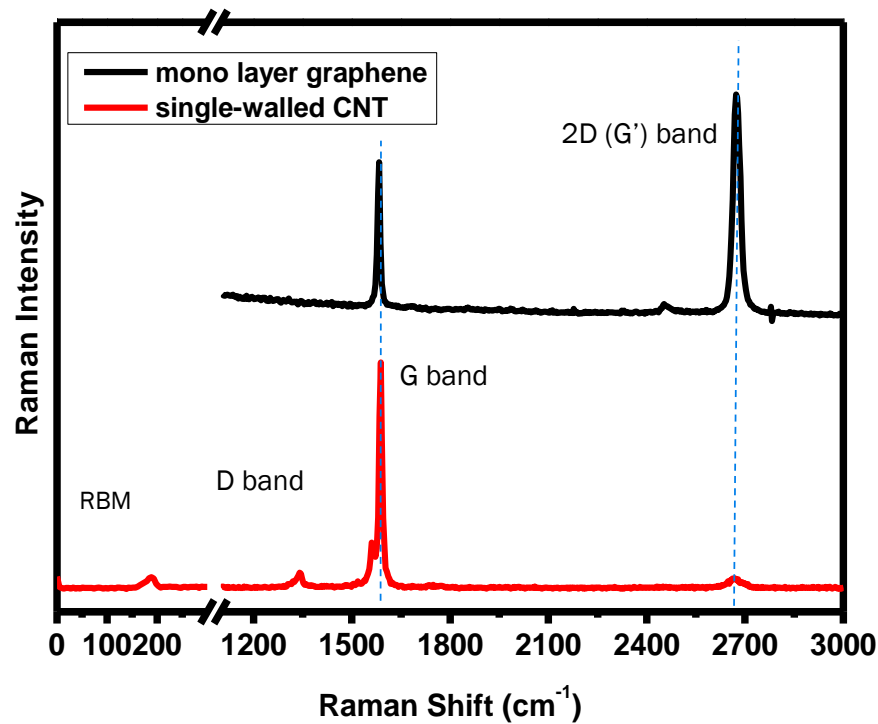


Figure 2.9 A comparison of typical Raman spectra collected on graphene and CNT.

In figure 2.9, typical spectra from graphene and CNT are compared. Due to their similar atomic structure, both graphene and CNT have three major Raman features of graphene and CNT: G band ($\sim 1580 \text{ cm}^{-1}$) which rises from the in-plane vibration of the sp^2 carbon atoms,[149] and the 2D band around 2700 cm^{-1} which is second-order process induced Raman feature.[150-152] In the case of presence of disordered carbon atoms or the edge of graphene, another band located around 1300 cm^{-1} can be observed, which is called the defect-induced band or D band. The appearance of the D band and 2D band is related to the double resonance Raman scattering process, which consists of several steps. For the D band, an electron-hole pair is excited. Then the electron (or hole) is inelastically scattered by a phonon, following the elastic scattering of the electron (or hole) by a defect. Finally, the excited electron and phonon recombine.[153] For the 2D band, elastic scattering of the electron (or hole) in the above process is replaced by the second phonon. By studying the Raman spectrum,

Chapter 2

Background and literature review

one can obtain a lot of useful information. Interested readers can refer to two comprehensive reviews on Raman study of graphene and CNT. [152, 154]

Chapter 3 *Surface enhanced Raman scattering and tip-enhanced Raman scattering study utilizing individual single crystalline silver nanowires*

Chapter 3

SERS and TERS study of individual single crystalline silver nanowires

3.1 SERS study of individual single crystalline silver nanowires

3.1.1 Introduction

SERS was discovered around 30 years ago and remains as one of the most important techniques for improving conventional Raman spectroscopy in surface analyses[10-12]. In the last decade, the research has moved toward the single molecules detection by the giant enhancement in SERS[6-9]. Although the observations are only supported by indirect proofs, it is commonly accepted that single molecules SERS are promising. Single molecules detections are mostly demonstrated using nanoparticles aggregates or roughened metal as a substrate. It is widely believed that the EM enhancement induced by the effect of LSP contributes the most for the enhancement in SERS. The LSP is in form of the highly confined EM field that interacts with the analyte molecules and by the help of the LSP, both incident and scattering field will be enhanced. The locations of the confinement are termed as “hot spots”.

In spite of the strong Raman signal, SERS by nano aggregates/roughened substrates suffer from several drawbacks such as random formation of hot spots (not every single particles or spacing between particles can have strong enhancement) and lack of control over the enhancement factor[155]. To further understand the EM enhancement in SERS, study on isolated hot spots is of importance. Several groups have reported SERS

Chapter 3 *Surface enhanced Raman scattering and tip-enhanced Raman scattering study utilizing individual single crystalline silver nanowires*

observed on single nanoparticles or nanoparticle-pairs[156-159]. In this work, we presented polarized SERS study at the apex and body of individual single-crystalline Ag NWs. The strong enhancement at the apex is induced by incident laser polarized along the Ag NWs' long axis, and the observation resembles the "lightning rod effect" of the NWs. The enhancement factor of the tip is significantly higher than body of the NWs. This result is highly repeatable, as almost all the wires prepared are able to give the strong enhancement. This also demonstrates an effective way to isolate single hot spots for SERS study, as the Ag NWs can be easily located by optical microscope and the hot spots are always located at the tip.

Another advantage of Ag NWs is the shapes and sizes of the wires are adjustable. Through the development of NWs fabrication technologies, the diameters and lengths of Ag NWs are well controllable. By this motivation, we simulate different diameters of the NWs under the same experimental condition and found that enormous enhancement can be achieved by using smaller dimension of Ag NWs. Our results show that the noble metal NWs is a great candidate for enhancement in SERS and such NW also provide a good model to study the physics behind the SERS effect.

3.1.2 Experimental

As the first step, we fabricate uniform single-crystalline Ag NWs in solution by using hydrothermal method[160]. Firstly, 5 mL 0.02 M silver nitrate is added to 30 mL deionized water (18.2 M Ω). Then the solution was vigorously stirred for 10 min, during the stirring process, 5mL 0.02 M sodium chloride, followed by 0.04 g glucose was gently

Chapter 3 *Surface enhanced Raman scattering and tip-enhanced Raman scattering study utilizing individual single crystalline silver nanowires*

dropped in. Finally, the solution was transferred into a stainless steel autoclave with a Teflon liner of 80 mL capacity, and heated in oven at 180 °C for 18h. After that, the as-prepared NWs are purified by centrifuge in deionized water and absolute ethanol for five times, and then stored in ethanol solution.

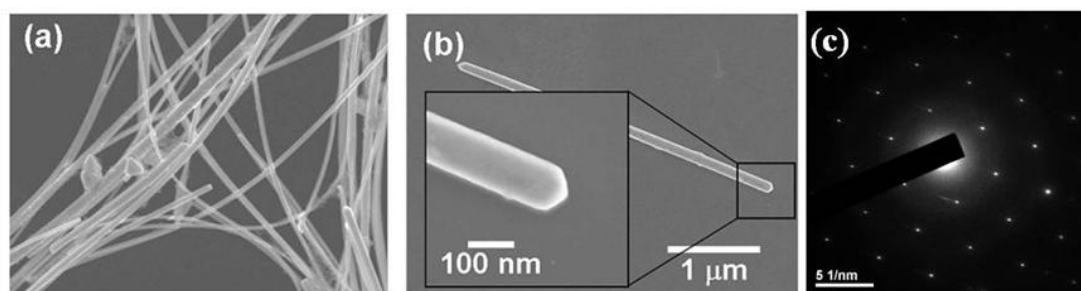


Figure 3.1 (a) SEM image of as-prepared Ag NWs. (b) SEM image of an single crystalline Ag NW. The inset shows the zoom-in view of the apex of the wire. (c) TEM SAED pattern of individual Ag NW.

The NW solution was dropped and dried on Si substrates for the next step SERS study. We then added in the etching process by immersion in concentrated chloride acid (HCl 35M) to remove the oxide layer of the Ag NWs and alter the tip morphology. Scanning electron microscope (SEM) image of the typical NWs obtained is shown in figure 3.1(a). The diameters of the Ag NWs obtained are approximately 150 nm and the length around 15 μm . The NWs have very sharp apex, as shown in the inset of figure 3.1(b). A TEM selected area electron diffraction (SAED) is shown in figure 3.1(c), which verifies the single-crystallinity of the NW. To isolate a single NW for our study, we diluted the as-prepared NWs with ethanol and dropped on a silicon substrate. The sample

Chapter 3 *Surface enhanced Raman scattering and tip-enhanced Raman scattering study utilizing individual single crystalline silver nanowires*

was then spin-coated (600 rpm) with 1 mM 4-mercaptobenzoic acid (4-MBA). To minimize the laser induced photo-dissociation we attenuated the laser power to 0.1 mW and used a short integration time of 0.1 s.

3.1.3 Results and discussions

A typical SEM image of a single Ag NW is shown in figure 3.1(b), and the NW has a cone-shape apex. Raman imaging with incident laser polarized along (p-polarization) and perpendicular (s-polarization) to the long axis of the NW is performed to locate the apex of the NW and to study the distribution of Raman signal enhancement, especially around the tip apex. 4MBA has two characteristic peaks located at 1081 cm^{-1} and 1591 cm^{-1} , which have been assigned to the $\nu(\text{CC})$ ring-breathing modes of the molecule[161, 162]. The images plotted by the intensity of 4MBA Raman peak (1591 cm^{-1}) for both polarizations are shown in figure 3.2(a) and 3.2(c). For s-polarization, the intensity of 4MBA Raman peaks distributed uniformly along the body of the NW, in agreement with result reported by Mohanty et al.[163] On the other hand, for p-polarization, the image plotted by the same peak shows an extraordinary strong Raman signal emerging from the apex of the NW, the origin of which will be discussed later. This result is very repeatable; almost all the NWs prepared show such enhancement at the apex. For further evaluation, figure 3.2(e) shows the comparison of spectra obtained at the NW body, NW apex, and the silicon substrate with p-polarized laser. To our best knowledge, such strong enhancement at the apex of an NW has not been reported before.

Chapter 3 Surface enhanced Raman scattering and tip-enhanced Raman scattering study utilizing individual single crystalline silver nanowires

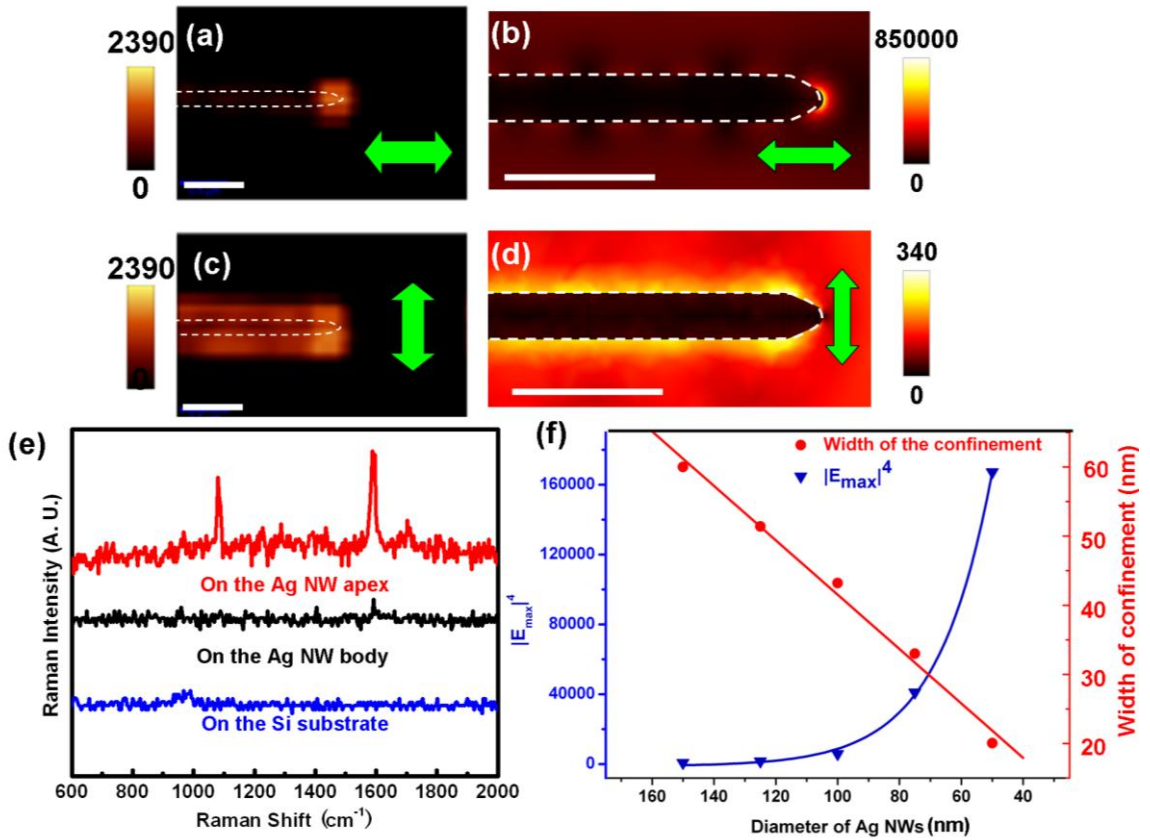


Figure 3.2 (a) and (c) are Raman images constructed by 4MBA Raman peak (located at 1591 cm^{-1}) with p-polarization and s-polarization, respectively. The white dash lines are guide for the eye showing the position of the NW. The white scale bar is $0.5 \mu\text{m}$. Comparison of FEM simulated field distribution in (b) p-polarization and (d) s-polarization. Please note the color scales are different for (b) and (d). (e) is the comparison of the Raman spectra collected at different positions with p-polarization. Figure (f) shows the simulation plot of the $|E_{\text{max}}|^4$ and FWHM of the localized EM field at the tip apex with p-polarization as a function of the function of the NW diameters.

Chapter 3 *Surface enhanced Raman scattering and tip-enhanced Raman scattering study utilizing individual single crystalline silver nanowires*

We attribute such Raman enhancement to the effect of excitation of LSP. When irradiated by a p-polarized laser, SP will be excited and localized in a small volume at the very end of the NW. Such highly confined localized EM field will interact with the analyte and enhance excitation and the scattered Raman signal. To demonstrate the EM enhancement localized at the apex of the NW, three-dimensional simulation by finite element method (FEM) has been conducted by using COMSOL MultiPhysics, AC/DC module. We simulated the Ag NW with a diameter of 150 nm, and at the apex of the wire the radius of curvature is 25 nm. For incident laser (wavelength = 532 nm) with different polarization, the intensive EM field is observed at different positions of the NW. The s-polarized light induces field enhancement at the sides of the NW body [figure 3.2(d)], while the p-polarized light reveals a much stronger field located at the apex of the NW [figure 2(c)]. The enhancement is most intense at the NW apex is due to the shape of the apex which provides a better concentration of the LSP. These results correspond well with our experiment observations.

To further study the size of the hot spot as a function of the NW diameter, we then extended our simulation to different diameters of Ag NWs. As the Raman enhancement is proportional to the $|E_{\max}|^4$ (E_{\max} is the maximum electric field intensity achieved at the apex of the NW), the $|E_{\max}|^4$ is then plotted in figure 3.2(f) in blue colored dots. To demonstrate the improvement of the spatial resolution, we also plotted the size of the confined EM field in figure 3.2(f) as red colored dots. From the curves we can see that for NW with smaller diameter, the EM field will be confined even more tightly, leading to a smaller and a more intensive field. For example, by decreasing the NW diameter

Chapter 3 *Surface enhanced Raman scattering and tip-enhanced Raman scattering study utilizing individual single crystalline silver nanowires*

from 150 nm to 50 nm, the size of the confined EM field is expected to be improved from 60 nm to 20 nm, at the same time, the Raman enhancement is expected to be increased by five orders of magnitude.

3.1.4 Conclusion

In summary, SERS at the end of individual single-crystalline Ag NWs have been observed by incident polarization along the NW axis. The enhancement is attributed to the LSP confined at the end of the NW, which is also demonstrated by FEM simulation. The enhancement factor of the end of the NW is shown to be much higher than that of the body of the NW. As the Ag NWs can be easily located by optical microscope, as well as the highly confined EM field is isolated in almost every tip of NWs, therefore, Ag NWs can be a perfect candidate to study the enhancement mechanism of the SERS effect. Not only restricted to certain size of Ag NWs, development in nanotechnologies has made different sizes of wires available. The simulation shows enormous enhancement is possible by using smaller Ag NWs. This shows a great potential for such noble metal NW in future SERS applications.

3.2 Tip-enhanced Raman scattering using individual single crystalline silver nanowire

3.2.1 Introduction

Chapter 3 *Surface enhanced Raman scattering and tip-enhanced Raman scattering study utilizing individual single crystalline silver nanowires*

Far-field micro-Raman spectroscopy has become an established characterization tool in both basic research and industrial applications, because it is non-destructive and provides chemical, physical and sometimes even electronic information. However, there are two limitations for its application in the emerging fields of nano-sciences and nano-technology: the sensitivity and the spatial resolution. Raman scattering is comparatively weak compared with other (nonlinear) processes. The Raman scattering cross-section is about 10 orders smaller than that of photoluminescence and 13 orders smaller than Rayleigh scattering. For this reason, it is very challenging to collect the extremely weak Raman features from the individual nanostructures. Besides this, the size of focal point for conventional far-field micro-Raman spectroscopy is in the scale of several hundreds of nanometers, governed by the diffraction limit. Such spatial resolution prevents Raman spectroscopy from probing individual nanomaterials and local properties which require a sub 100 nm or even sub 10 nm spatial resolution. Extensive efforts have been made on near-field scanning techniques to improve the sensitivity and spatial resolution [164-167]. Among these methods, TERS injects new vitality to the conventional Raman spectroscopy [7, 168-172].

TERS effect is normally attributed to the EM enhancement mechanism. By introducing a sharp metal tip, the LSP can be excited at the vicinity between the tip and sample. Such highly confined EM field can yield strong Raman signal (near-field signal) from the portion of the sample which is inside that tiny probing volume (10~100 nm). Lots of approaches have been made since the discovery of TERS effect. Metal coated tips of AFM [173, 174], etched metal wires [34, 175-178] and even metal nanospheres

Chapter 3 *Surface enhanced Raman scattering and tip-enhanced Raman scattering study utilizing individual single crystalline silver nanowires*

[179] have been demonstrated, and the best spatial resolution of ~10 nm has been reported [180]. Besides the ultra high resolution, TERS also has the ability to probe even single molecules[42, 181, 182], which has been directly shown by Pettinger's group recently [43]. At the moment, TERS is still one of the characterization techniques that are used by only a few in the research laboratories, as the experiments require very high degree of expertise and even though the success rate of TERS is extremely low. In order to make TERS a routine characterization technique in biology, physics, chemistry and even semiconductor industry, significant progress must be made. The main stumbling block for TERS application is therefore the fabrication of reproducible, reusable and highly active TERS tips.

Several types of TERS tips have been used in the literature. [35, 168, 183] For metal coated tips, a smooth metal (e.g. Au, Ag or copper) film is the main requirement and the size of the tip is greatly limited by the thickness of coated film. Besides this, such a thin film is very easy to wear off or oxidized [184]. Although etched tips do not have such "worn off" problems, producing reproducible sharp tips with a smooth surface is always complicated and the etching process may involve toxic chemicals [185]. More importantly, most of the tips prepared for TERS experiment utilize polycrystalline metal, which decreases the efficiency of LSP due to the scattering from the domain boundaries, roughness or defects[186]. Although some groups have used other approaches such as using the Au nanosphere or Si nanorods with Au caps [187] as TERS probes, complicated process and low yield are still yet to be solved.

Chapter 3 *Surface enhanced Raman scattering and tip-enhanced Raman scattering study utilizing individual single crystalline silver nanowires*

Noble metal NWs have always been attractive candidates to study SERS effect, as such nanostructures provide very strong Raman signal enhancement. Furthermore, noble metal NWs are also good models to fundamentally study the enhancement mechanism[163, 188-191]. Inspired by our results described in chapter 3.1, we have developed a simple and high yield method to produce reproducible highly efficient TERS probes. By means of applying such single-crystalline noble metal NW as TERS probes, the probe quality is ensured and the wear and tear problem can be overcome. Moreover, since the synthesis of metal NWs has been already well developed and different diameters of NWs can be easily achieved, the controlling of the probe size can also be bypassed[192-200]. In addition, recently, several methods have been reported to fabricate single-crystalline Au NWs with diameter of ~ 2 nm[201, 202]. By combining the achievement in NWs fabrication and the high surface plasmon efficiency of single-crystalline noble metal nanostructures, spatial resolution, signal intensity and reproducibility of TERS can be greatly improved.

3.2.2 Preparation of NW attached TERS tip and experimental setup

To manipulate such nano-scale Ag wires, we attach the NW to a W tip first. The W tips were fabricated by electrochemical etching process [203]. Many methods were attempted to attach the NWs, and we found that the alternating current dielectrophoresis (AC-DEP) technique is the simplest and most reliable one. The AC-DEP setup is illustrated in figure 3.3(a). A copper ring (2 mm, Agar Scientific) was used as one electrode, which was also used to hold the droplet of Ag NW solution. 10 μ L ethanolic

Chapter 3 *Surface enhanced Raman scattering and tip-enhanced Raman scattering study utilizing individual single crystalline silver nanowires*

solution of Ag NWs was dropped on the copper ring to form a droplet. The operation voltage is 10 V, 1 MHz. The W tip, as the other electrode, was then dipped into the droplet for ~1 second. After that, one or more Ag NWs will be attached on the W tip. One of the key issues to this AC-DEP method is the concentration of the NW solution. For an over diluted solution, it will be extremely difficult to attach the NWs to the W tip, whereas an over concentrated solution will attach multiple (sometimes more than 10) NWs to the tip. The optimized concentration (with success rate more than 50%) is found to be $\sim 1 \times 10^9$ NWs per liter. Figure 3.3(b) and 3.3(c) are the images taken by SEM showing a W tip with Ag NWs attached at the tip at different magnifications. Besides W tips, this method can also be used for most metal tips or metal coated AFM tips.

The TERS experiments were performed on the same Raman system. An ultra long working distance 80X objective lens with NA = 0.75 was used, so that the W tip can be placed between the objective and sample. The sample is a piece of Ag coated silicon

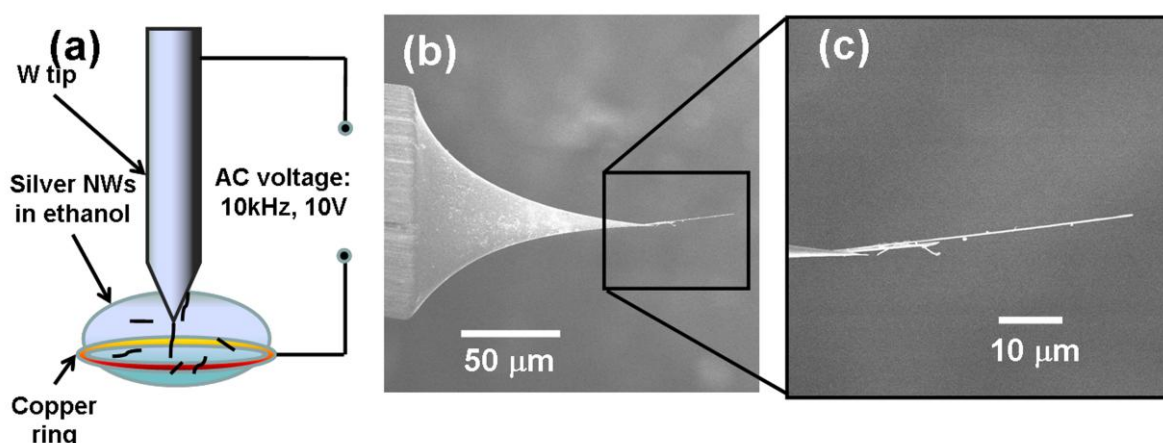


Figure 3.3 (a) illustration of the AC-DEP setup. (b), (c), SEM images of W tip with Ag NWs in different magnifications.

Chapter 3 *Surface enhanced Raman scattering and tip-enhanced Raman scattering study utilizing individual single crystalline silver nanowires*

with 1 μM 4MBA spin coated on top. It was placed on the piezo stage under the microscope and held at an angle of 45° to horizon in order to achieve a reflection setup. The Ag NW tip was then mounted on the nanomanipulator (Kleindiek MM3A-EM). The experimental setup was illustrated in figure 3.4.

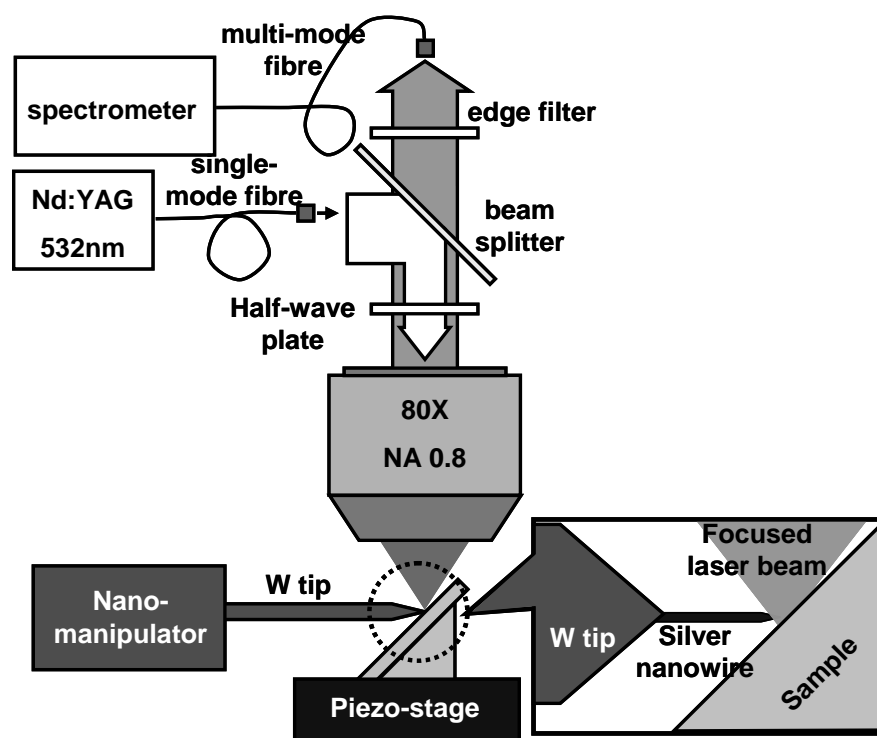


Figure 3.4 Schematic diagram of experiment setup for our TERS experiment.

In our experiment, the Ag NW was brought into the focused laser spot (size ~ 500 nm) by using the nanomanipulator. We approached the sample surface to the Ag NW tip with

Chapter 3 *Surface enhanced Raman scattering and tip-enhanced Raman scattering study utilizing individual single crystalline silver nanowires*

a constant step size of 10 nm. Raman spectra were collected at each step. The integration time for each Raman spectrum was 0.5 s. We did not use any feedback system while approaching the sample, thus we can only estimate the tip-sample contact point from the signal enhancement of Raman peaks from the analyte, which will be discussed latter.

3.2.3 Results and discussion

Figure 3.5 shows the Raman spectra of the sample in different conditions. As discussed before, the TERS enhancement is greatly related to the polarization direction of the incident laser[204]. The black curve is the Raman spectrum collected on sample surface with the apex of Ag NW retracted 1 μm away (p-polarization). The other two curves show the Raman spectra collected when Ag NW is very close to sample surface (distance less than 10 nm) with incident laser (red) in p-polarization and (blue) in s-polarization. The blue and black curve shows similar weak Raman intensity while a ~ 10 times stronger intensity observed in the red curve. These spectra obtained by TERS agree well with that of SERS experiments and our simulation. Figure 3.6 compares spectra collected by TERS and SERS to that of the pure 4MBA molecules. In the figure, both TERS and SERS spectra show the two characteristic peaks ($\nu(\text{CC})$ ring-breathing modes) of 4MBA and a less intense Raman band at $1130\text{--}1180\text{ cm}^{-1}$ ($\delta(\text{CH})$ mode) [161, 162]. The observed characteristic peaks of 4MBA remain in the same position in SERS and TERS, which are slightly different from that of the bulk molecule. Such differences in peak position and intensity can be attributed to the intrinsic properties of EM enhancement [168] and the absorption state of the 4MBA molecule [205]. In our TERS

Chapter 3 *Surface enhanced Raman scattering and tip-enhanced Raman scattering study utilizing individual single crystalline silver nanowires*

experiment, the spectra collected sometimes reveals some new Raman features in between 1000 to 2000 cm^{-1} . The additional features appear not only while using different Ag NWs for TERS tip, but even for two different approaches with the same Ag NW tip. The appearance of these extra peaks is believed to be originated from local carbonic surface contamination or degradation of the analyte.

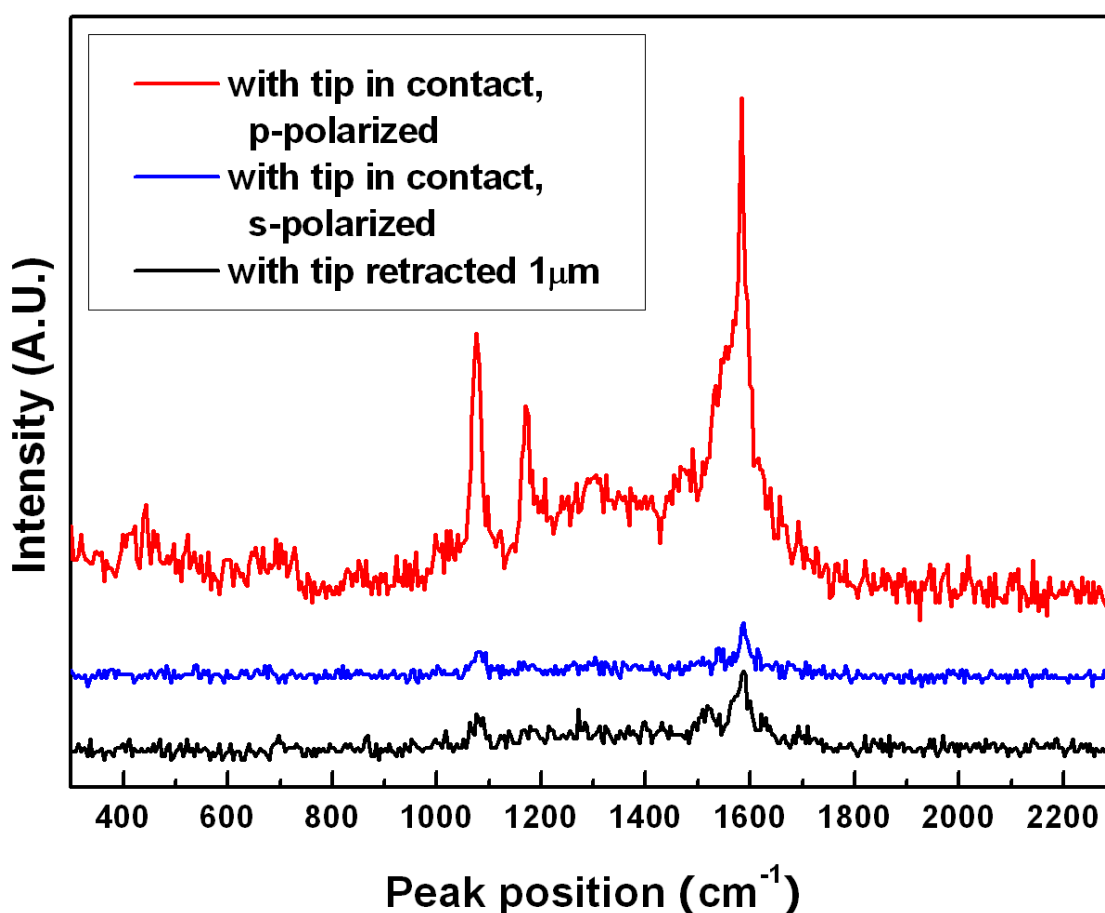


Figure 3.5 Comparison of the Raman spectra. Tip in contact with sample surface with p-polarized incident laser (as red curve). Tip in contact with sample surface with s-polarized (as blue curve). Tip retracted about 1 μm from sample surface with p-polarized incident laser (as black curve).

Chapter 3 Surface enhanced Raman scattering and tip-enhanced Raman scattering study utilizing individual single crystalline silver nanowires

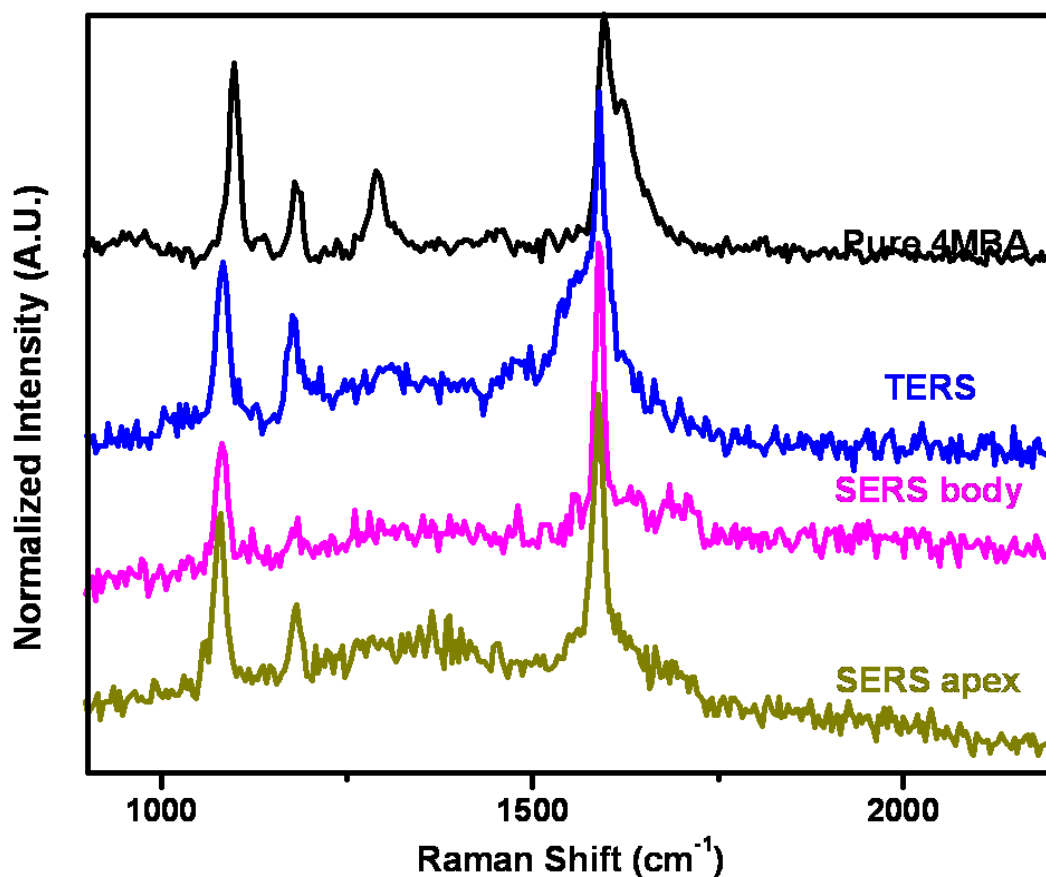


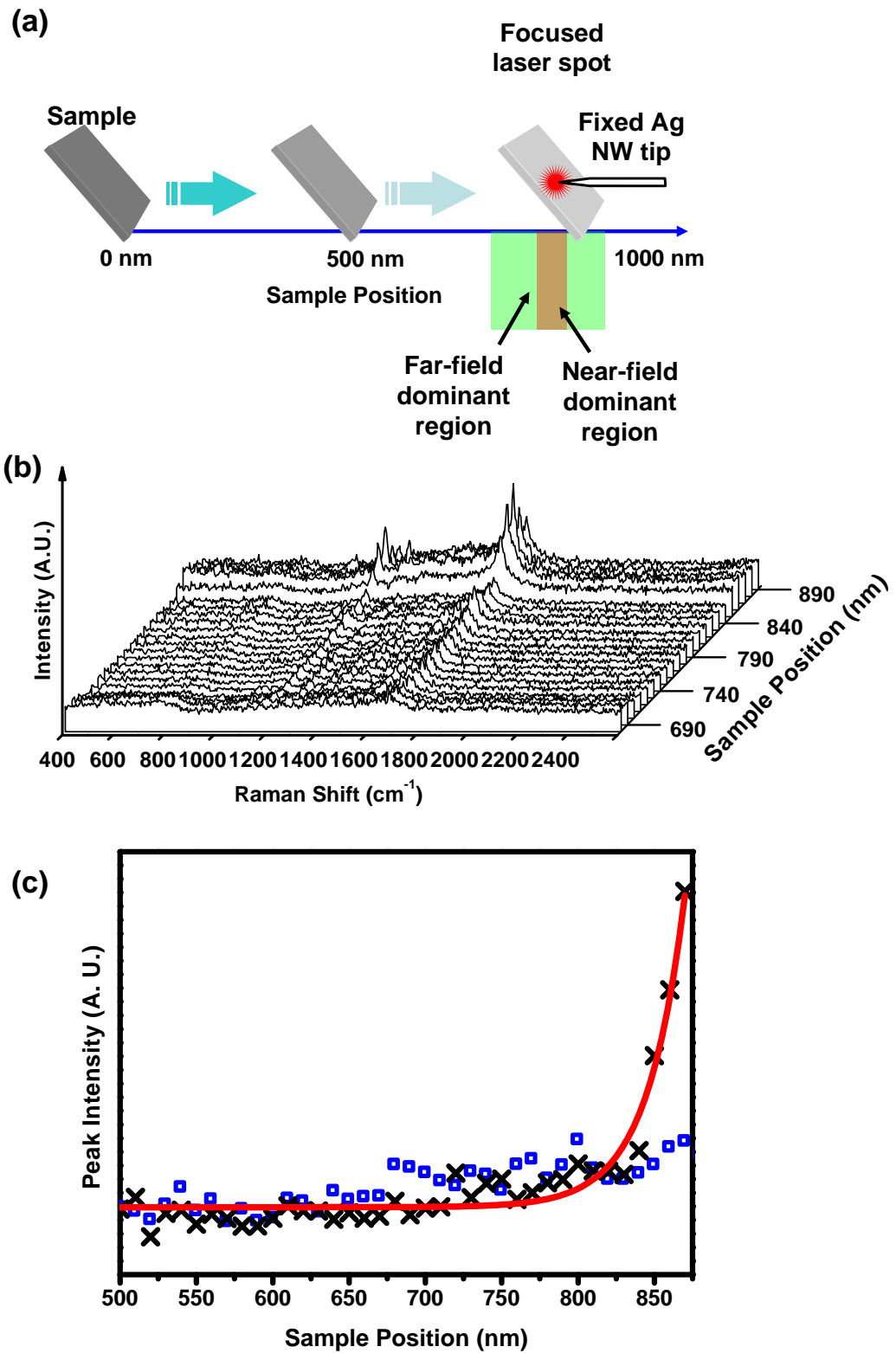
Figure 3.6 Comparison between spectra obtained on bulk 4MBA molecule, TERS and SERS spectra on different spot of the Ag NW. All spectra are normalized by the Raman feature near 1590 cm^{-1} .

In order to study the signal enhancement as the function of tip-sample distance, we studied the Raman spectra while approaching the sample to tip. The sample surface was placed around $1\text{ }\mu\text{m}$ away from the end of the Ag NW. The sample was then driven towards the tip with a step size of 10 nm , as illustrated in figure 3.7(a). Raman spectrum was collected in each step with 0.5 s integration time.

Chapter 3 *Surface enhanced Raman scattering and tip-enhanced Raman scattering study utilizing individual single crystalline silver nanowires*

The approaching has been carried out several times for different sample position and different Ag NW tips. One set of typical approaching result is shown in figure 3.7. The spectra collected are piled up for the sample position in the range of 690-890 nm in figure 3.7(b). From the figure, a weak Raman feature of 4MBA is barely observed when sample position is 690 nm, as the sample just entered the far-field dominant region. The increase of the Raman intensity is slow until the sample position is larger than 830 nm. From 840 nm to 870 nm is the near-field dominant region, in which the sample surface starts to interact with the apex of the tip. A rapid increase in Raman intensity is observed due to the presence of the tip. In figure 3.7(b), we only observe a rise of the baseline uniformly in all the spectra but no obvious changes of the position and intensity of the spectrum background as mentioned by other people. The origin of the spectrum background in TERS has been detailed studied [206], and it is believed that the position of the background reflects the energy profile of the LSP. For our experiment setup, the calculated LSP resonance is in between 400-500 nm region[207], which suggests with our excitation laser at 532 nm it is at the low energy tail of the LSP profile. Thus the background is rather flat and shows little fluctuation in our observation.

Chapter 3 *Surface enhanced Raman scattering and tip-enhanced Raman scattering study utilizing individual single crystalline silver nanowires*



Chapter 3 *Surface enhanced Raman scattering and tip-enhanced Raman scattering study utilizing individual single crystalline silver nanowires*

Figure 3.7 (a) An illustration of the approaching process. (b) A typical set of data collected while approaching sample towards the Ag NW tip. For a clear view, only data inside the far-field/near-field dominant region are plotted. (c) Curve fitted Raman intensity of 4MBA Raman peak (1591 cm^{-1}) as a function of sample position. The black crosses are data obtained with tip in focus and the blue squares are data obtained with the absence of tip. The experiment data with tip is also fitted by function of exponential growth (red curve).

The characteristic peak of 4MBA (1591 cm^{-1}) in each spectrum is then fitted by Lorentzian distribution, and the peak intensity is plotted as a function of the sample position as the black dots in figure 3.7(c). A rapid increase followed by a sudden drop down in intensity can be observed while moving the sample surface towards the Ag NW tip in the near-field dominant region. As there is no feedback, the exact tip-sample distance cannot be measured. We then assume for the point with the highest Raman intensity (sample position = 870 nm), the tip-sample distance is the smallest (<10 nm). After the sample touched the tip, the tip will be bent or drifted, causing the sudden decrease of the Raman intensity. Owing the fact that TERS is a near-field effect, its enhancement is expected to increase exponentially while decreasing the tip-sample distance. The trend is well fitted by the exponential growth function with a growth length of 24 nm. Such rapid increase can serves as an evidence of the tip enhancement[50]. For different Ag NW tips, the growth length varies from ~25 nm to ~40 nm, as this growth

Chapter 3 Surface enhanced Raman scattering and tip-enhanced Raman scattering study utilizing individual single crystalline silver nanowires

length is found closely related to the radius of curvature of the tip. To compare the TERS results to the far-field results and further verify the effect of the Ag NW, the tip was retracted several micrometers away from the laser beam, and the sample approaching was repeated in the same manner. In this sense, the Raman signal collected is a pure far-field product. The intensity of 4MBA peak is plotted in figure 3.7(c) as blue squares. This time, the Raman peak intensity increases very little and the increase starts when the tip-sample distance is less than ~ 300 nm. The maximum Raman intensity in the absence of tip is much weaker than that with the presence of tip.

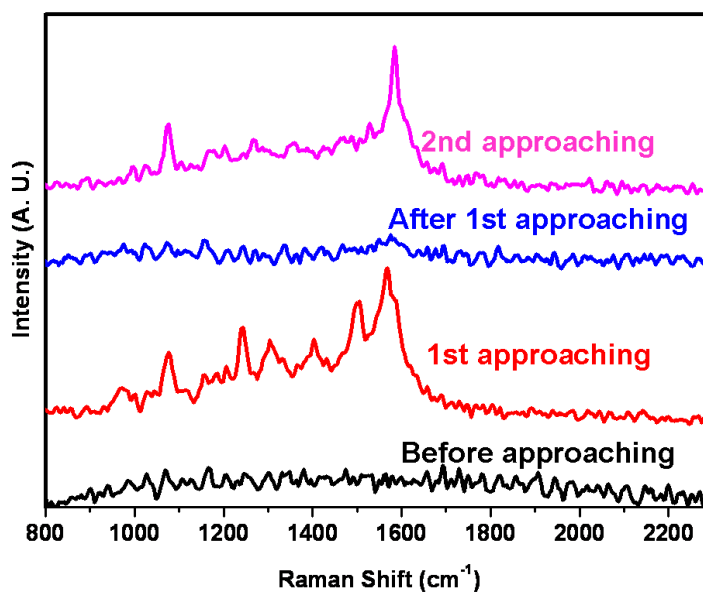


Figure 3.8 Comparison of spectra collected on the tip apex before and after a TERS approaching. The black curve is the spectrum collected on sample alone before the TERS experiment. The TERS spectrum obtained in the first approaching is shown in red color. Spectrum of the same Ag NW tip after the first approaching is shown in blue curve. Result acquired in second approaching is shown in purple color.

Chapter 3 *Surface enhanced Raman scattering and tip-enhanced Raman scattering study utilizing individual single crystalline silver nanowires*

Raman study of the apex of the Ag NW TERS tip has also been carried out to verify the reusability of the tip. As shown in figure 3.8, black curve was collected on the apex of the tip along before a TERS experiment as a reference. Then the tip was mounted on the nanomanipulator and performed the TERS approaching. The red colored curve is the data collected while tip-sample distance is the smallest. After the first approaching, the sample was retracted and spectrum was collected on the same spot of the tip, and once again, the second TERS approaching was performed towards a different position of the sample surface. By comparing the spectra of the tip only, we believe that the TERS signal observed is originated from the 4MBA molecule on the sample surface due to TERS effect but not molecules or contaminations adsorbed on the tip due to the SERS effect. Furthermore, besides the normal 4MBA characteristic peaks, some additional Raman features can be seen in the first TERS spectrum. These features are not coincidence with any reported 4MBA Raman spectra, suggesting the appearance of some contaminations on the sample surface. But the second TERS spectrum shows rather pure 4MBA Raman features. We can then conclude that the Ag NW tip did not pick up or transfer the surface molecule and even contamination molecules. After the TERS approaching, the Ag NW tip is still “clean”. We need to emphasize that the adhesive force between NW and tip is very strong and the NW does not drop off even though the sample surface was pressed against it for as far as 1 μm . The success rate of this method is very high and the same NW can be used many times.

3.2.4 Conclusion

Chapter 3 *Surface enhanced Raman scattering and tip-enhanced Raman scattering study utilizing individual single crystalline silver nanowires*

In conclusion, the strong Raman enhancement at the apex of individual single crystalline Ag NW has been studied. Using AC-DEP, we applied such NWs as TERS probes and demonstrated the TERS effects. The result is very promising and it shows that, by combining the mature metal NW fabrication techniques and the TERS technique, a highly repeatable and much simplified near-field Raman spectroscopic technique can be expected.

Chapter 4

Mechanically held Microsphere-enhanced Raman spectroscopy/imaging

4.1 Introduction

As described in previous chapter, in order to improve Raman spectroscopy/imaging to meet the increasing demand of studying nano-materials, extensive efforts have been made to reduce the spatial resolution below the diffraction limit by using scanning near-field optical microscopy (SNOM). TERS is the preferred choice for performing near-field Raman scattering and ~10 nm spatial resolution has been achieved [208]. However, TERS also has its severe limitations. Fabricating an effective and reliable tip, by which strongly enhanced EM field can be excited on the apex of the tip is the key issue to the reproducibility of TERS experiments. But the preparing method for such a small tip with highly controlled geometry and quality is still not available. Besides this, TERS tip also faces wear-tear and oxidation problems, which limit the tip's reusability [35, 168, 183, 184]. These problems must be overcome before TERS become a routine tool in nano-science and nano-technology. One of promising approaches in controlling the geometry of the tip is by using NW. In our previous works, single crystalline silver NWs have been shown to be a good candidate to achieve controllable and reproducible "hot" tip for successful TERS experiments.

Other than utilizing the EM enhancement induced by the noble nanostructures, we have developed another approach, which utilizes the near-field focusing power of a

Chapter 4 *Mechanically held microsphere-enhanced Raman spectroscopy/imaging*

micrometer-size dielectric sphere to achieve high S/N ratio and further improve the spatial resolution. In this technique, the laser is focused to a spot smaller than 200 nm by a dielectric microsphere. The microsphere is then held either mechanically or by optical tweezing, while Raman imaging is performed by scanning the sample. With the help of the microsphere, both the spatial resolution and the S/N ratio can be greatly enhanced.

4.2 Preliminary works

In this part, the experiment setup and results of the Raman enhancement study with the optically trapped sphere are discussed. Although this chapter focuses on the mechanical held microsphere, the preliminary works here are included as the motivation of my works and a brief introduction of the microsphere-enhanced Raman techniques as well. For readers who are interested in Raman enhancement from the optically trapped microsphere, please refer to our published journal article[167] and thesis of Johnson Kasim for more comprehensive information.

In this part, we show by employing an optically trapped a dielectric microsphere the spatial resolution is greatly improved and Raman signal collected is always much stronger than that without microsphere, by 2-7 times depending on the diameter of microsphere used. Taking advantages of high reproducibility, strong near-field Raman signal and the simplicity, this microshpere-enhanced Raman spectroscopy technique gains great potential as a future characterization tool.

Chapter 4 Mechanically held microsphere-enhanced Raman spectroscopy/imaging

4.2.1 Experimental

The preliminary study features the optically trapped sphere, whose role can be understood as a micro-lens in Raman imaging. In this part, besides the excitation source for Raman spectroscopy, the focused incident laser beam is also used to hold the microsphere above the sample surface through the scanning, by the optical tweezers mechanism, as illustrated in figure 4.1. Raman spectra were collected in each step, while scanning the sample. At last the spectral information of each spectrum will be extracted and used to construct the Raman image.

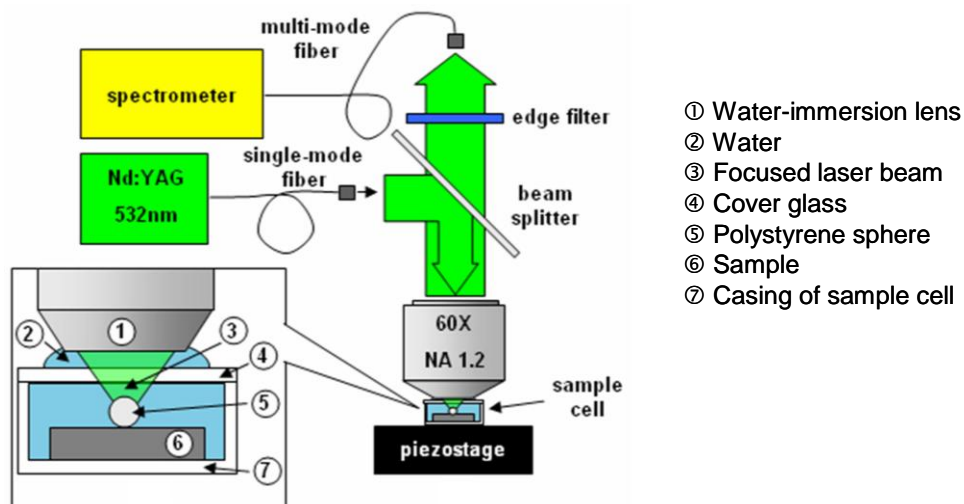


Figure 4.1 The schematic diagram of the microsphere enhanced Raman Spectroscopy (spheres trapped by optical tweezers). Adapted from Kasim J. et al.[167]

Chapter 4 *Mechanically held microsphere-enhanced Raman spectroscopy/imaging*

4.2.2 Results and discussion

Real semiconducting devices of transistors with SiGe source drain stressors and poly-Si gate was employed as a test structure. By the help of the optically trapped microsphere, we can well resolved the strain distribution on the 65 nm device lines with much improved repeatability and excellent S/N ratio. It is nearly impossible for conventional confocal microscopy to study such small feature.

Figure 4.2(a) and 4.2(b) show the Raman spectra obtained from the SiGe stressor region and the poly-Si gate region, respectively. Each spectrum was curve-fitted with three Lorentzian peaks, as shown in figure 4.2(a): the Raman band located at 510.4 cm^{-1} corresponds to the Si-Si bond vibrations from the SiGe stressor, the band at 518.9 cm^{-1} indicates the tensile-strained Si just below the SiGe, and the band at 520.6 cm^{-1} is from the relaxed Si substrate below the structures, respectively. Similarly, in Figure 4.2(b), the Raman band from Si-Si bond vibrations of poly-Si locates at 516.3 cm^{-1} , the Raman band located at 520.6 cm^{-1} is the bulk Si below, and another one is from compressively strained Si in the channel region (522.1 cm^{-1}).

We carried out the Raman line scan on the above structures with the optically trapped microsphere. The results are shown in figure 4.2(c). The intensity profile of the of Si-Si peak from the SiGe (yellow color) and the Si-Si peak position profile from the bulk Si (purple color) are superimposed on the SEM image of the tested area. It can be seen in the figure that the results show excellent correspondence with the device structure with good S/N ratio. The SiGe stressor lines can be well resolved which is impossible for a same scan without the microsphere.

Chapter 4 Mechanically held microsphere-enhanced Raman spectroscopy/imaging

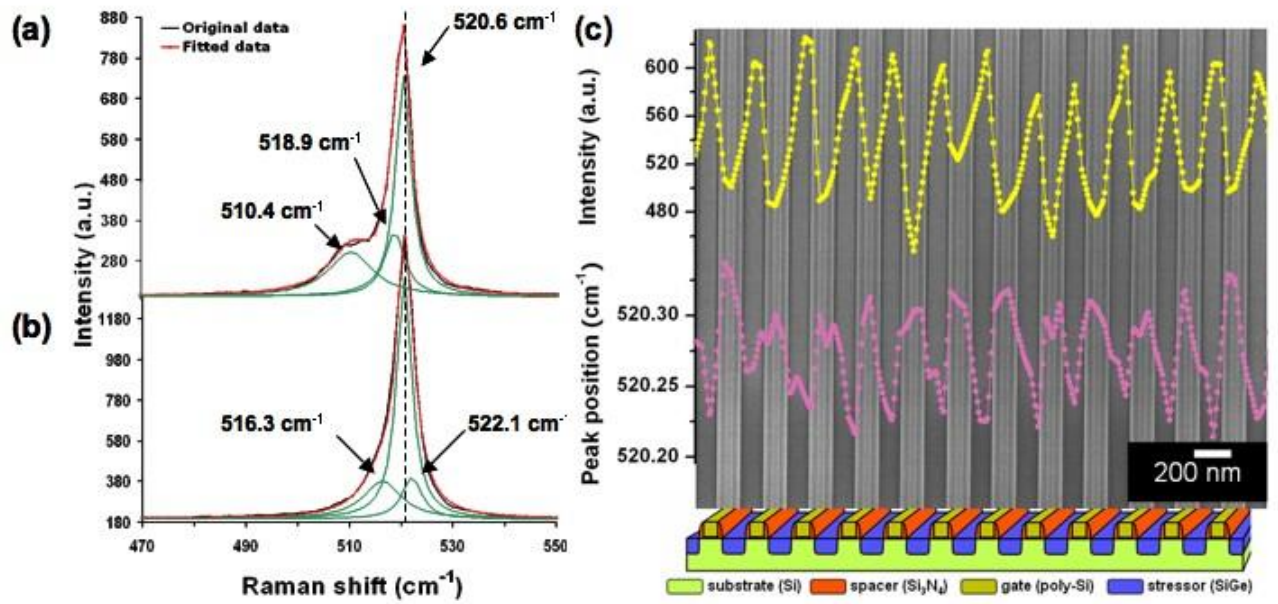


Figure 4.2 The Raman spectra from (a) SiGe and (b) poly-Si lines with fitted peaks using Lorentzian function. In spectrum a, the Raman peak at 510.4 cm^{-1} corresponds to Si-Si phonon vibrations from SiGe, while the peaks at 518.9 and 520.6 cm^{-1} belong to tensile-strained Si just below the SiGe and the bulk Si substrate, respectively. In spectrum b, the Raman peaks at 516.3 , 520.6 and 522.1 cm^{-1} correspond to Si-Si phonon vibrations of poly-Si, bulk Si substrate and compressively strained Si in the channel region, respectively. (c) SEM image with cross-section view diagram of periodic tested structure. Line-profile of Raman Si-Si peak intensity from SiGe is shown in yellow color, and the Si-Si peak position from the bulk Si is in purple color. The line scans show excellent correspondence with the structure. Adapted from Kasim J. et al.[167]

Chapter 4 *Mechanically held microsphere-enhanced Raman spectroscopy/imaging*

Besides the Si based devices, we have also performed Raman mapping on gold nanopatterns and CNTs (the results are not included in this thesis). All those tests provide good reproducibility of this technique.

4.2.3 Conclusion of preliminary works

Our study showed the optically trapped microsphere-enhanced Raman imaging has a very high spatial resolution and S/N ratio comparing to normal confocal Raman imaging. It is also very simple and practical. But there is still some problems need to be addressed, which will be discussed in the introduction of the next part.

4.3 Raman enhancement study from mechanically held dielectric microspheres

4.3.1 Introduction

Although using optical tweezers to hold the microsphere has many advantages, there are still some problems needed to be concerned. As the spheres and samples are immersed in water, study of dissolvable samples may be challenging and the Brownian motion of the microsphere also affects the spatial resolution of Raman imaging. Liquid (such as water) may also introduce undesirable doping or contamination to the sample. Besides these, in liquid environment, in-situ studies like applying current or changing temperature are almost impossible. Thus we like to develop an alternative approach to

Chapter 4 *Mechanically held microsphere-enhanced Raman spectroscopy/imaging*

hold the sphere in a more stable, controllable and liquid-free method – using either tailored AFM cantilever or ATEC (Advanced Tip at the End of Cantilever) tip.

Before the study on Raman enhancement, efforts are made to attach the sphere on the cantilever/tip. As the sphere and cantilever/tip are extremely small, micro-scale manipulation processes is necessary as discussed in chapter 4.3.2.

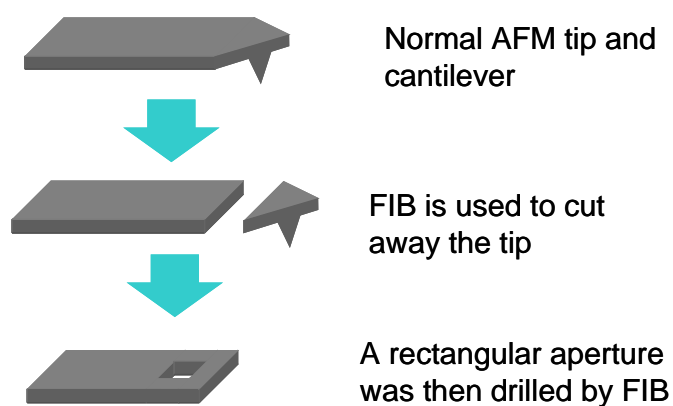


Figure 4.3 Illustration of tailoring normal AFM tip by FIB.

4.3.2 Attaching the sphere to the cantilever/tip

Preparation of the tailored cantilever

Before attaching sphere, normal AFM cantilevers were tailored by focused ion beam (FIB) to cut away the tip and drill an aperture to mount the microsphere, as illustrated in figure 4.3, while this step is not necessary for the ATEC tip.

Attaching the microsphere

A pair of nano-manipulators (Kleindiek MM3A-EM) was employed to manipulate the microsphere under an optical microscope. The nano-manipulator is driven by piezo

Chapter 4 *Mechanically held microsphere-enhanced Raman spectroscopy/imaging*

crystals, which allow a smooth movement with three degrees of freedom (vertical swing, horizontal swing and retraction/extension). The tungsten tip is mounted on the manipulator which serves as the hand to transfer the sphere. Such W tip is fabricated by electrochemical etching process using 5 M KOH solution with 10 V operating voltage[203]. By controlling the etching condition, tip with different radius of curvature ranging from ~50 nm to 1 μm can be fabricated.

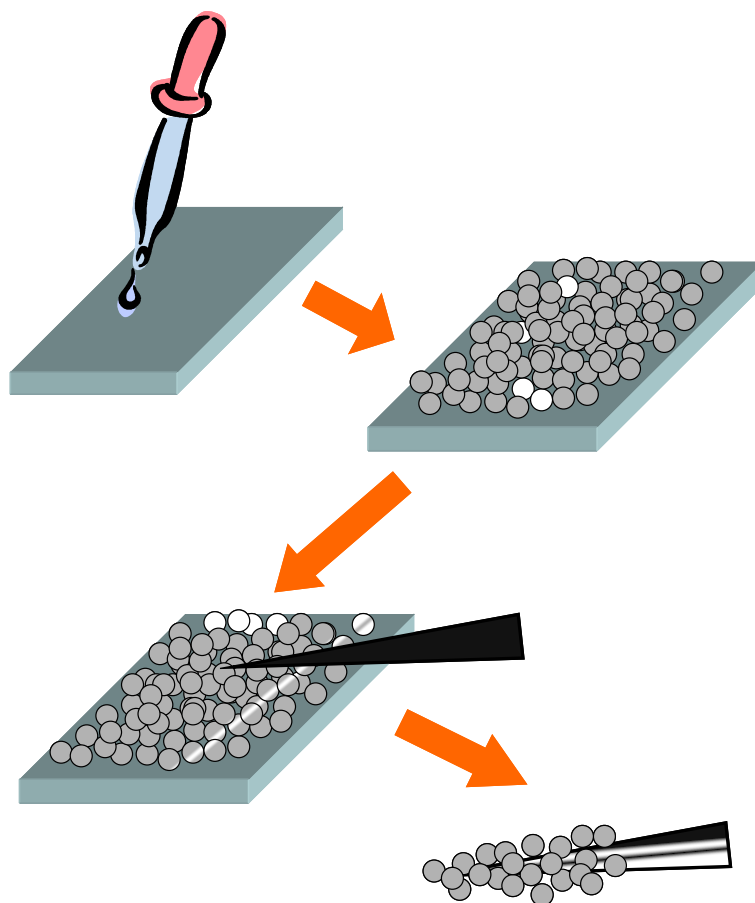


Figure 4.4 Schematic diagram of picking up microspheres by a W tip operated by nanomanipulators.

Chapter 4 *Mechanically held microsphere-enhanced Raman spectroscopy/imaging*

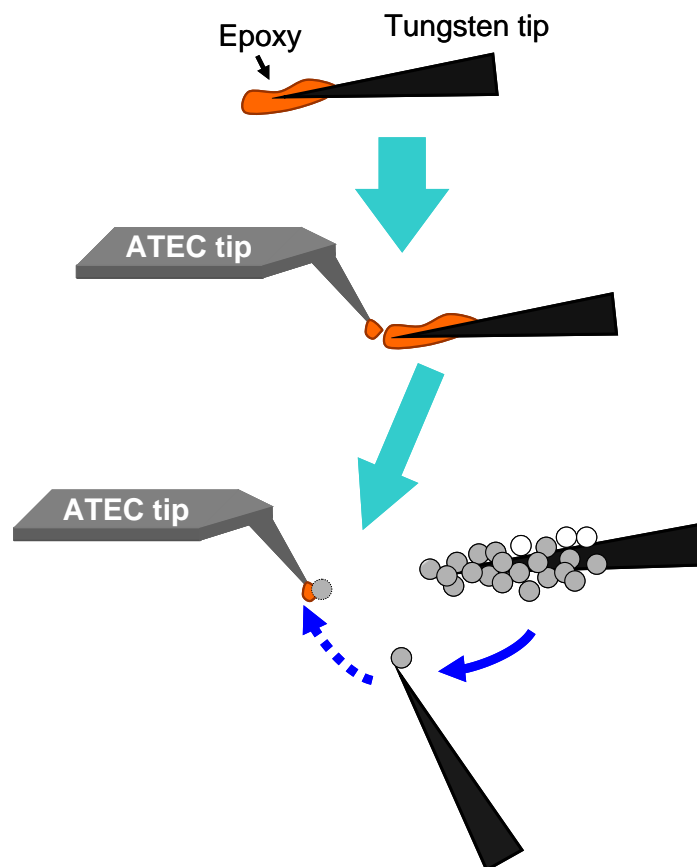


Figure 4.5 Sphere mounting process.

Firstly, the microsphere solution was drop and dry on a glass slide, then around 100 spheres were pickup by a tungsten tip for the next step of attaching, as illustrated in figure 4.4.

Chapter 4 Mechanically held microsphere-enhanced Raman spectroscopy/imaging

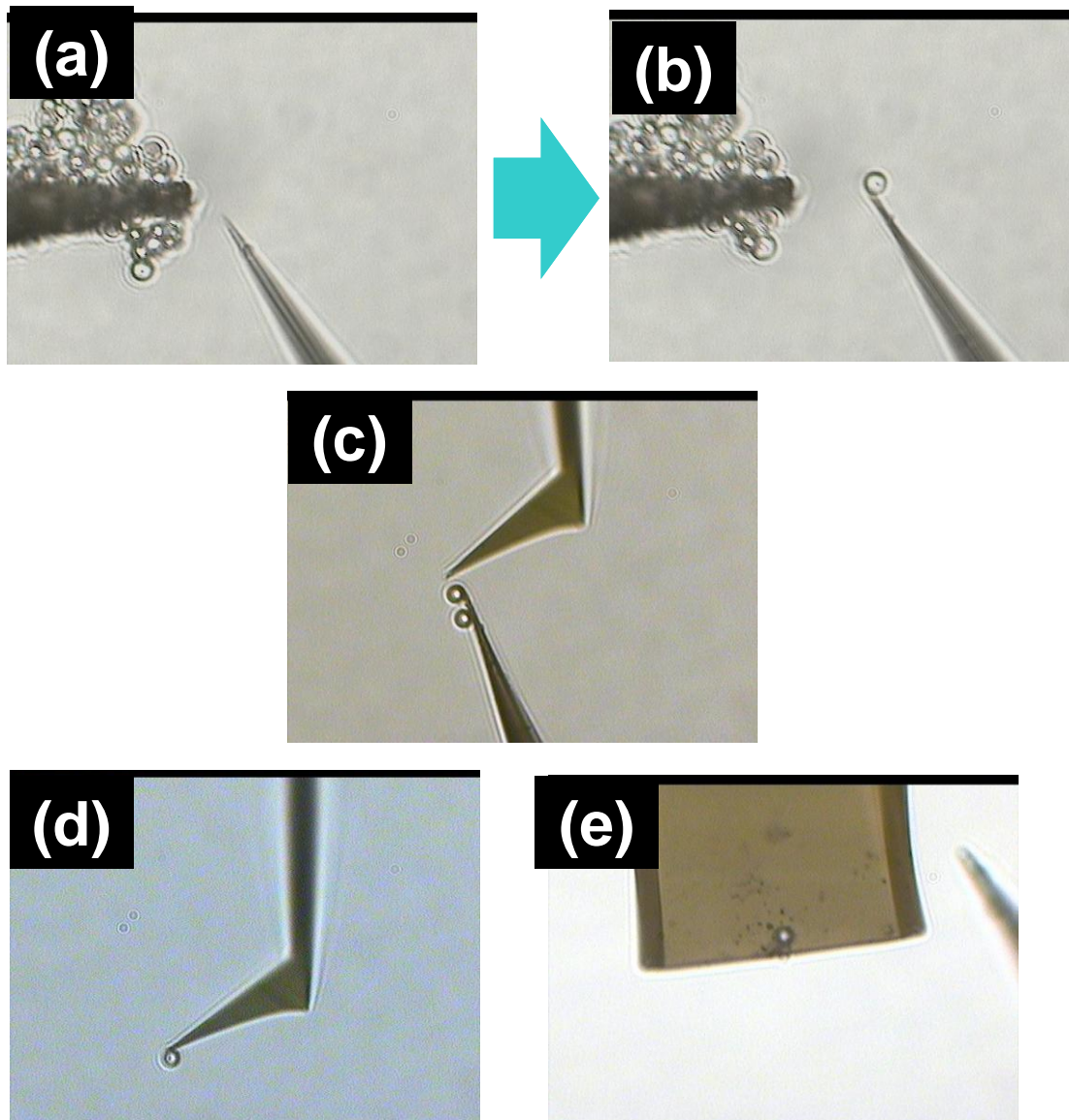


Figure 4.6 Optical images of the mounting process. Figure (a) and (b) show one microsphere is picked up by a W tip. (c) A W tip transferring a sphere to the end of the ATEC tip. The sphere attached (d) ATEC tip and (e) tailored AFM tip.

The next process is to transfer the sphere to the cantilever/tip. This step is very crucial, because in Raman scanning, the sphere will be hold to touch/scratch against the

Chapter 4 *Mechanically held microsphere-enhanced Raman spectroscopy/imaging*

sample surface, thus the attached sphere must be well stabilized and has enough mechanical strength to avoid dropping off or drifting during the scanning. In order to achieve this requirement, “glue” is necessary to ensure a stable attachment of the sphere. After several attempts, epoxy glue was chosen not only because of its high mechanical strength but also for the purpose of minimizing the PL and Raman signal produced by the glue. As shown in figure 4.5, firstly, a tungsten tip picks up small amount of epoxy. Secondly, the epoxy is carefully spread to the end of the ATEC tip. The tungsten tip with many sphere attached on it is then brought to the ATEC tip. Finally, a clean and sharp tip transfers one sphere to the end of the ATEC tip. For tailored cantilever, the above process is the same. After all, the sphere attached cantilever/tip is baked in oven at 150 °C for 30 min to harden the epoxy glue.

Figure 4.6 shows optical images captured during the process and images of sphere attached cantilever/tip.

Testing the as-prepared sphere attached cantilever/tip

Before practically using sphere attached cantilever/tip, the mechanical strength is tested first under the microscope by the nanomanipulator. In such test, tungsten tips controlled by nanomanipulator touch and push each sphere to ensure they are well attached. Besides the mechanical testing, spectral testing is also carried out on the attached microsphere to ensure that the attaching process does not introduce contaminations which produce extra Raman peaks. Figure 4.7 shows the spectrum collected from polystyrene microsphere attached on cantilever with 10 s integration time, a spectrum collected under the same condition from bulk Si substrate is also included as

Chapter 4 Mechanically held microsphere-enhanced Raman spectroscopy/imaging

a comparison. There is no obvious Raman peak induced by the attaching process. The Raman features from the Si cantilever and the polystyrene are shown in the zoom-in inset.

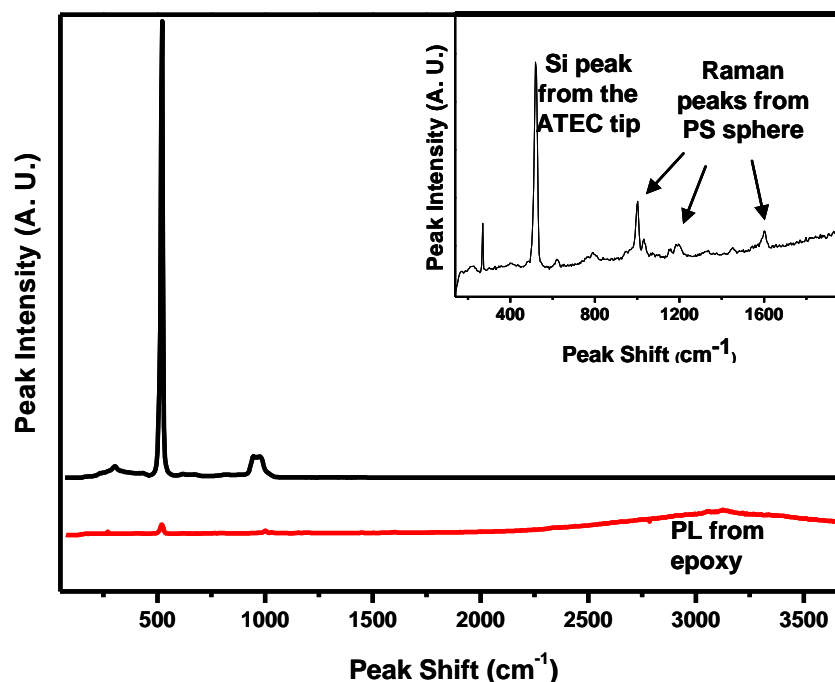


Figure 4.7 Spectrum collected on the Si substrate (black) and the as attached microsphere (red). The inset is the zoom-in view of the spectrum of the microsphere.

4.3.3 Microsphere-enhanced Raman imaging

Figure 4.8 illustrates the experiment setups of the mechanically held microsphere-enhanced Raman imaging. The tested sphere attached cantilever/tip can then be mounted to the cantilever holder (figure 4.9) installed on the objective lens to perform Raman imaging. The cantilever can be moved in three directions as respected to the objective lens, so that the excitation laser can be focused on the microsphere (through the

Chapter 4 Mechanically held microsphere-enhanced Raman spectroscopy/imaging

aperture, in the first case). Then the objective lens moves down with the sphere. After the sphere touches the sample surface, a fine adjustment of the sphere position will be performed and monitored by the Raman signal from the sample. At last the sample is then scanned to carry out the Raman imaging process as normal.

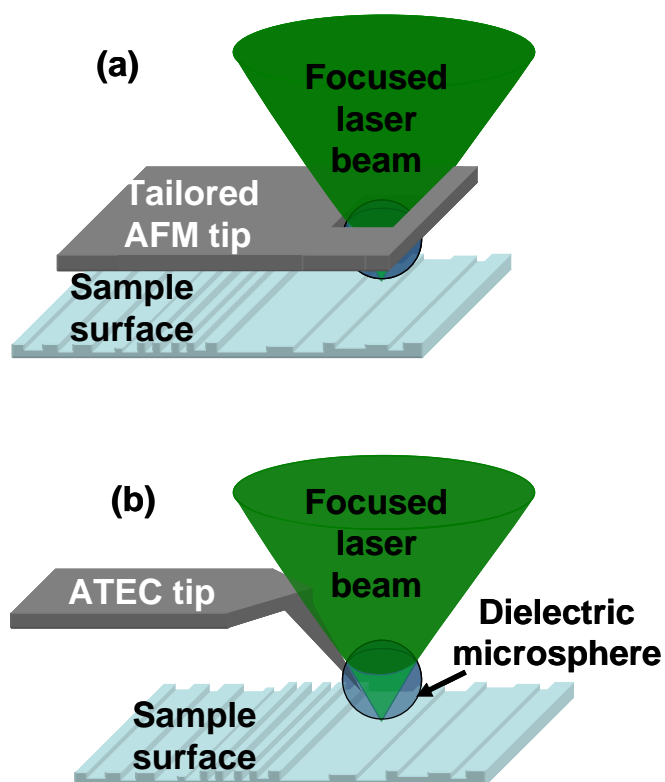


Figure 4.8 Illustration of the experiment setup. (a) The sphere mounted tailored AFM cantilever and (b) the sphere mounted ATEC tip.

Chapter 4 *Mechanically held microsphere-enhanced Raman spectroscopy/imaging*

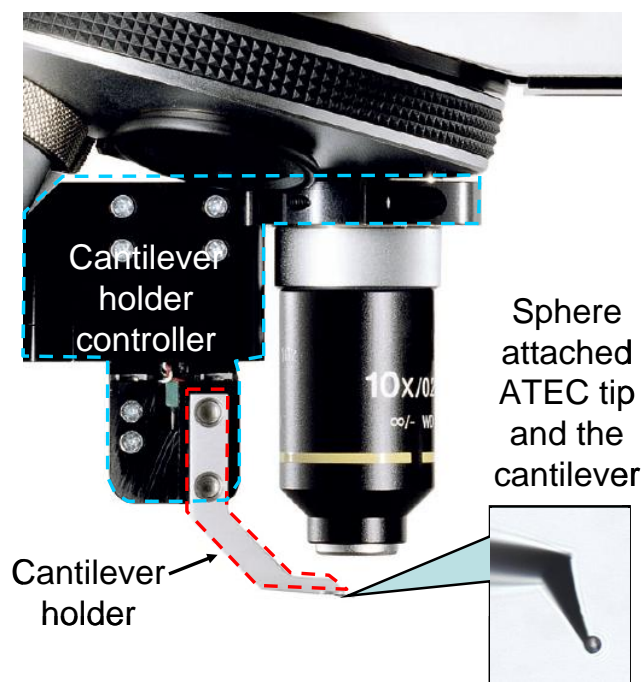


Figure 4.9 The cantilever holder is mounted on the objective lens. The cantilever can be moved by such holder in three directions under the microscope.

As the development of microsphere-enhanced Raman imaging (hold by cantilever/tip) is still in progress, the experiment condition has not been optimized yet. In this stage of experiment, no feed-back system is employed as the common SNOM experiment, thus the sphere is actually pressed against the sample surface.

Figure 4.10(a) shows the results of Raman imaging with a 3 μm polystyrene sphere held by tailored AFM cantilever. The sample is the same as preliminary works using optically trapped sphere. The objective lens is 20X with NA of 0.4. Another Raman image was done on the same region without using sphere is shown in figure 4.10(b) as a comparison. It is very clear that the Raman imaging with microspheres held by cantilever provides a much better spatial resolution, and the vertical SiGe stressors can be well resolved. Although the data obtained using mechanically held sphere is not as good as

Chapter 4 Mechanically held microsphere-enhanced Raman spectroscopy/imaging

previous data using optically trapped sphere in terms of spatial resolution, it demonstrates the potential and applicability of using such mechanically held sphere to perform Raman imaging nonetheless.

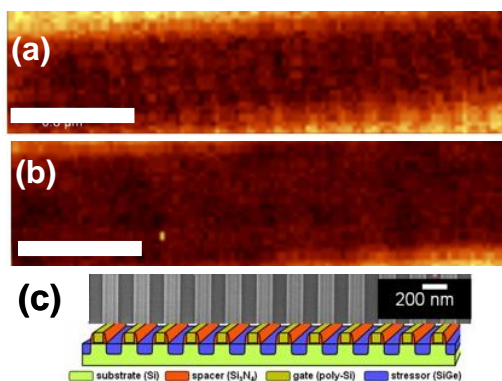


Figure 4.10 Raman image constructed by intensity of Si peak (a) with using sphere attached cantilever and (b) without using any sphere. Both scale bars are 1 μm . Figure (c) is a SEM picture showing the vertical SiGe stressors and a cross-sectional diagram of the sample structure.

Besides the promising results obtained, there are still some unsolved problems. First of all, the aperture of tailored cantilever needs to be improved to adapt to microsphere with smaller size ($<3\ \mu\text{m}$). As illustrated in figure 4.11(a), the current aperture for spheres less than $3\ \mu\text{m}$ is too small to let the focused laser pass through. An aperture with the cross-sectional shape like figure 4.11(b) should be used to overcome this problem. Secondly, limited by our system, the AFM cantilever can only be used with 20X objective lens. Better spatial resolution is expected while using an objective lens with higher NA (e.g. 80X with NA 0.75). Furthermore, a feedback system to control the

Chapter 4 *Mechanically held microsphere-enhanced Raman spectroscopy/imaging*

distance between the microsphere and the sample surface should also be employed in order to get the ultimate results. However, this will increase the cost significantly.

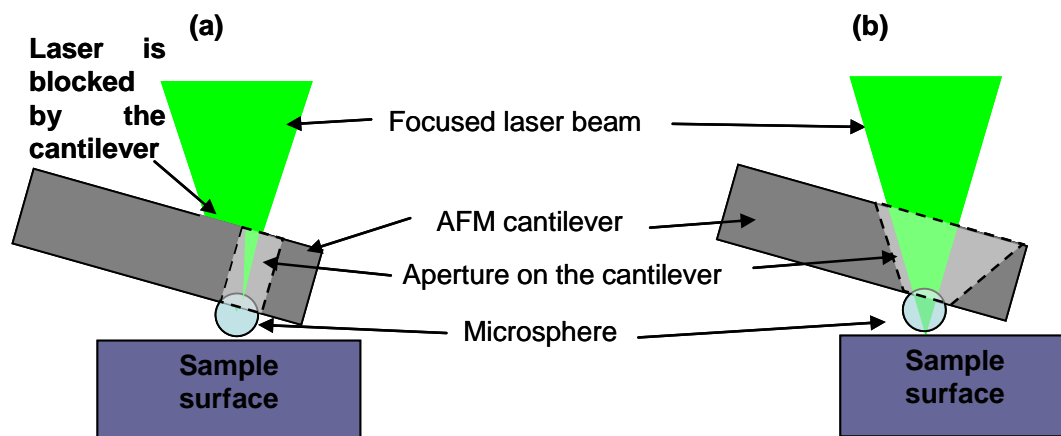


Figure 4.11 Illustration of the problem brought by the aperture on the cantilever.

4.4 Conclusion and future works

The sphere attached cantilever/tip shows great application potential in our preliminary study. It also complements in liquid-free operation and is friendly to all sample surfaces. In the next step of the development, the sphere diameter should be optimized, theoretical and experimental works will be done to test the enhancement for different size of the sphere under different objective lens to further optimize the experiment. For the instrumental part, a feed-back system is setting up to maintain a constant sphere-sample distance to improve the stability of the measurement and minimize the damage to the sample surface and attached sphere.

Chapter 5 Visualization and investigation of Si-C covalent bonding of single carbon nanotube grown on silicon substrate

Chapter 5

Visualization and investigation of Si-C covalent bonding of single carbon nanotube grown on silicon substrate

5.1 Introduction

CNTs have attracted a great amount of interest because of their extraordinary electrical, chemical, thermal and mechanical properties[63, 64, 70-104] that make them promising candidates for nano-electronics and device applications. One of the unique properties of CNTs is that they can be either metallic or semiconducting, depending on their chirality and diameters[209]. CNTs can also be tuned to be either P-type or N-type by introducing structural defects [210, 211]. Nano-PN-junctions and nano-field-effect-transistors are some of the most fascinating applications[75] that make use of these properties. Recently, many groups have predicted that the electrical properties of single CNTs can be tuned by inducing covalent bonds between the CNTs and a Si substrate [212-215]. By selectively forming covalent bonds between the CNTs and the Si substrate, it is possible to build nano-scaled or even single-molecule electronic devices. Fabrication of CNT devices on Si substrates also has the additional advantage of direct integration into well-developed silicon technology.

Several groups have achieved Si-CNT bonding in ceramics with good mechanical properties by annealing Si nano-particles together with CNTs[216]. However, direct observation of Si-C covalent bonding on single CNTs on Si substrate has not been reported, partly because the lack of suitable characterization techniques. It has been

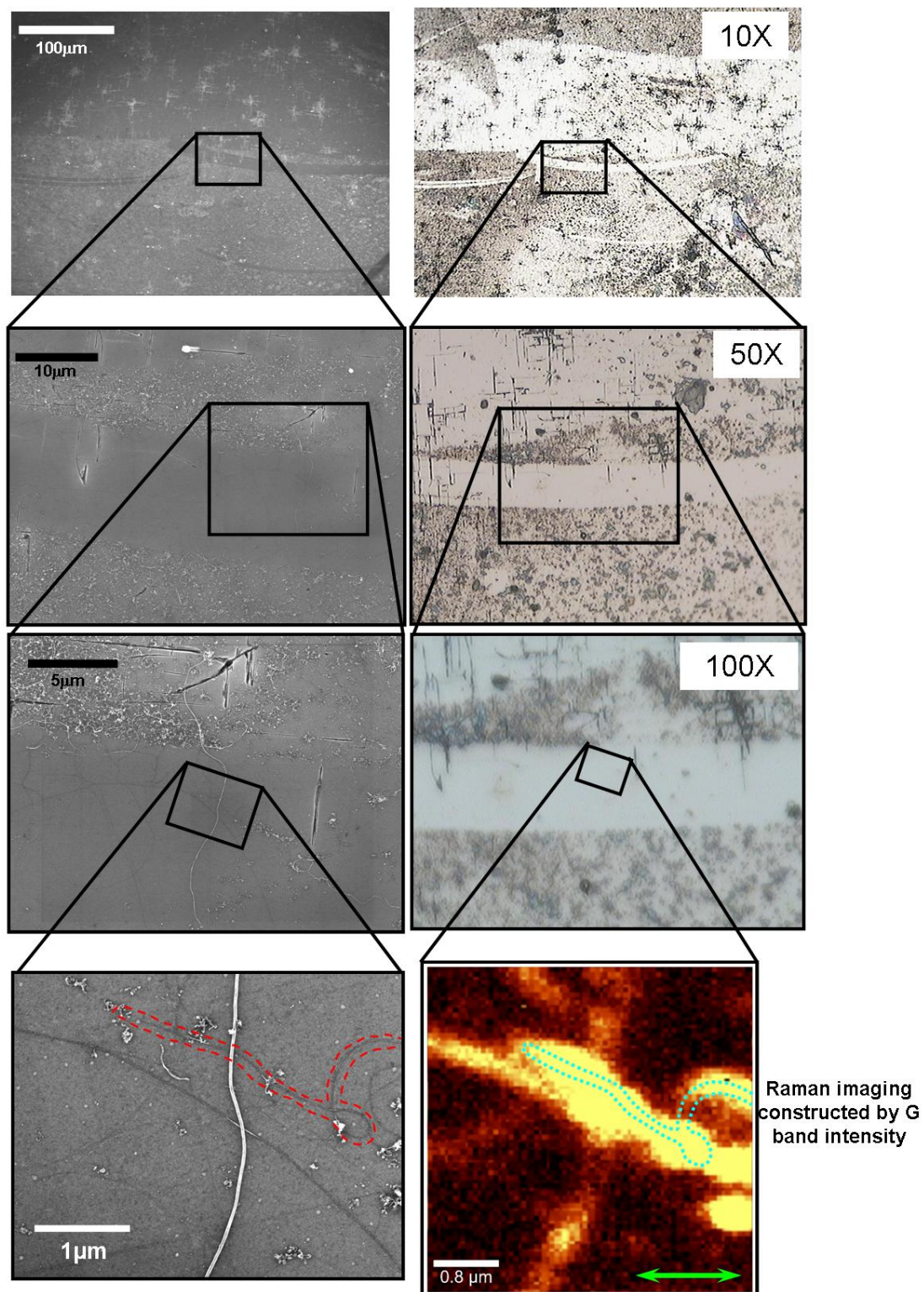
Chapter 5 Visualization and investigation of Si-C covalent bonding of single carbon nanotube grown on silicon substrate

predicted that the Si-CNT interaction results in a large variety of changes in the electronic structures of the CNT. For example, Miwa et al studied single-walled CNTs adsorbed on partially and fully hydrogenated Si (001) surfaces[212, 213, 217]. They showed that by removing a few H atoms along the adsorption sites, the metallic character of the CNTs will be enhanced. However, removing all the H atoms will render the CNTs semiconducting. To realize Si-CNT devices, the first step is to induce Si-CNT covalent bonds on a large scale. Whatever the technique used to characterize the sample, it must be able to identify the CNTs with Si-C bonds. In this chapter, we used Raman imaging that can probe down to the sub-micron scale, to investigate isolated single CNTs and their interaction with the Si substrate. The CNTs were grown on silicon substrate at high temperature in order to achieve Si-CNT bonding, and Raman imaging reveals that some single CNTs were covalently attached to the silicon wafer surface.

5.2 Experimental

The CNTs were grown on Si substrate by thermal CVD. The substrate was cleaned using trichloroethylene, acetone and ethanol in turn by ultrasonic agitation. An ultrathin Fe film, which acted as a catalyst, was deposited in vacuum of 10^{-5} Torr by ion beam sputtering. The substrates were pre-annealed at 850°C in hydrogen in a quartz tube furnace for 90 min. CNTs were then grown at 1000°C for 20 minutes using methane, hydrogen and argon at a gas flow rate of 75, 20, and 100 sccm, respectively. The sample was cooled below 300°C before exposing to air to avoid damage due to rapid cooling.

Chapter 5 Visualization and investigation of Si-C covalent bonding of single carbon nanotube grown on silicon substrate



Chapter 5 Visualization and investigation of Si-C covalent bonding of single carbon nanotube grown on silicon substrate

Figure 5.1 The figures show the procedures of locating area of interests and the correspondence of optical images and SEM images. Left column are SEM image with different magnification. Right column are optical images and Raman image constructed by G band intensity (lowest right figure) with different magnification. Same CNT in the SEM picture and Raman image is emphasized by dotted curves.

The SEM and Raman studies are carried out by the same equipments as described in chapter 3. As the CNTs are not visible under optical microscope, we took SEM images with different magnification on the area of interests, which serve as a map. With the help of the artificial marking (scratches) on the sample surface, we can then use optical microscope to locate and carry out Raman imaging on the exact CNT which was studied by SEM. The locating process is shown in figure 5.1. These processes allow us to locate and perform one-to-one-corresponding Raman spectroscopic study on samples which are normally “invisible” under optical microscope, such as individual SWCNT, quantum dots, nanoparticles, etc.

Chapter 5 Visualization and investigation of Si-C covalent bonding of single carbon nanotube grown on silicon substrate

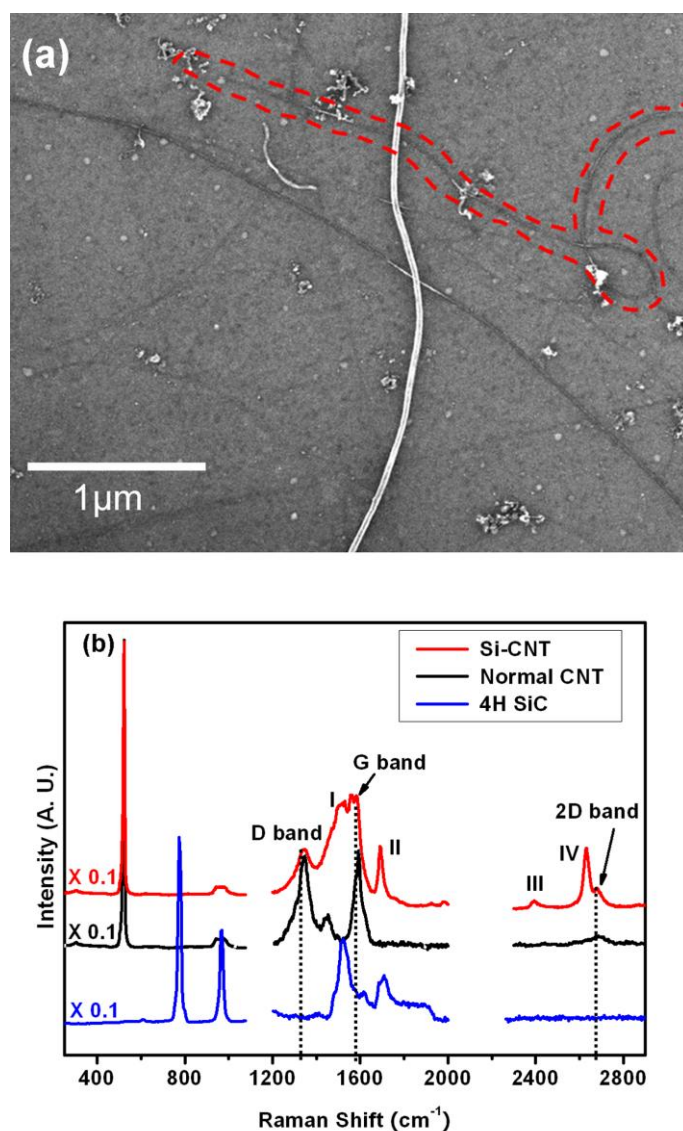


Figure 5.2 (a) SEM image showing an area of interest. Raman bands belonging to Si-C bonds can be detected on the CNT indicated by the dashed curve in red. (b) Comparison of Raman spectra obtained on normal CNTs (black spectrum), on the special CNT (red spectrum) and on bulk crystalline 4H SiC (blue spectrum). The dotted lines represent the CNT peak positions at the D band, G band and 2D band.

Chapter 5 Visualization and investigation of Si-C covalent bonding of single carbon nanotube grown on silicon substrate

5.3 Results and Discussion

Figure 5.2(a) shows the SEM image of the sample. It can be seen that all the CNTs were horizontally grown on the Si substrate in random orientations. The various diameters of CNTs may be due to the different sizes of the Fe catalyst. After analysis of the Raman spectra in the Raman images reveal that the Raman spectra of the CNTs shown in figure 5.2(a) can be separated into two groups: those consisting only normal CNT peaks and those with additional peaks which can be assigned to Si-C bonds (to be discussed in detail later). For simplicity, we call these two types of spectra as CNT spectra and Si-CNT spectra respectively. Figure 5.2(b) shows the typical Raman spectra of these two groups and that of bulk crystalline SiC for comparison. The CNT spectrum only shows the Raman bands of normal CNTs: the D band at 1344 cm^{-1} , the 2D band at 2681 cm^{-1} , and the G band [216]. The G band can be further resolved into the G^- band at 1570 cm^{-1} and G^+ band at 1590 cm^{-1} . For certain CNTs (such as the CNT highlighted by the red dashed curve in figure 5.2(a)), their Raman spectra show extra bands belonging to Si-C bonds at around 1510 cm^{-1} (band I), 1692 cm^{-1} (band II), 2392 cm^{-1} (band III) and 2620 cm^{-1} (band IV). Several regions were tested in this work and we noted that the extra bands (band I to IV) were observable only for certain CNTs, suggesting that Si-C bonds form only for certain CNTs. We term these CNTs with such bonding as Si-CNTs.

We performed Raman imaging in the back-scattering configuration at the same region shown in figure 5.2(a) using a scanning step size of 50 nm and with the incident laser polarized horizontally as indicated by the green arrow in figure 5.3. Raman images

Chapter 5 Visualization and investigation of Si-C covalent bonding of single carbon nanotube grown on silicon substrate

constructed using the intensities of different peaks were shown in figures 5.3. Figure 5.3(a) was generated by the G band (including the G^+ and G^- bands around 1580 cm^{-1})

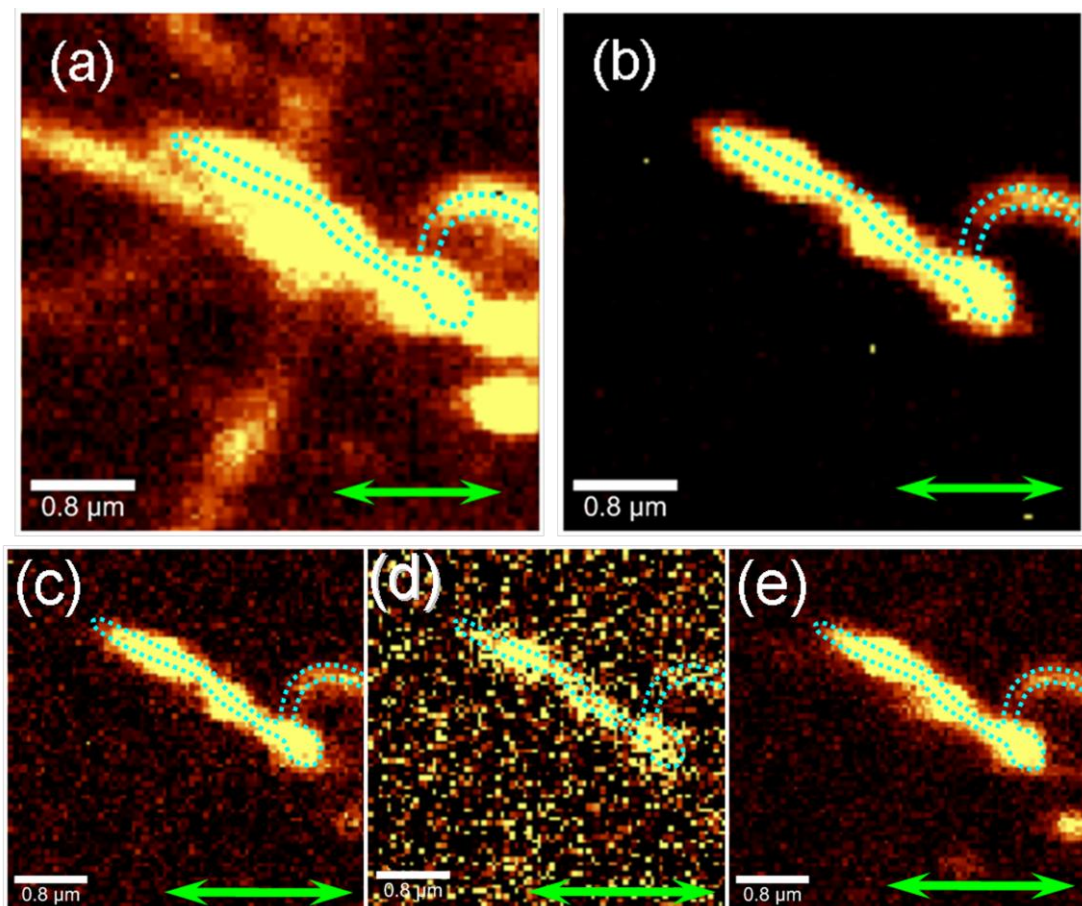


Figure 5.3 Raman images constructed using peak intensity of (a) G band of CNTs, (b) band I of Si-C at 1510 cm^{-1} , (c) band II of Si-C at 1692 cm^{-1} , (d) band III at 2392 cm^{-1} , and (e) band IV at 2620 cm^{-1} . The green arrow indicates the polarization of the incident laser. The blue dotted curves indicate the position and shape of the special CNT.

Chapter 5 *Visualization and investigation of Si-C covalent bonding of single carbon nanotube grown on silicon substrate*

intensity of CNTs. Brighter regions represent the CNTs, whose locations correspond well with those observed under SEM. We also constructed images using the intensity of the extra band (labeled I) and the resulting image is shown in figure 5.3(b). The shape and position of the bright region matches perfectly the CNT emphasized by the dashed curve in the SEM image [figure 5.2(a)]. Images generated using bands II, III and IV, shown in Figures 5.3(c) – 5.3(e) respectively, exhibit nearly identical patterns as that generated using band I, clearly indicating that the three bands are all correlated with the same CNT emphasized in the SEM image.

Before assigning the peaks, we need to first exclude the possibility that Raman bands I to IV are from CNTs. Band I has a similar shape and position as the fano-like lineshape of the G band of metallic CNTs. Oron-Carl et al.[218] compared the G⁻ band of metallic CNTs and semiconducting CNTs and found that for metallic tubes, the fano-like band has a width around 34-54 cm⁻¹, while for the G⁺ band, the width is 20 to 30 cm⁻¹. For our case, the G⁺ band has a width around 30 cm⁻¹, which agrees well with their results. However, Band I has a width of about 130 cm⁻¹, which is much broader than the G⁻ band in their results. Based on this, we can eliminate the possibility that band I is related to the G band of metallic CNTs. Furthermore, as far as we know, the maximum intensity of such fano-like band usually appears around 1540-1550 cm⁻¹[218-220], while band I is found at 1510 cm⁻¹. For band II, we note that the position is similar to that of the band observed in pristine CNTs located around 1740 cm⁻¹. The latter is a combination mode comprising of the first order RBM and the most intense G mode (usually the G⁺ mode) [151]. This peak is normally found together with another band of comparable intensity

Chapter 5 *Visualization and investigation of Si-C covalent bonding of single carbon nanotube grown on silicon substrate*

around 1900 cm^{-1} , which is a combination mode comprising of the second order RBM and the most intense G mode. The spectral distance between these two bands should be equal to the frequency of first order RBM. In our experiments, we did not observe such a band near 1900 cm^{-1} and neither did we observe band II on the “normal” CNTs. Hence, we conclude that band II did not originate from the CNTs, despite the fact that it is located close to the position of the band at 1740 cm^{-1} for pristine CNTs. In Figure 5.2(b) for the spectrum taken at the same position as the Si-CNT, the D band is located at 1350 cm^{-1} while both band IV and the 2D band of CNTs are located in the region between 2600 cm^{-1} and 2800 cm^{-1} . We assigned the bands based on the fact that the frequency of the 2D band should be two times the frequency of the D band (1350 cm^{-1}). Therefore the 2D band should be at 2700 cm^{-1} , as labeled in figure 5.2(b). A weak Raman band located $\sim 1450\text{ cm}^{-1}$ can also be observed, which is attributed to the third-order Raman mode (3TO) of the silicon substrate.

To further confirm that these bands in figure 5.2(b) are indeed related to Si-CNT covalent bonds, we compared our Raman spectra with those of bulk crystalline 4H SiC which have been well studied[221]. The Raman spectra of bulk crystalline 4H SiC are shown as blue curves in figure 5.2(b). The peak positions and relative intensities of SiC Raman bands vary for different polytypes, and generally there are two characteristic bands in the region above 1300 cm^{-1} : a broad band between 1510 cm^{-1} and 1540 cm^{-1} and a narrower band around 1710 cm^{-1} . Both bands correspond to multi-bands resulting from overlapping of different overtone phonon vibrations of SiC[222, 223]. As shown in figure 5.2(b), the shapes and intensities of band I (1510 cm^{-1}) and band II (1692 cm^{-1})

Chapter 5 Visualization and investigation of Si-C covalent bonding of single carbon nanotube grown on silicon substrate

resemble those of the two characteristic bands of SiC. We noticed that bands III and IV are not detected in bulk SiC at the high frequency region. These spectral differences are understandable considering the following: the Si-C covalent bonds in our case are intrinsically of an interfacial/surface mode, for which the Raman selection rules may be broken down. However, the excellent correspondence in the Raman images constructed by bands III and IV with those constructed by band I and II shows that bands III and IV are also from the Si-C bonds in our sample.

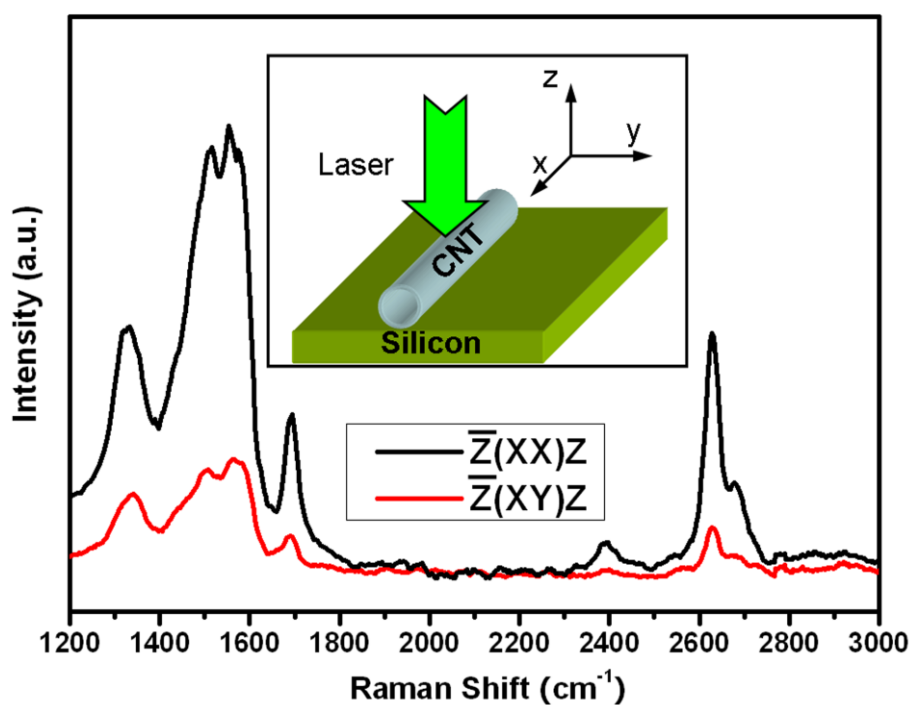


Figure 5.4 Polarized Raman spectra on the special CNT. Inset is the schematic of the configuration of the experiment.

Chapter 5 Visualization and investigation of Si-C covalent bonding of single carbon nanotube grown on silicon substrate

Figure 5.4 shows the polarized Raman spectra from the CNT with Si-C bonds, with the incident laser polarization along the long axis of the CNT and the Raman signal collected parallel and perpendicular to the polarization of the laser. The results show that the Raman spectra are strongly polarization dependent, which indicate that the Si-C bonds are arranged orderly along the long axis of the Si-CNT [224]. It effectively excludes the possibility that the Si-CNT bands we observed are from surface-adsorbed carbon or other surface contamination, which are normally amorphous with bonds randomly arranged.

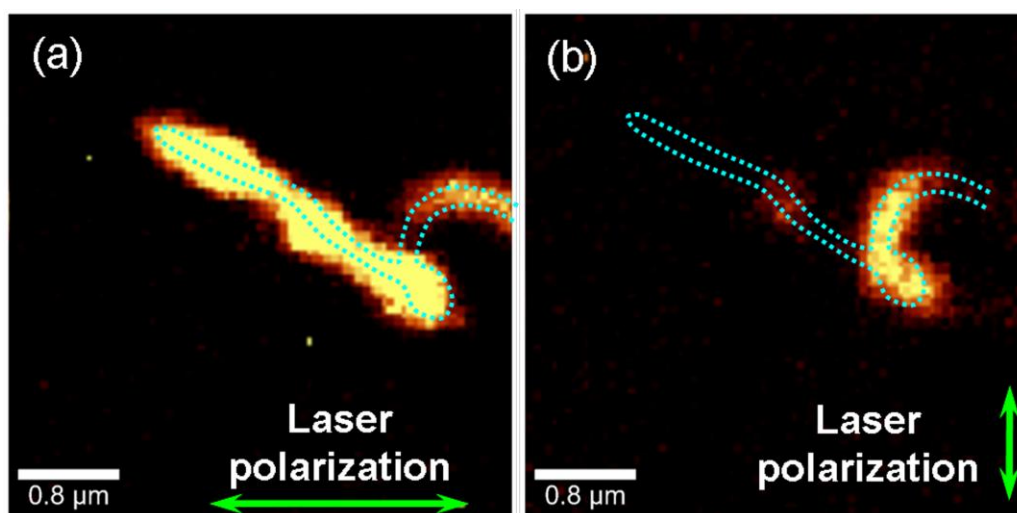


Figure 5.5 Raman imaging with different incident polarization: (a) horizontal and (b) perpendicular. The blue dotted curves indicate the position and shape of the CNTs with Si-C bonds.

Raman imaging with different laser polarizations is also carried out on the area of interest, as shown in figure 5.5. Images are constructed by the peak intensity of band I at

Chapter 5 Visualization and investigation of Si-C covalent bonding of single carbon nanotube grown on silicon substrate

1510 cm^{-1} , one of the second order Raman band of Si-CNT covalent bonding. From the images, it is clear that only the portion of the Si-CNT which has a component parallel to the polarization of the incident laser can be observed. This result can be well explained by the depolarization effect [225], as the distribution of Si-CNT covalent bonds also follow the anisotropic geometry of the CNTs. The same polarization dependence was also observed for the images constructed from intensities of bands II at 1700 cm^{-1} and IV at 2630 cm^{-1} (results not shown).

5.4 Conclusion

In summary, we have grown CNTs on a silicon substrate at high temperature using Fe as the catalyst. Raman spectroscopy and imaging show that Si-C bonds were formed between some CNTs and the Si substrate. Polarized Raman spectroscopy was also carried out, which further verified our conclusion. Systematic investigation of the mechanism of forming such Si-CNT covalent bonds and the vibrational properties of such a system is currently being performed both experimentally and theoretically. We have shown that Raman imaging is a powerful tool for the identification and characterization of individual Si-CNTs bond formation. This is crucial for developing single-CNT nano-scale electronics and logic circuits with tunable electrical transport properties.

Chapter 6

Edge chirality determination of graphene by Raman spectroscopy and imaging

6.1 Introduction

Graphene has attracted great attention not only because it is the ideal material to study the fundamental properties of two-dimensional nanostructures[111], but also for its potential applications in future electronic devices [144]. The exceptionally high crystallization and unique electronic properties make graphene a promising candidate for ultrahigh speed nanoelectronics [145]. Graphene nanoribbons (GNR) have been receiving remarkable attention[226, 227]. It was predicted that GNR with certain edge chirality would open the bandgap [226-228] and show distinct magnetic[228, 229], optical[229] and superconductive[230] properties. All these peculiar properties are strongly dependent on the edge chirality (zigzag or armchair). Conventional methods like transmission electron microscope (TEM), X-ray diffraction (XRD) and STM are either destructive, very time consuming or nearly impossible to locate such small regions of interest[231, 232]. The increasing interests in graphene demand a fast and non-destructive method to determine the state of edges and the crystal orientation.

As a perfect single crystalline structure, the MCG sheet is also expected to have similar cleavage behaviors[233]. After studying hundreds of MCG pieces, we found that the angles between MCG edges have an average value equaling to multiples of 30°. Figure 6.1(a) shows the optical image of a typical MCG sheet and the angles between the edges as an example. Figure 6.1(b) shows the measurement of angles. It can be clearly

Chapter 6 Edge state determination of graphene by Raman spectroscopy

seen that most of the angles are distributed around $n \times 30^\circ$, where n is an integer between 0 and 6. Such a distribution suggests that the carbon atoms along the graphene edges have either zigzag or armchair structures. It can be easily shown that when the angle between two adjacent edges is 30° , 90° or 150° , the two edges have different edge chiralities, i.e. one armchair and the other one zigzag. On the hand, when the angle is 60° or 120° , both edges have the same edge chirality (either zigzag or armchair). Recently,

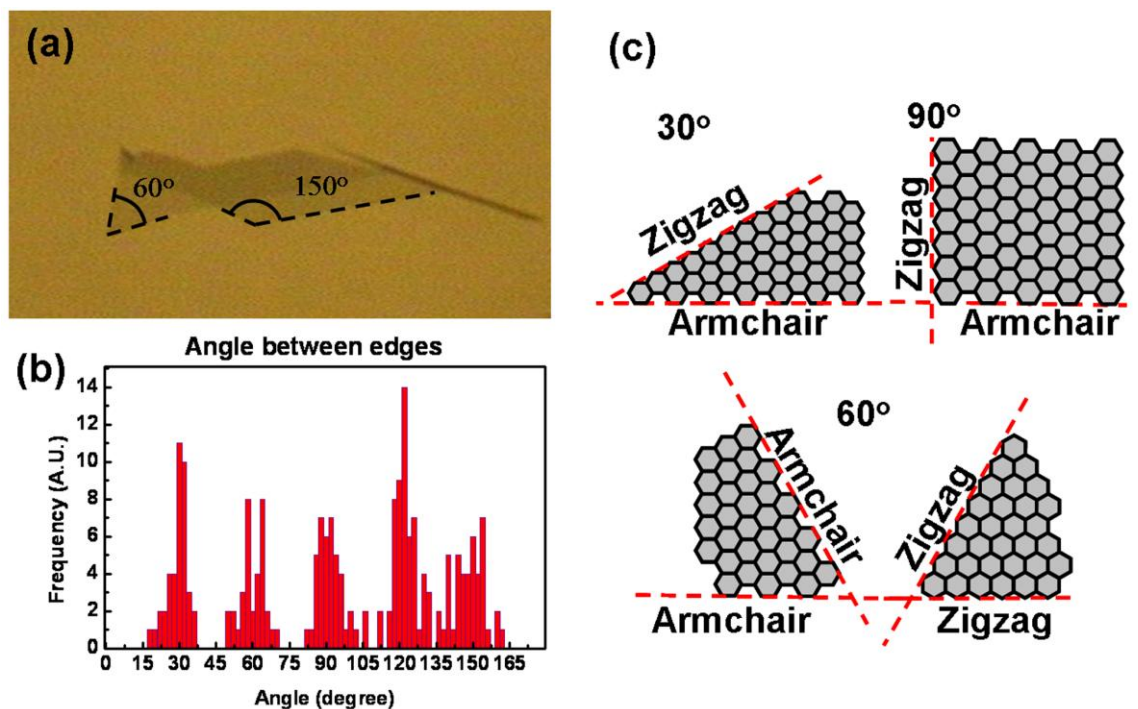


Figure 6.1 (a) Optical image of a typical MCG sheet and the angles between edges. (b) The statistical results of the angle measurements. The standard deviation is 5.4° . (c) Illustration of the relationship between angles and the chiralities of the adjacent edges.

SEM and TEM results have actually shown that the edge of graphene is not ideally smooth[234]. For such edges, both kinds of edge structures should exist. However, the majority of carbon atoms still have the same arrangement as the smooth one. Therefore,

Chapter 6 *Edge state determination of graphene by Raman spectroscopy*

the angle and state of edges should result from a microscopic averaging effect, as the majority of the carbon atoms along the edge are arranged in one kind of edge chirality different from the other kind. As a result, the edge chirality we mentioned in this work is the average from the statistics.

As one of the most commonly used techniques to characterize carbon related materials, Raman spectroscopy plays a very important role in acquiring information on the physical, chemical and even electronic properties of graphene and graphene based devices[154, 235]. Figure 6.2(a) shows the spectral comparison between MCG on SiO₂/Si with different number of layers. The Raman spectra are obtained with an excitation source of 532 nm. In Figure 6.2(a), graphene shows three major Raman bands: The G band ($\sim 1580 \text{ cm}^{-1}$) that originated from the in-plane vibrations of the graphene lattice[149], and a second-order Raman feature named 2D band ($\sim 2700 \text{ cm}^{-1}$) [150-152]. In the presence of defect or on the edge of a graphene sheet, one can observe another Raman band at $\sim 1300 \text{ cm}^{-1}$, which is called D band. A double resonance process is introduced to explain the appearance of the D band and 2D band, which consists of several steps: (i) an electron-hole pair is excited by absorbing an incident photon. (ii) The electron (or hole) is inelastically scattered by another phonon. (iii) The electron (or hole) is then elastic scattered again by a defect (D band) or another phonon with opposite wavevector (2D band). Finally, the excited electron and phonon recombine and emit a photon[153]. Figure 6.2(b) provides a zoom-in view of the 2D band. It can be seen that by increasing the number of layers the 2D band becomes broaden and blue-shifted. Such phenomenon closely related to the band structure differences of graphene with different number of layers, as the 2D band origins from the two phonon double resonance

Chapter 6 Edge state determination of graphene by Raman spectroscopy

process[236-238]. Besides the difference in 2D band for graphene of different thickness, the G band intensity increases almost linearly with the graphene thickness[114]. Therefore, the intensity ratio between the G band and 2D band and the width of 2D band can be used to determine the number of layers of graphene.

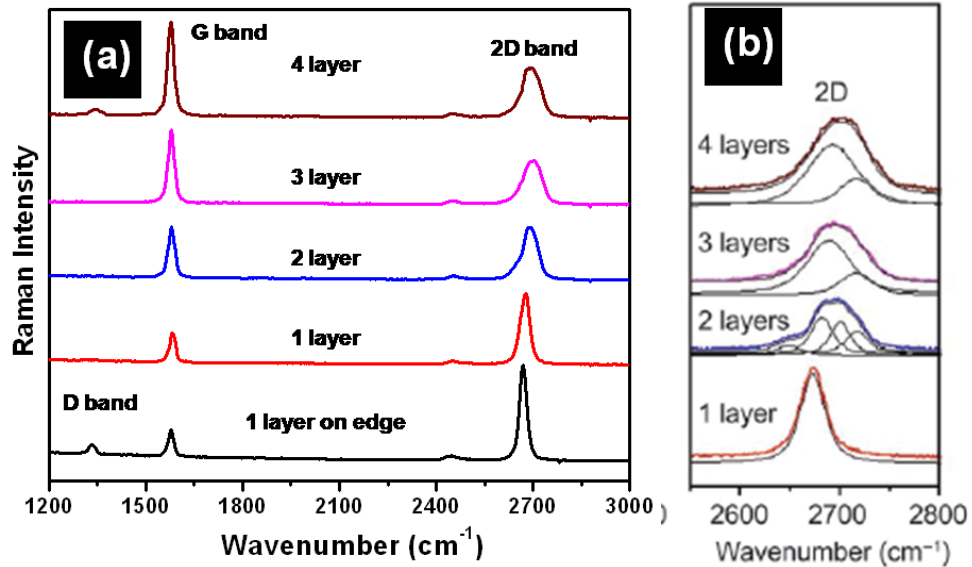


Figure 6.2 (a) Comparison of Raman spectra for different numbers of layers. (b) Zoom-in view of the Raman 2D band. Adapted from Ni et al.

[239].

In this work, we are able to determine the edge chirality, hence the crystallographic orientation of graphene using the difference in intensity of the D band on the different states of edges (stronger in armchair edges and weaker in zigzag edges). This provides an easy and nondestructive method to identify the edge chirality of graphene, which would help to speed up the practical applications of graphene nanoelectronic devices, such as GNR.

Chapter 6 Edge state determination of graphene by Raman spectroscopy

6.2 Experimental

The MCG sheets are prepared using the common micromechanical cleavage method on a 300 nm SiO₂ / Si substrate which provides a good optical contrast[114]. The Raman study was carried out using a WITec CRM200 confocal microscopy Raman system with a 100X objective lens (NA=0.95). The excitation light is 532 nm laser. Raman images were generated by scanning the sample with step size of 100 nm with a spatial resolution ~500 nm.

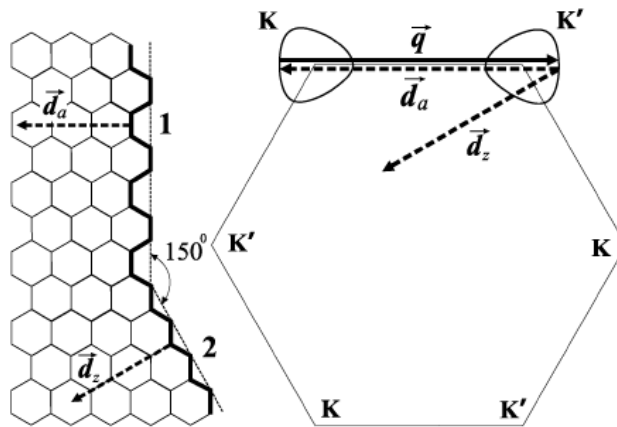


Figure 6.3 (a) Schematic illustration of the atomic structure of the armchair and zigzag edges and (b) first Brillouin zone of 2-D graphite, showing the double resonance mechanism for an armchair graphite edge. Adapted from Cancado et al.[240]

6.3 Results and Discussions

A piece of single layer graphene (SLG) is used as the sample. The number of layer has been determined by Raman spectroscopy as well as the contrast method[239]. There are two edges. The angle (θ_1) between those two edges (1 and 2) is 30°. Based on previous discussions, edge 1 and 2 should have different edge chiralities. The main

Chapter 6 *Edge state determination of graphene by Raman spectroscopy*

question here would be whether it is possible to determine the chirality of each edge. Here, Raman spectroscopy proves to be critically useful.

At the edge of the graphene, the double resonance D bands are closely related to the edge chiralities of which is either zigzag or armchair[240]. The edge chirality induced D band of highly ordered pyrolytic graphite (HOPG) have been studied by Cancado et al. before[149, 240]. They found that the D band obtained from the armchair edge of HOPG has much stronger intensity than that from the zigzag edge which could be explained by the theoretical analysis. Their theoretical explanation was based on the model of SLG. Figure 6.3 shows the edge chirality of the SLG together with its first Brillouin zone. Edge 1 and edge 2 in this figure are armchair edge and zigzag edge, respectively. The wavevectors of the edge-induced defect are illustrated by the dotted arrows. The double resonance process for D band is: firstly, the generation of electron hole pair near K point by absorbing a photon; secondly a phonon inelastically scatters the electron to the K' point; thirdly, the electron is elastically scattered back near K point by the defect; finally is the recombination of the electron-hole pair. From figure 6.3(b), we can see that the wavevector of zigzag edge-induced defect cannot connect any point of the equi-energy contour of the K and K' point, which means electrons are difficult to be scattered back to the K point by the zigzag edge, therefore, the weak or vanished D band is observed. And for the armchair edge, it can fulfill the requirement of scattering back of electron to the K point, hence the strong D band is obtained. This idea present a simple and efficient way to distinguish the edge chirality of the HOPG and in this work this method is extended to the study of the edge chirality of SLG.

Chapter 6 Edge state determination of graphene by Raman spectroscopy

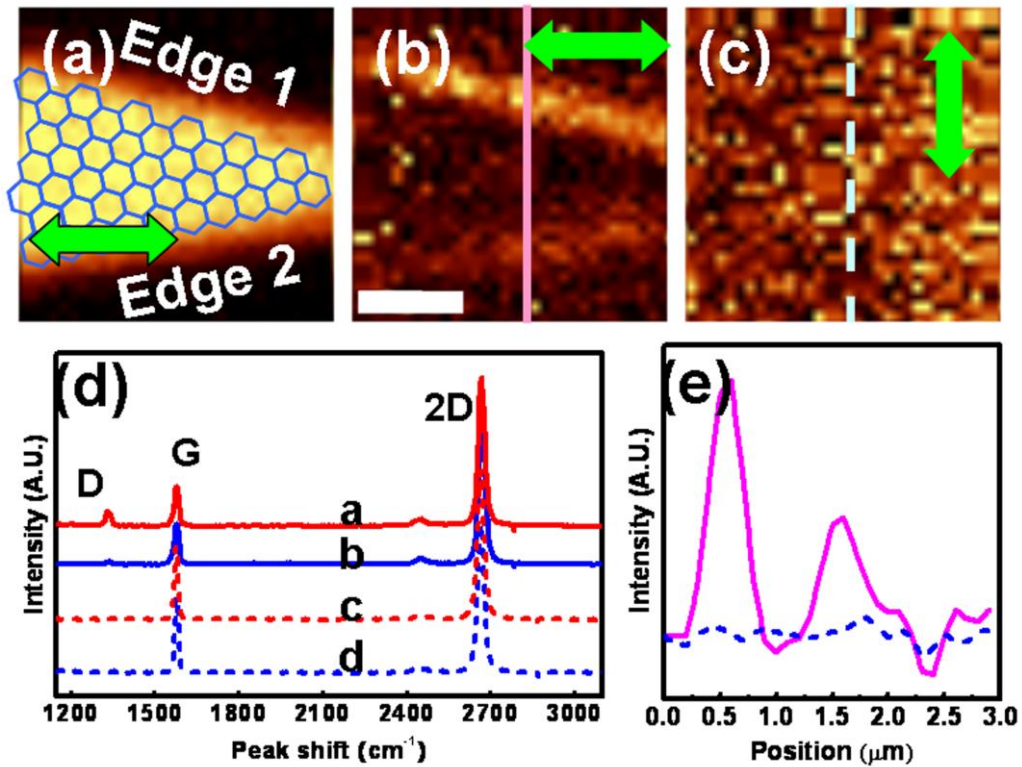


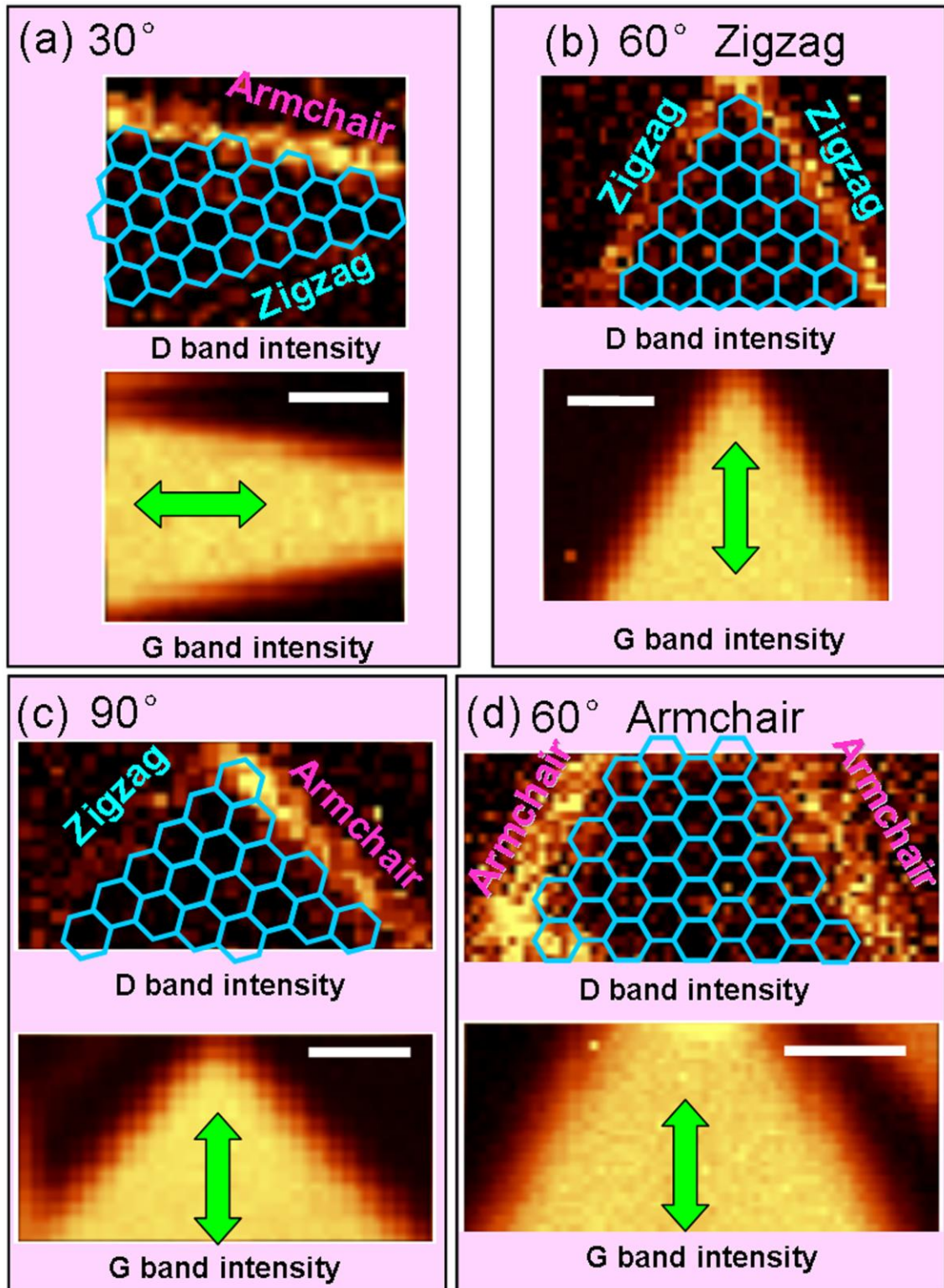
Figure 6.4 (a) Raman image constructed by the intensity of G band with the expected arrangement in blue. Figure (b) and (c) are images constructed by the D band intensity with horizontal and vertical polarization, respectively. All images share the same scale bar as indicated in figure (b) which is $2\ \mu\text{m}$. (d) Raman spectra taken from edge 1 (spectrum a), and edge 2 (spectrum b), with horizontal laser polarization. Spectra c and d were also collected from edges 1 and 2 respectively, with vertical laser polarization. (e) The solid and dotted lines represent the D band intensity profile (solid/dash) plotted along the solid line on figure (b) and the dashed line on Figure (c), respectively.

Chapter 6 *Edge state determination of graphene by Raman spectroscopy*

Raman images edge 1 and 2 are shown in figure 6.4(a)-(c). The bright part in Figure 2(a) corresponds to the appearance of the G band. The G band intensity is distributed uniformly over the whole graphene sheet, indicating the good quality of the sample. Figure 6.4(b) and (c) show the D band intensity of graphene with laser polarization in the horizontal and vertical directions respectively. From these images, we can see that the D band only appears at the edges and shows very strong polarization dependence. We put the sample in this orientation to ensure that both edges (1 and 2) make the same angle with the laser polarization, $\pm 15^\circ$ to the horizontal polarization and $\pm 75^\circ$ to the vertical polarization. Therefore, the stronger D band intensity at edge 1 compared to that at edge 2 is not due to the polarization effect, but related to the carbon atom arrangement at the edge, i.e. the edge chirality[240]. The spectra collected from different spots in both polarizations are shown in figure 6.4(d). All of the spectra are recorded under the same conditions. Spectra a and b are recorded at edge 1 and 2 respectively, with horizontal laser polarization, which is almost parallel to the two edges. The D band intensity of edge 1 is 1.7 times of that of edge 2. Since this is not due to the polarization effect, we can now identify edge 1 as armchair edge while edge 2 as zigzag edge. Do note that the armchair or zigzag arrangement mentioned here for edges 1 and 2 should be a result of the majority of carbon atoms along the edge being arranged in one kind of structure (either armchair or zigzag). This can be demonstrated in spectrum b of figure 6.4(d), where a weak D band can be observed. This suggests that, in edge 2, there is still a small portion of carbon atoms in armchair arrangement. On the other hand, spectra c and d in figure 6.4(e) are recorded at edges 1 and 2, respectively, with a vertical laser polarization. Both spectra hardly show any D band because of the polarization effect. Raman images of SLG edges with different angles are compared in figure 6.5. In the case of 30° and 90° , edges show different D band contrast as they have different edge chirality. On the other

Chapter 6 *Edge state determination of graphene by Raman spectroscopy*

hand, in the case of 60° , a similar D band contrast is observed as the two edges have same edge chirality.



Chapter 6 *Edge state determination of graphene by Raman spectroscopy*

Figure 6.5 Raman imaging results from edges with angles (a) 30° , (b) 60° (zigzag), (c) 90° and (d) 60° (armchair). The images constructed by the G band intensity show the positions and shapes of the SLG sheets. The laser polarization is indicated by the green arrows. The superimposed frameworks are guides for the eye indicating the edge chirality. Note that the edge chirality of (b) and (d) were determined by the other pair of edges (not shown) with $30^\circ / 90^\circ$ on the same piece of SLG. The scale bar is $1\ \mu\text{m}$.

Chapter 6 *Edge state determination of graphene by Raman spectroscopy*

Table 2. Statistic results of intensity of D band along different edges.

Angle (degree)	# of pixels used for calculation	Average D band intensity (A. U.)	Standard deviation (A. U.)	Difference	Edge chirality
30	63	20.2	6.8	1.66	Zigzag
	60	33.5	9.9		Armchair
30	54	6.6	6.1	3.12	Zigzag
	75	20.6	6.3		Armchair
90	42	8.1	4.4	3.40	Zigzag
	62	27.5	7.9		Armchair
90	33	24.0	5.9	1.95	Zigzag
	34	46.8	7.4		Armchair
60	107	13.9	6.3	1.01	Same state
	113	14.1	10.1		
60	66	11.3	6.3	1.07	Same state
	66	12.1	6.4		
120	63	20.2	6.8	1.09	Same state
	63	22.0	8.3		
120	33	10.0	5.3	1.22	Same state
	30	12.2	4.7		
120	37	33.9	8.2	1.10	Same state
	33	37.4	9.4		

To rule out the possibility that the results of Raman imaging are caused by a difference in focusing or edge nonuniformity, we carried out a statistical analysis of the Raman intensities at each edge. For the SLG discussed in figure 6.4, it has three edges with an angle of 30° between edge 1 and 2, and 120° between edge 2 and 3. To compare the three edges under the same conditions, Raman imaging is carried out on each individual edge, with the laser polarization parallel to that edge (Raman images are not shown). The D band obtained at different spots of the edge was then fitted using a Lorentzian function and the intensity image was plotted. We manually chose the data points along the edges with similar area (~ 300 nm by $2\ \mu\text{m}$) and calculated the average D

Chapter 6 *Edge state determination of graphene by Raman spectroscopy*

band intensity generated from the edges. The average D band intensity from edge 1 (33.5) is obviously stronger than those from edges 2 (20.2) and 3 (22.0), which reveals that edge 1 is armchair and edges 2 and 3 are zigzag. This is consistent with the discussion in Figure 6.4 about the state of edge 1 and 2. Similar results were also obtained for other MCG sheets. We have in total measured nine pairs of edges with different angles (listed in table 2), and our Raman results agree well with expectation. For angles of 30° and 90° , two adjacent edges show different D band intensities, indicating they have different atomic arrangements at the edges. While for angles of 60° and 120° , two adjacent edges show similar D band intensities, showing that they have the same arrangement. The intensity ratio for the same edge chirality is around 1.0, while the difference for different edge chiralities is greater than 1.6, which suggests that Raman spectroscopy is a practical and reliable method for determination of the graphene edge structure.

6.4 Conclusion

By knowing the edge arrangement, we can actually know the crystallographic orientation of the whole graphene sheet. This is significant in the process of making graphene nano-constriction using lithography techniques[241]. To conclude, we found that although the edges of MCG are not ideally smooth, they are on average predominantly either zigzag or armchair in nature. The defect-induced D band at the edges was found to be strongly polarization dependent, which is similar to that of graphite edges. This can be used to determine the crystallographic orientation of the MCG, which is important for the study of graphene and graphene-based devices.

Chapter 7

Conclusion and future work

This thesis contains two parts. Firstly, the study of advanced Raman spectroscopy/imaging, SERS and TERS study was carried out on the individual silver NWs, and the development of the cantilever held dielectric microsphere-enhanced Raman spectroscopy/imaging is also included. Secondly, Raman study of carbon related materials such as Si-CNT and graphene are carried out.

7.1 Advanced Raman spectroscopy/imaging

1. SERS at the end of individual single-crystalline Ag NWs have been observed with incident light polarized along the NW axis. The enhancement is attributed to the LSP confined at the end of the NW, which is also demonstrated by FEM simulation. The enhancement factor of the end of the NW is shown to be much higher than the SERS at the body of the NW. As the Ag NWs can be easily located by optical microscope and EM field is confined strongly at almost every tip of NWs, Ag NWs can be a perfect candidate to study the enhancement mechanism of the SERS effect.
2. Using AC-DEP, we present a simple but highly reliable method to apply such NWs as TERS probes. TERS study with such NW tips was also carried out. The results are very promising and show that, by combining the mature metal NW fabrication techniques and the TERS technique, a highly repeatable and much simplified near-field Raman

spectroscopic technique can be expected.

3. Several experimental configurations for near-field Raman imaging using a dielectric microsphere have been tested. After analyzing the results and limitations of the different configurations, an improved setup of using a mechanically held microsphere was introduced. This setup could provide Raman imaging with a much higher spatial resolution and higher S/N ratio as compared to normal confocal Raman imaging and it suggests a great potential in the practical applications of such a method.

7.2 Raman study on carbon related nanomaterials

1. We have grown CNTs on a silicon substrate at high temperature using Fe as the catalyst. Raman spectroscopy and imaging show that Si-C bonds were formed between some CNTs and the Si substrate. Polarized Raman spectroscopy was also carried out, which further verified our conclusion. We have shown that Raman imaging is a powerful tool for the identification and characterization of individual Si-CNTs bond formation. This is crucial for developing single-CNT nano-scale electronics and logic circuits with tunable electrical transport properties.

2. We found that although the edges of MCG are not ideally smooth, they are on average predominantly either zigzag or armchair in nature. The defect-induced D band at the edges was found to be strongly polarization dependent, which is similar to that of graphite edges. This can be used to determine the crystallographic orientation of the MCG, which is important for the study of graphene and graphene-based devices.

7.3 Future work

In the part of advanced Raman spectroscopy/imaging, surface-enhanced Raman spectroscopy study on individual noble metal (Au, Ag, Pt, etc.) NWs and nanostructures will be carried out. At the same time, we will study the SERS effect on metal NWs with different length and diameters. The above works will help us further understand the physics behind the SERS effect especially the EM enhance mechanism. For the TERS part, the imaging study will be carried out to find out the spatial resolution. Metal NWs with smaller diameter (e.g. less than 30 nm) will be employed as the TERS tip to achieve a better spatial resolution.

On the other hand, dielectric microspheres with different diameters and materials will be attached to the cantilever/tip. And as mentioned before, Raman imaging using sphere attached cantilever will be carried out with higher NA objective lens, as the NA increasing, enhancement of spatial resolution is also expected to be improved. Since the sphere is held by cantilever, the relative position of the sphere and the incident laser is no longer uncontrollable as in the case of using optical tweezers. Study of focusing depth should be repeated again with cantilever controlled sphere. From our result, for higher NA objective lens, microspheres with diameters less than 3 μm show better enhancement with high S/N ratio. To test the spatial resolution of such sphere with small diameter microsphere, the aperture of the AFM cantilever need to be further modified as mentioned in chapter 4. Besides the Raman study, sub-diffraction-limited lithography by optical trapped microsphere has been reported recently. As the sphere attached cantilever has many advantages over the optical trapping methods, we are going to extend the

application of our technique to lithography and related topics.

Although many efforts have been made on Raman spectroscopy study of carbon related nanomaterials, especially CNTs and graphene, very little work has been carried out with the near-field techniques. As one of our final aims, we will employ the developed advanced Raman spectroscopy/imaging on the characterization of CNTs, graphene and other carbon nano-materials. The ultra-high spatial resolution and great sensitivity will surely bring us more information about the physical, chemical properties of such materials in a nanometer-scale. For example: in graphene, nanoscale morphology can cause local strain, such local strain will modify the band structure and further effect the electronic properties, a high-resolution Raman spectroscopy/imaging study could be of great importance for the future application of graphene devices. The advanced Raman technique can also be employed to study the bonding properties of Si-CNT, allowing us to obtain structural and even electronic information in ~ 10 nm scale.

References

References

1. Raman, C.V. and Krishnan, K.S., *A new type of secondary radiation*. Nature, **121**, 501-502 (1928).
2. Ferraro, J.R., Nakamoto, K., and Brown, C.W., *Introductory Raman Spectroscopy*. 1994, San Diego, CA: Academic Press, Inc.
3. Svanberg, S., Ecker, G., Lambropoulos, P., Sobelman, I.I., and Walther, H.-O., *Atomic and Molecular Spectroscopy*. Advanced Texts in Physics 2004: Springer.
4. Slater, J.C. and Frank, N.H., *Introduction to theoretical physics*. 1933, New York: McGraw-Hill Company, inc.
5. Smith, W.E., *Practical understanding and use of surface enhanced Raman scattering/surface enhanced resonance Raman scattering in chemical and biological analysis*. Chemical Society Reviews, **37**, 955-964 (2008).
6. Vlckova, B., Moskovits, M., Pavel, I., Siskova, K., Sladkova, M., and Slouf, M., *Single-molecule surface-enhanced Raman spectroscopy from a molecularly-bridged silver nanoparticle dimer*. Chemical Physics Letters, **455**, 131-134 (2008).
7. Qian, X.M. and Nie, S.M., *Single-molecule and single-nanoparticle SERS: from fundamental mechanisms to biomedical applications*. Chemical Society Reviews, **37**, 912-920 (2008).
8. Pieczonka, N.P.W. and Aroca, R.F., *Single molecule analysis by surfaced-enhanced Raman scattering*. Chemical Society Reviews, **37**, 946-954 (2008).
9. Kneipp, J., Kneipp, H., and Kneipp, K., *SERS - a single-molecule and nanoscale tool for bioanalytics*. Chemical Society Reviews, **37**, 1052-1060 (2008).
10. Fleischm.M, Hendra, P.J., and McQuilla.Aj, *Raman-Spectra of Pyridine Adsorbed at a Silver Electrode*. Chemical Physics Letters, **26**, 163-166 (1974).
11. Jeanmaire, D.L. and Vanduyne, R.P., *Surface Raman Spectroelectrochemistry .1. Heterocyclic, Aromatic, and Aliphatic-Amines Adsorbed on Anodized Silver Electrode*. Journal of Electroanalytical Chemistry, **84**, 1-20 (1977).
12. Albrecht, M.G. and Creighton, J.A., *Anomalously Intense Raman-Spectra of Pyridine at a Silver Electrode*. Journal of the American Chemical Society, **99**, 5215-5217 (1977).
13. Kneipp, H. and Moskovits, M., *Surface-enhanced raman scattering: physics and applications*. 2006: Springer.
14. Campion, A. and Kambhampati, P., *Surface-enhanced Raman scattering*. Chemical Society Reviews, **27**, 241-250 (1998).
15. Otto, A., Mrozek, I., Grabhorn, H., and Akemann, W., *Surface-Enhanced Raman-Scattering*. Journal of Physics-Condensed Matter, **4**, 1143-1212 (1992).
16. Lombardi, J.R., Birke, R.L., Lu, T.H., and Xu, J., *Charge-Transfer Theory of Surface Enhanced Raman-Spectroscopy - Herzberg-Teller Contributions*. Journal of Chemical Physics, **84**, 4174-4180 (1986).
17. Kambhampati, P., Child, C.M., Foster, M.C., and Campion, A., *On the chemical mechanism of surface enhanced Raman scattering: Experiment and theory*. Journal of Chemical Physics, **108**, 5013-5026 (1998).

References

18. Moskovits, M., *Surface-Enhanced Spectroscopy*. Reviews of Modern Physics, **57**, 783-826 (1985).
19. Johnson, P.B. and Christy, R.W., *Optical Constants of the Noble Metals*. Physical Review B, **6**, 4370 (1972).
20. Wang, D.S., Chew, H., and Kerker, M., *Enhanced Raman-Scattering at the Surface (Sers) of a Spherical-Particle*. Applied Optics, **19**, 2256-2257 (1980).
21. Hu, B., Xu, W.Q., Wang, K.X., Xie, Y.T., and Zhao, B., *Discussion on the Electromagnetic Theory of SERS According to Dielectric Function* Acta Scientiarum Naturalium Universitatis Jilinensis, 57-61 (2001).
22. Webster, S., Smith, D.A., and Batchelder, D.N., *Raman microscopy using a scanning near-field optical probe*. Vibrational Spectroscopy, **18**, 51-59 (1998).
23. Liao, P.F. and Wokaun, A., *Lightning Rod Effect in Surface Enhanced Raman-Scattering*. Journal of Chemical Physics, **76**, 751-752 (1982).
24. Grand, J., de la Chapelle, M.L., Bijeon, J.L., Adam, P.M., Vial, A., and Royer, P., *Role of localized surface plasmons in surface-enhanced Raman scattering of shape-controlled metallic particles in regular arrays*. Physical Review B, **72**, 033407 (2005).
25. Le, F., Brandl, D.W., Urzhumov, Y.A., Wang, H., Kundu, J., Halas, N.J., Aizpurua, J., and Nordlander, P., *Metallic nanoparticle arrays: A common substrate for both surface-enhanced Raman scattering and surface-enhanced infrared absorption*. Acs Nano, **2**, 707-718 (2008).
26. Porto, J.A., Johansson, P., Apell, S.P., and Lopez-Rios, T., *Resonance shift effects in apertureless scanning near-field optical microscopy*. Physical Review B, **67**, 085409 (2003).
27. Demming, A.L., Festy, F., and Richards, D., *Plasmon resonances on metal tips: Understanding tip-enhanced Raman scattering*. Journal of Chemical Physics, **122**, 184716 (2005).
28. Yeo, B.S., Zhang, W.H., Vannier, C., and Zenobi, R., *Enhancement of Raman signals with silver-coated tips*. Applied Spectroscopy, **60**, 1142-1147 (2006).
29. Gramotnev, D.K., *Adiabatic nanofocusing of plasmons by sharp metallic grooves: Geometrical optics approach*. Journal of Applied Physics, **98**, 104302 (2005).
30. Zhang, W.H., Cui, X.D., Yeo, B.S., Schmid, T., Hafner, C., and Zenobi, R., *Nanoscale roughness on metal surfaces can increase tip-enhanced Raman scattering by an order of magnitude*. Nano Letters, **7**, 1401-1405 (2007).
31. Verma, P., Yamada, K., Watanabe, H., Inouye, Y., and Kawata, S., *Near-field Raman scattering investigation of tip effects on C-60 molecules*. Physical Review B, **73**, 045416 (2006).
32. Domke, K.F., Zhang, D., and Pettinger, B., *Tip-enhanced Raman spectra of picomole quantities of DNA nucleobases at Au(111)*. Journal of the American Chemical Society, **129**, 6708 (2007).
33. Hayazawa, N., Inouye, Y., Sekkat, Z., and Kawata, S., *Near-field Raman scattering enhanced by a metallized tip*. Chemical Physics Letters, **335**, 369-374 (2001).
34. Ren, B., Picardi, G., Pettinger, B., Schuster, R., and Ertl, G., *Tip-enhanced Raman spectroscopy of benzenethiol adsorbed on Au and Pt single-crystal surfaces*. Angewandte Chemie-International Edition, **44**, 139-142 (2005).
35. Hartschuh, A., *Tip-Enhanced Near-Field Optical Microscopy*. Angewandte Chemie-International Edition, **47**, 8178-8191 (2008).
36. Bouhelier, A., Beversluis, M.R., and Novotny, L., *Near-field scattering of longitudinal fields*. Applied Physics Letters, **82**, 4596-4598 (2003).

References

37. Oron, R., Blit, S., Davidson, N., Friesem, A.A., Bomzon, Z., and Hasman, E., *The formation of laser beams with pure azimuthal or radial polarization*. Applied Physics Letters, **77**, 3322-3324 (2000).
38. Neacsu, C.C., Dreyer, J., Behr, N., and Raschke, M.B., *Scanning-probe Raman spectroscopy with single-molecule sensitivity*. Physical Review B, **73**, 4 (2006).
39. Zhang, W.H., Yeo, B.S., Schmid, T., and Zenobi, R., *Single molecule tip-enhanced Raman spectroscopy with silver tips*. Journal of Physical Chemistry C, **111**, 1733-1738 (2007).
40. Domke, K.F., Zhang, D., and Pettinger, B., *Enhanced Raman spectroscopy: Single molecules or carbon?* Journal of Physical Chemistry C, **111**, 8611-8616 (2007).
41. Domke, K.F., Zhang, D., and Pettinger, B., *Toward Raman fingerprints of single dye molecules at atomically smooth Au(111)*. Journal of the American Chemical Society, **128**, 14721-14727 (2006).
42. Neacsu, C.C., Dreyer, J., Behr, N., and Raschke, M.B., *Reply to "Comment on 'Scanning-probe Raman spectroscopy with single-molecule sensitivity' "*. Physical Review B, **75**, 236402 (2007).
43. Steidtner, J. and Pettinger, B., *Tip-enhanced Raman spectroscopy and microscopy on single dye molecules with 15 nm resolution*. Physical Review Letters, **100**, 236101 (2008).
44. Bailo, E. and Deckert, V., *Tip-enhanced Raman spectroscopy of single RNA strands: Towards a novel direct-sequencing method*. Angewandte Chemie-International Edition, **47**, 1658-1661 (2008).
45. Anderson, M.S. and Gaimari, S.D., *Raman-atomic force microscopy of the ommatidial surfaces of Dipteran compound eyes*. Journal of Structural Biology, **142**, 364-368 (2003).
46. Watanabe, H., Ishida, Y., Hayazawa, N., Inouye, Y., and Kawata, S., *Tip-enhanced near-field Raman analysis of tip-pressurized adenine molecule*. Physical Review B, **69**, 155418 (2004).
47. Neugebauer, U., Rosch, P., Schmitt, M., Popp, J., Julien, C., Rasmussen, A., Budich, C., and Deckert, V., *On the way to nanometer-sized information of the bacterial surface by tip-enhanced Raman spectroscopy*. ChemPhysChem, **7**, 1428-1430 (2006).
48. Saito, Y., Motohashi, M., Hayazawa, N., Iyoki, M., and Kawata, S., *Nanoscale characterization of strained silicon by tip-enhanced Raman spectroscopy in reflection mode*. Applied Physics Letters, **88**, 143109 (2006).
49. Saito, Y., Motohashi, M., Hayazawa, N., and Kawata, S., *Stress imaging of semiconductor surface by tip-enhanced Raman spectroscopy*. Journal of Microscopy-Oxford, **229**, 217-222 (2008).
50. Richards, D., Milner, R.G., Huang, F., and Festy, F., *Tip-enhanced Raman microscopy: practicalities and limitations*. Journal of Raman Spectroscopy, **34**, 663-667 (2003).
51. Haynes, C.L. and Van Duyne, R.P., *Nanosphere lithography: A versatile nanofabrication tool for studies of size-dependent nanoparticle optics*. Journal of Physical Chemistry B, **105**, 5599-5611 (2001).
52. Wang, M.D., Yin, H., Landick, R., Gelles, J., and Block, S.M., *Stretching DNA with optical tweezers*. Biophysical Journal, **72**, 1335-1346 (1997).
53. Gorodetsky, M.L., Savchenkov, A.A., and Ilchenko, V.S., *Ultimate Q of optical microsphere resonators*. Optics Letters, **21**, 453-455 (1996).
54. Sandoghdar, V., Treussart, F., Hare, J., LefevreSeguin, V., Raimond, J.M., and Haroche, S., *Very low threshold whispering-gallery-mode microsphere laser*. Physical Review A, **54**, R1777-R1780 (1996).

References

55. Cai, M., Painter, O., Vahala, K.J., and Sercel, P.C., *Fiber-coupled microsphere laser*. Optics Letters, **25**, 1430-1432 (2000).
56. Li, X., Chen, Z., Taflove, A., and Backman, V., *Optical analysis of nanoparticles via enhanced backscattering facilitated by 3-D photonic nanojets*. Opt. Express, **13**, 526-533 (2005).
57. Minoru, S., Tutomu, K., and Kazuhiro, H., *Micro-objective manipulated with optical tweezers*. Applied Physics Letters, **70**, 785-787 (1997).
58. Leclerc, S., Takakura, Y., and Meyrueis, P., *Properties of a three-dimensional photonic jet*. Opt. Lett., **30**, 2641-2643 (2005).
59. Ferrand, P., Wenger, J., Devilez, A., Pianta, M., Stout, B., Bonod, N., Popov, E., and Rigneault, H., *Direct imaging of photonic nanojets*. Optic Express, **16**, 6930-6940 (2008).
60. Alexander, H., Kevin, H., Alan, V.S., Xu, L., Allen, T., and Vadim, B., *Experimental confirmation of backscattering enhancement induced by a photonic jet*. Applied Physics Letters, **89**, 221118 (2006).
61. Soon-Cheol, K., Alan, V.S., Alexander, H., Allen, T., and Vadim, B., *Robust detection of deeply subwavelength pits in simulated optical data-storage disks using photonic jets*. Applied Physics Letters, **92**, 211102 (2008).
62. McLeod, E. and Arnold, C.B., *Subwavelength direct-write nanopatterning using optically trapped microspheres*. Nature Nanotechnology, **3**, 413-417 (2008).
63. Iijima, S., *Helical Microtubules of Graphitic Carbon*. Nature, **354**, 56-58 (1991).
64. Iijima, S. and Ichihashi, T., *Single-Shell Carbon Nanotubes of 1-nm Diameter*. Nature, **363**, 603-605 (1993).
65. Bethune, D.S., Kiang, C.H., Devries, M.S., Gorman, G., Savoy, R., Vazquez, J., and Beyers, R., *Cobalt-Catalyzed Growth of Carbon Nanotubes with Single-Atomic-Layerwalls*. Nature, **363**, 605-607 (1993).
66. Huang, S.M., Fu, Q., An, L., and Liu, J., *Growth of aligned SWNT arrays from water-soluble molecular clusters for nanotube device fabrication*. Physical Chemistry Chemical Physics, **6**, 1077-1079 (2004).
67. Saito, R., Dresselhaus, G., and Dresselhaus, M.S., *Physics properties of carbon nanotubes*. 1998, London: Imperial College Press.
68. Yudasaka, M., Yamada, R., Sensui, N., Wilkins, T., Ichihashi, T., and Iijima, S., *Mechanism of the effect of NiCo, Ni and Co catalysts on the yield of single-wall carbon nanotubes formed by pulsed Nd : YAG laser ablation*. Journal of Physical Chemistry B, **103**, 6224-6229 (1999).
69. Bower, C., Zhou, O., Zhu, W., Werder, D.J., and Jin, S.H., *Nucleation and growth of carbon nanotubes by microwave plasma chemical vapor deposition*. Applied Physics Letters, **77**, 2767-2769 (2000).
70. Treacy, M.M.J., Ebbesen, T.W., and Gibson, J.M., *Exceptionally high Young's modulus observed for individual carbon nanotubes*. Nature, **381**, 678-680 (1996).
71. Kim, P. and Lieber, C.M., *Nanotube nanotweezers*. Science, **286**, 2148-2150 (1999).
72. Avouris, P., Appenzeller, J., Martel, R., and Wind, S.J., *Carbon nanotube electronics*. Proceedings of the Ieee, **91**, 1772-1784 (2003).
73. Martel, R., Schmidt, T., Shea, H.R., Hertel, T., and Avouris, P., *Single- and multi-wall carbon nanotube field-effect transistors*. Applied Physics Letters, **73**, 2447-2449 (1998).
74. Bachtold, A., Hadley, P., Nakanishi, T., and Dekker, C., *Logic circuits with carbon nanotube transistors*. Science, **294**, 1317-1320 (2001).

References

75. Yao, Z., Postma, H.W.C., Balents, L., and Dekker, C., *Carbon nanotube intramolecular junctions*. Nature, **402**, 273-276 (1999).
76. Javey, A., Guo, J., Wang, Q., Lundstrom, M., and Dai, H.J., *Ballistic carbon nanotube field-effect transistors*. Nature, **424**, 654-657 (2003).
77. Collins, P.C., Arnold, M.S., and Avouris, P., *Engineering carbon nanotubes and nanotube circuits using electrical breakdown*. Science, **292**, 706-709 (2001).
78. Liang, W.J., Shores, M.P., Bockrath, M., Long, J.R., and Park, H., *Kondo resonance in a single-molecule transistor*. Nature, **417**, 725-729 (2002).
79. Derycke, V., Martel, R., Appenzeller, J., and Avouris, P., *Carbon nanotube inter- and intramolecular logic gates*. Nano Letters, **1**, 453-456 (2001).
80. Heinze, S., Tersoff, J., Martel, R., Derycke, V., Appenzeller, J., and Avouris, P., *Carbon nanotubes as Schottky barrier transistors*. Physical Review Letters, **89**, 106801 (2002).
81. Hu, J.T., Ouyang, M., Yang, P.D., and Lieber, C.M., *Controlled growth and electrical properties of heterojunctions of carbon nanotubes and silicon nanowires*. Nature, **399**, 48-51 (1999).
82. McEuen, P.L., Fuhrer, M.S., and Park, H.K., *Single-walled carbon nanotube electronics*. Ieee Transactions on Nanotechnology, **1**, 78-85 (2002).
83. Xia, Y.N., Yang, P.D., Sun, Y.G., Wu, Y.Y., Mayers, B., Gates, B., Yin, Y.D., Kim, F., and Yan, Y.Q., *One-dimensional nanostructures: Synthesis, characterization, and applications*. Advanced Materials, **15**, 353-389 (2003).
84. Baughman, R.H., Zakhidov, A.A., and de Heer, W.A., *Carbon nanotubes - the route toward applications*. Science, **297**, 787-792 (2002).
85. Deheer, W.A., Chatelain, A., and Ugarte, D., *A Carbon Nanotube Field-Emission Electron Source*. Science, **270**, 1179-1180 (1995).
86. Fan, S.S., Chapline, M.G., Franklin, N.R., Tomblor, T.W., Cassell, A.M., and Dai, H.J., *Self-oriented regular arrays of carbon nanotubes and their field emission properties*. Science, **283**, 512-514 (1999).
87. Rinzler, A.G., Hafner, J.H., Nikolaev, P., Lou, L., Kim, S.G., Tomanek, D., Nordlander, P., Colbert, D.T., and Smalley, R.E., *Unraveling Nanotubes - Field-Emission from an Atomic Wire*. Science, **269**, 1550-1553 (1995).
88. Lee, C.J., Lee, T.J., Lyu, S.C., Zhang, Y., Ruh, H., and Lee, H.J., *Field emission from well-aligned zinc oxide nanowires grown at low temperature*. Applied Physics Letters, **81**, 3648-3650 (2002).
89. Bonard, J.M., Salvetat, J.P., Stockli, T., de Heer, W.A., Forro, L., and Chatelain, A., *Field emission from single-wall carbon nanotube films*. Applied Physics Letters, **73**, 918-920 (1998).
90. Zhu, W., Bower, C., Zhou, O., Kochanski, G., and Jin, S., *Large current density from carbon nanotube field emitters*. Applied Physics Letters, **75**, 873-875 (1999).
91. Bonard, J.M., Kind, H., Stockli, T., and Nilsson, L.A., *Field emission from carbon nanotubes: the first five years*. Solid-State Electronics, **45**, 893-914 (2001).
92. Wang, Q.H., Corrigan, T.D., Dai, J.Y., Chang, R.P.H., and Krauss, A.R., *Field emission from nanotube bundle emitters at low fields*. Applied Physics Letters, **70**, 3308-3310 (1997).
93. Dillon, A.C., Jones, K.M., Bekkedahl, T.A., Kiang, C.H., Bethune, D.S., and Heben, M.J., *Storage of hydrogen in single-walled carbon nanotubes*. Nature, **386**, 377-379 (1997).
94. Liu, C., Fan, Y.Y., Liu, M., Cong, H.T., Cheng, H.M., and Dresselhaus, M.S., *Hydrogen storage in single-walled carbon nanotubes at room temperature*. Science, **286**, 1127-1129 (1999).

References

95. Chen, P., Wu, X., Lin, J., and Tan, K.L., *High H₂ uptake by alkali-doped carbon nanotubes under ambient pressure and moderate temperatures*. Science, **285**, 91-93 (1999).
96. Ye, Y., Ahn, C.C., Witham, C., Fultz, B., Liu, J., Rinzler, A.G., Colbert, D., Smith, K.A., and Smalley, R.E., *Hydrogen adsorption and cohesive energy of single-walled carbon nanotubes*. Applied Physics Letters, **74**, 2307-2309 (1999).
97. Zhao, J.J., Buldum, A., Han, J., and Lu, J.P., *Gas molecule adsorption in carbon nanotubes and nanotube bundles*. Nanotechnology, **13**, 195-200 (2002).
98. Baughman, R.H., Cui, C.X., Zakhidov, A.A., Iqbal, Z., Barisci, J.N., Spinks, G.M., Wallace, G.G., Mazzoldi, A., De Rossi, D., Rinzler, A.G., Jaschinski, O., Roth, S., and Kertesz, M., *Carbon nanotube actuators*. Science, **284**, 1340-1344 (1999).
99. Che, G.L., Lakshmi, B.B., Fisher, E.R., and Martin, C.R., *Carbon nanotubule membranes for electrochemical energy storage and production*. Nature, **393**, 346-349 (1998).
100. Frackowiak, E. and Beguin, F., *Carbon materials for the electrochemical storage of energy in capacitors*. Carbon, **39**, 937-950 (2001).
101. Niu, C.M., Sichel, E.K., Hoch, R., Moy, D., and Tennent, H., *High power electrochemical capacitors based on carbon nanotube electrodes*. Applied Physics Letters, **70**, 1480-1482 (1997).
102. Wang, J.X., Li, M.X., Shi, Z.J., Li, N.Q., and Gu, Z.N., *Direct electrochemistry of cytochrome c at a glassy carbon electrode modified with single-wall carbon nanotubes*. Analytical Chemistry, **74**, 1993-1997 (2002).
103. Arico, A.S., Bruce, P., Scrosati, B., Tarascon, J.M., and Van Schalkwijk, W., *Nanostructured materials for advanced energy conversion and storage devices*. Nature Materials, **4**, 366-377 (2005).
104. Wang, J., *Carbon-nanotube based electrochemical biosensors: A review*. ElectroAnalysis, **17**, 7-14 (2005).
105. Wallace, P.R., *The Band Theory of Graphite*. Physical Review, **71**, 622 (1947).
106. McClure, J.W., *Band Structure of Graphite and de Haas-van Alphen Effect*. Physical Review, **108**, 612 (1957).
107. Slonczewski, J.C. and Weiss, P.R., *Band Structure of Graphite*. Physical Review, **109**, 272 (1958).
108. Semenoff, G.W., *Condensed-Matter Simulation of a Three-Dimensional Anomaly*. Physical Review Letters, **53**, 2449 (1984).
109. Ando, T., Fowler, A.B., and Stern, F., *ELECTRONIC-PROPERTIES OF TWO-DIMENSIONAL SYSTEMS*. Reviews Of Modern Physics, **54**, 437-672 (1982).
110. Marder, M.P., *Condensed matter physics*. 2000, New York: John Wiley.
111. Novoselov, K.S., Geim, A.K., Morozov, S.V., Jiang, D., Zhang, Y., Dubonos, S.V., Grigorieva, I.V., and Firsov, A.A., *Electric field effect in atomically thin carbon films*. Science, **306**, 666-669 (2004).
112. Novoselov, K.S., Geim, A.K., Morozov, S.V., Jiang, D., Katsnelson, M.I., Grigorieva, I.V., Dubonos, S.V., and Firsov, A.A., *Two-dimensional gas of massless Dirac fermions in graphene*. Nature, **438**, 197-200 (2005).
113. Zhang, Y.B., Tan, Y.W., Stormer, H.L., and Kim, P., *Experimental observation of the quantum Hall effect and Berry's phase in graphene*. Nature, **438**, 201-204 (2005).
114. Wang, Y.Y., Ni, Z.H., Shen, Z.X., Wang, H.M., and Wu, Y.H., *Interference enhancement of Raman signal of graphene*. Applied Physics Letters, **92**, 043121 (2008).

References

115. de Heer, W.A., Berger, C., Wu, X.S., First, P.N., Conrad, E.H., Li, X.B., Li, T.B., Sprinkle, M., Hass, J., Sadowski, M.L., Potemski, M., and Martinez, G., *Epitaxial graphene*. Solid State Communications, **143**, 92-100 (2007).
116. Hass, J., de Heer, W.A., and Conrad, E.H., *The growth and morphology of epitaxial multilayer graphene*. Journal Of Physics-Condensed Matter, **20**, 323202 (2008).
117. Gall, N.R., Rut'kov, E.V., and Tontegode, A.Y., *Two dimensional graphite films on metals and their intercalation*. International Journal Of Modern Physics B, **11**, 1865-1911 (1997).
118. Oshima, C. and Nagashima, A., *Ultra-thin epitaxial films of graphite and hexagonal boron nitride on solid surfaces*. Journal Of Physics-condensed Matter, **9**, 1-20 (1997).
119. Wintterlin, J. and Bocquet, M.-L., Surface Science, doi:10.1016/j.susc.2008.08.037 (2009).
120. Park, S.J. and Ruoff, R.S., *Chemical methods for the production of graphenes*. Nature Nanotechnology, **4**, 217 (2009).
121. Vaari, J., Lahtinen, J., and Hautajarvi, P., *The adsorption and decomposition of acetylene on clean and K-covered Co(0001)*. Catalysis Letters, **44**, 43-49 (1997).
122. Ueta, H., Saida, M., Nakai, C., Yamada, Y., Sasaki, M., and Yamamoto, S., *Highly oriented monolayer graphite formation on Pt(111) by a supersonic methane beam*. Surface Science, **560**, 183-190 (2004).
123. Starr, D.E., Pazhetnov, E.M., Stadnichenko, A.I., Boronin, A.I., and Shaikhutdinov, S.K., *Carbon films grown on Pt(111) as supports for model gold catalysts*. Surface Science, **600**, 2688-2695 (2006).
124. Gall, N.R., Rut'kov, E.V., and Tontegode, A.Y., *Interaction of silver atoms with iridium and with a two-dimensional graphite film on iridium: Adsorption, desorption, and dissolution*. Physics of the Solid State, **46**, 371-377 (2004).
125. Kawano, T., Kawaguchi, M., Okamoto, Y., Enomoto, H., and Bando, H., *Preparation of layered B/C/N thin films on nickel single crystal by LPCVD*. Solid State Sciences, **4**, 1521-1527 (2002).
126. Madden, H.H., Kupperts, J., and Ertl, G., *Interaction of Carbon-Monoxide with (110) Nickel Surfaces*. Journal of Chemical Physics, **58**, 3401-3410 (1973).
127. Goodman, D.W. and Yates, J.T., *Co Isotopic Mixing Measurements on Nickel - Evidence for Irreversibility of Co Dissociation*. Journal of Catalysis, **82**, 255-260 (1983).
128. Gamo, Y., Nagashima, A., Wakabayashi, M., Terai, M., and Oshima, C., *Atomic structure of monolayer graphite formed on Ni(111)*. Surface Science, **374**, 61-64 (1997).
129. Starodubov, A.G., Medvetskii, M.A., Shikin, A.M., and Adamchuk, V.K., *Intercalation of silver atoms under a graphite monolayer on Ni(111)*. Physics of the Solid State, **46**, 1340-1348 (2004).
130. Sutter, P.W., Flege, J.I., and Sutter, E.A., *Epitaxial graphene on ruthenium*. Nature Materials, **7**, 406-411 (2008).
131. de Parga, A.L.V., Calleja, F., Borca, B., Passeggi, M.C.G., Hinarejos, J.J., Guinea, F., and Miranda, R., *Periodically rippled graphene: Growth and spatially resolved electronic structure*. Physical Review Letters, **1**, 056807 (2008).
132. Marchini, S., Gunther, S., and Wintterlin, J., *Scanning tunneling microscopy of graphene on Ru(0001)*. Physical Review B, **76**, 075429 (2007).
133. Coraux, J., N'Diaye, A.T., Busse, C., and Michely, T., *Structural coherency of graphene on Ir(111)*. Nano Letters, **8**, 565-570 (2008).

References

134. Frank, I.W., Tanenbaum, D.M., Van der Zande, A.M., and McEuen, P.L., *Mechanical properties of suspended graphene sheets*. Journal of Vacuum Science & Technology B, **25**, 2558-2561 (2007).
135. Garcia-Sanchez, D., van der Zande, A.M., Paulo, A.S., Lassagne, B., McEuen, P.L., and Bachtold, A., *Imaging mechanical vibrations in suspended graphene sheets*. Nano Letters, **8**, 1399-1403 (2008).
136. Poot, M. and van der Zant, H.S.J., *Nanomechanical properties of few-layer graphene membranes*. Applied Physics Letters, **92**, 063111 (2008).
137. Schedin, F., Geim, A.K., Morozov, S.V., Hill, E.W., Blake, P., Katsnelson, M.I., and Novoselov, K.S., *Detection of individual gas molecules adsorbed on graphene*. Nature Materials, **6**, 652-655 (2007).
138. Neto, A.H.C., Guinea, F., Peres, N.M.R., Novoselov, K.S., and Geim, A.K., *The electronic properties of graphene*. Reviews Of Modern Physics, **81**, 109-162 (2009).
139. Katsnelson, M.I., Novoselov, K.S., and Geim, A.K., *Chiral tunnelling and the Klein paradox in graphene*. Nature Physics, **2**, 620-625 (2006).
140. Beenakker, C.W.J., *Colloquium: Andreev reflection and Klein tunneling in graphene*. Reviews Of Modern Physics, **80**, 1337-1354 (2008).
141. Stander, N., Huard, B., and Goldhaber-Gordon, D., *Evidence for Klein Tunneling in Graphene p-n Junctions*. Physical Review Letters, **102**, 026807 (2009).
142. Rycerz, A., Tworzydło, J., and Beenakker, C.W.J., *Valley filter and valley valve in graphene*. Nature Physics, **3**, 172-175 (2007).
143. Cresti, A., Grosso, G., and Parravicini, G.P., *Valley-valve effect and even-odd chain parity in p-n graphene junctions*. Physical Review B, **77**, 233402 (2008).
144. Geim, A.K. and Novoselov, K.S., *The rise of graphene*. Nature Materials, **6**, 183-191 (2007).
145. Bolotin, K.I., Sikes, K.J., Jiang, Z., Klima, M., Fudenberg, G., Hone, J., Kim, P., and Stormer, H.L., *Ultrahigh electron mobility in suspended graphene*. Solid State Communications, **146**, 351-355 (2008).
146. Orlita, M., Faugeras, C., Plochocka, P., Neugebauer, P., Martinez, G., Maude, D.K., Barra, A.L., Sprinkle, M., Berger, C., de Heer, W.A., and Potemski, M., *Approaching the Dirac Point in High-Mobility Multilayer Epitaxial Graphene*. Physical Review Letters, **101**, 267601 (2008).
147. Du, X., Skachko, I., Barker, A., and Andrei, E.Y., *Approaching ballistic transport in suspended graphene*. Nature Nanotechnology, **3**, 491-495 (2008).
148. Geim, A.K. and MacDonald, A.H., *Graphene: Exploring carbon flatland*. Physics Today, **60**, 35-41 (2007).
149. Pimenta, M.A., Dresselhaus, G., Dresselhaus, M.S., Cancado, L.G., Jorio, A., and Saito, R., *Studying disorder in graphite-based systems by Raman spectroscopy*. Physical Chemistry Chemical Physics, **9**, 1276-1291 (2007).
150. Reich, S. and Thomsen, C., *Raman spectroscopy of graphite*. Philosophical Transactions of the Royal Society of London Series a-Mathematical Physical and Engineering Sciences, **362**, 2271-2288 (2004).
151. Dresselhaus, M.S. and Eklund, P.C., *Phonons in carbon nanotubes*. Advances in Physics, **49**, 705-814 (2000).
152. Dresselhaus, M.S., Dresselhaus, G., Saito, R., and Jorio, A., *Raman spectroscopy of carbon nanotubes*. Physics Reports-Review Section of Physics Letters, **409**, 47-99 (2005).

References

153. Thomsen, C. and Reich, S., *Double resonant Raman scattering in graphite*. Physical Review Letters, **85**, 5214-5217 (2000).
154. Malard, L.M., Pimenta, M.A., Dresselhaus, G., and Dresselhaus, M.S., *Raman spectroscopy in graphene*. Physics Reports-review Section Of Physics Letters, **473**, 51-87 (2009).
155. Banholzer, M.J., Millstone, J.E., Qin, L.D., and Mirkin, C.A., *Rationally designed nanostructures for surface-enhanced Raman spectroscopy*. Chemical Society Reviews, **37**, 885-897 (2008).
156. Qin, L.D., Zou, S.L., Xue, C., Atkinson, A., Schatz, G.C., and Mirkin, C.A., *Designing, fabricating, and imaging Raman hot spots*. Proceedings of the National Academy of Sciences of the United States of America, **103**, 13300-13303 (2006).
157. Fromm, D.P., Sundaramurthy, A., Kinkhabwala, A., Schuck, P.J., Kino, G.S., and Moerner, W.E., *Exploring the chemical enhancement for surface-enhanced Raman scattering with Au bowtie nanoantennas*. Journal of Chemical Physics, **124**, 061101 (2006).
158. Sawai, Y., Takimoto, B., Nabika, H., Ajito, K., and Murakoshi, K., *Observation of a small number of molecules at a metal nanogap arrayed on a solid surface using surface-enhanced Raman scattering*. Journal of the American Chemical Society, **129**, 1658-1662 (2007).
159. Li, W.Y., Camargo, P.H.C., Lu, X.M., and Xia, Y.N., *Dimers of Silver Nanospheres: Facile Synthesis and Their Use as Hot Spots for Surface-Enhanced Raman Scattering*. Nano Letters, **9**, 485-490 (2009).
160. Wang, Z.H., Liu, J.W., Chen, X.Y., Wan, J.X., and Qian, Y.T., *A simple hydrothermal route to large-scale synthesis of uniform silver nanowires*. Chemistry-a European Journal, **11**, 160-163 (2004).
161. Njoki, P.N., Lim, I.I.S., Mott, D., Park, H.Y., Khan, B., Mishra, S., Sujakumar, R., Luo, J., and Zhong, C.J., *Size correlation of optical and spectroscopic properties for gold nanoparticles*. Journal of Physical Chemistry C, **111**, 14664-14669 (2007).
162. Ayars, E.J., Hallen, H.D., and Jahncke, C.L., *Electric Field Gradient Effects in Raman Spectroscopy*. Physical Review Letters, **85**, 4180 (2000).
163. Mohanty, P., Yoon, I., Kang, T., Seo, K., Varadwaj, K.S.K., Choi, W., Park, Q.H., Ahn, J.P., Suh, Y.D., Ihee, H., and Kim, B., *Simple vapor-phase synthesis of single-crystalline Ag nanowires and single-nanowire surface-enhanced Raman scattering*. Journal of the American Chemical Society, **129**, 9576 (2007).
164. Tsai, D.P., Othonos, A., Moskovits, M., and Uttamchandani, D., *Raman-Spectroscopy Using a Fiber Optic Probe with Subwavelength Aperture*. Applied Physics Letters, **64**, 1768-1770 (1994).
165. Jahncke, C.L., Paesler, M.A., and Hallen, H.D., *Raman Imaging with near-Field Scanning Optical Microscopy*. Applied Physics Letters, **67**, 2483-2485 (1995).
166. Anderson, M.S., *Locally enhanced Raman spectroscopy with an atomic force microscope*. Applied Physics Letters, **76**, 3130-3132 (2000).
167. Kasim, J., Yu, T., You, Y.M., Liu, J.P., See, A., Li, L.J., and Shen, Z.X., *Near-field Raman imaging using optically trapped dielectric microsphere*. Optics Express, **16**, 7976-7984 (2008).
168. Bailo, E. and Deckert, V., *Tip-enhanced Raman scattering*. Chemical Society Reviews, **37**, 921-930 (2008).
169. Pettinger, B., Ren, B., Picardi, G., Schuster, R., and Ertl, G., *Nanoscale probing of adsorbed species by tip-enhanced Raman spectroscopy*. Physical Review Letters, **92**, 096101 (2004).
170. Steidtner, J. and Pettinger, B., *High-resolution microscope for tip-enhanced optical processes in ultrahigh vacuum*. Review of Scientific Instruments, **78**, 103104 (2007).

References

171. Yeo, B.S., Stadler, J., Schmid, T., Zenobi, R., and Zhang, W.H., *Tip-enhanced Raman Spectroscopy - Its status, challenges and future directions*. Chemical Physics Letters, **472**, 1-13 (2009).
172. Maciel, J.M., Jaimes, R., Corio, P., Rubim, J.C., Volpe, P.L., Agostinho, A., and Agostinho, S.M.L., *The characterisation of the protective film formed by benzotriazole on the 90/10 copper-nickel alloy surface in H₂SO₄ media*. Corrosion Science, **50**, 879-886 (2008).
173. Wang, J.J., Smith, D.A., Batchelder, D.N., Saito, Y., Kirkham, J., Robinson, C., Baldwin, K., Li, G., and Bennett, B., *Apertureless near-field Raman spectroscopy*. Journal of Microscopy-Oxford, **210**, 330-333 (2003).
174. Kharintsev, S.S., Hoffmann, G.G., Dorozhkin, P.S., de With, G., and Loos, J., *Atomic force and shear force based tip-enhanced Raman spectroscopy and imaging*. Nanotechnology, **18**, 315502 (2007).
175. Sun, W.X. and Shen, Z.X., *Near-field scanning Raman microscopy using apertureless probes*. Journal of Raman Spectroscopy, **34**, 668-676 (2003).
176. Ren, B., Picardi, G., and Pettinger, B., *Preparation of gold tips suitable for tip-enhanced Raman spectroscopy and light emission by electrochemical etching*. Review of Scientific Instruments, **75**, 837-841 (2004).
177. Wang, X., Liu, Z., Zhuang, M.D., Zhang, H.M., Wang, X., Xie, Z.X., Wu, D.Y., Ren, B., and Tian, Z.Q., *Tip-enhanced Raman spectroscopy for investigating adsorbed species on a single-crystal surface using electrochemically prepared Au tips*. Applied Physics Letters, **91**, 101105 (2007).
178. Anderson, N., Hartschuh, A., and Novotny, L., *Chirality changes in carbon nanotubes studied with near-field Raman spectroscopy*. Nano Letters, **7**, 577-582 (2007).
179. Kim, Z.H. and Leone, S.R., *High-resolution apertureless near-field optical imaging using gold nanosphere probes*. Journal of Physical Chemistry B, **110**, 19804-19809 (2006).
180. Anderson, N., Bouhelier, A., and Novotny, L., *Near-field photonics: tip-enhanced microscopy and spectroscopy on the nanoscale*. Journal of Optics a-Pure and Applied Optics, **8**, S227-S233 (2006).
181. Zhang, C., Abdijalilov, K., and Grebel, H., *Surface enhanced Raman with anodized aluminum oxide films*. Journal of Chemical Physics, **127**, 044701 (2007).
182. Catalin, C.N., Jens, D., Nicolas, B., and Markus, B.R., *Scanning-probe Raman spectroscopy with single-molecule sensitivity*. Physical Review B (Condensed Matter and Materials Physics), **73**, 193406 (2006).
183. Pettinger, B., *Tip-enhanced Raman spectroscopy (TERS)*, in *Surface-Enhanced Raman Scattering: Physics and Applications*. 2006. p. 217-240.
184. Nieman, L.T., Krampert, G.M., and Martinez, R.E., *An apertureless near-field scanning optical microscope and its application to surface-enhanced Raman spectroscopy and multiphoton fluorescence imaging*. Review of Scientific Instruments, **72**, 1691-1699 (2001).
185. Baykul, M.C., *Preparation of sharp gold tips for STM by using electrochemical etching method*. Materials Science and Engineering B-Solid State Materials for Advanced Technology, **74**, 229-233 (2000).
186. Ditlbacher, H., Hohenau, A., Wagner, D., Kreibig, U., Rogers, M., Hofer, F., Aussenegg, F.R., and Krenn, J.R., *Silver nanowires as surface plasmon resonators*. Physical Review Letters, **95**, 257403 (2005).

References

187. Christiansen, S.H., Becker, M., Fahlbusch, S., Michler, J., Sivakov, V., Andra, G., and Geiger, R., *Signal enhancement in nano-Raman spectroscopy by gold caps on silicon nanowires obtained by vapour-liquid-solid growth*. Nanotechnology, **18**, 035503 (2007).
188. Hutchison, J.A., Centeno, S.P., Odaka, H., Fukumura, H., Hofkens, J., and Uji-i, H., *Subdiffraction Limited, Remote Excitation of Surface Enhanced Raman Scattering*. Nano Letters, **9**, 995-1001 (2009).
189. Zeisel, D., Deckert, V., Zenobi, R., and Vo-Dinh, T., *Near-field surface-enhanced Raman spectroscopy of dye molecules adsorbed on silver island films*. Chemical Physics Letters, **283**, 381-385 (1998).
190. Lee, S.J., Guan, Z.Q., Xu, H.X., and Moskovits, M., *Surface-enhanced Raman spectroscopy and nanogeometry: The plasmonic origin of SERS*. Journal of Physical Chemistry C, **111**, 17985-17988 (2007).
191. Chen, J.N., Martensson, T., Dick, K.A., Deppert, K., Xu, H.Q., Samuelson, L., and Xu, H.X., *Surface-enhanced Raman scattering of rhodamine 6G on nanowire arrays decorated with gold nanoparticles*. Nanotechnology, **19**, 275712 (2008).
192. Tang, Z.Y. and Kotov, N.A., *One-dimensional assemblies of nanoparticles: Preparation, properties, and promise*. Advanced Materials, **17**, 951-962 (2005).
193. Chen, J.Y., Wiley, B.J., and Xia, Y.N., *One-dimensional nanostructures of metals: Large-scale synthesis and some potential applications*. Langmuir, **23**, 4120-4129 (2007).
194. Chen, Y., Wang, C.G., Ma, Z.F., and Su, Z.M., *Controllable colours and shapes of silver nanostructures based on pH: application to surface-enhanced Raman scattering*. Nanotechnology, **18**, 325602 (2007).
195. Graff, A., Wagner, D., Ditlbacher, H., and Kreibitz, U., *Silver nanowires*. European Physical Journal D, **34**, 263-269 (2005).
196. Ma, G.H., Tang, S.H., Sun, W.X., Shen, Z.X., Huang, W.M., and Shi, J.L., *Size-dependent excited state properties of US nanocrystals*. Physics Letters A, **299**, 581-585 (2002).
197. Balan, L., Malval, J.P., Schneider, R., and Burget, D., *Silver nanoparticles: New synthesis, characterization and photophysical properties*. Materials Chemistry and Physics, **104**, 417-421 (2007).
198. Zhang, J.H., Liu, H.Y., Wang, Z.L., and Ming, N.B., *Shape-selective synthesis of gold nanoparticles with controlled sizes, shapes, and plasmon Resonances*. Advanced Functional Materials, **17**, 3295-3303 (2007).
199. Wiley, B., Sun, Y.G., Chen, J.Y., Cang, H., Li, Z.Y., Li, X.D., and Xia, Y.N., *Shape-controlled synthesis of silver and gold nanostructures*. MRS Bulletin, **30**, 356-361 (2005).
200. Wiley, B., Sun, Y.G., Mayers, B., and Xia, Y.N., *Shape-controlled synthesis of metal nanostructures: The case of silver*. Chemistry-a European Journal, **11**, 454-463 (2005).
201. Huo, Z., Tsung, C., Huang, W., Zhang, X., and Yang, P., *Sub-Two Nanometer Single Crystal Au Nanowires*. Nano Lett., 2041-2044 (2008).
202. Feng, H.J., Yang, Y.M., You, Y.M., Li, G.P., Guo, J., Yu, T., Shen, Z.X., Wu, T., and Xing, B.G., *Simple and rapid synthesis of ultrathin gold nanowires, their self-assembly and application in surface-enhanced Raman scattering*. Chemical Communications, 1984-1986 (2009).
203. Sun, W.X., Shen, Z.X., Cheong, F.C., Yu, G.Y., Lim, K.Y., and Lin, J.Y., *Preparation of cantilevered W tips for atomic force microscopy and apertureless near-field scanning optical microscopy*. Review of Scientific Instruments, **73**, 2942-2947 (2002).

References

204. Motohashi, M., Hayazawa, N., Tarun, A., and Kawata, S., *Depolarization effect in reflection-mode tip-enhanced Raman scattering for Raman active crystals*. Journal of Applied Physics, **103**, 034309 (2008).
205. Michota, A. and Bukowska, J., *Surface-enhanced Raman scattering (SERS) of 4-mercaptobenzoic acid on silver and gold substrates*. Journal of Raman Spectroscopy, **34**, 21-25 (2003).
206. Pettinger, B., Domke, K.F., Zhang, D., Schuster, R., and Ertl, G., *Direct monitoring of plasmon resonances in a tip-surface gap of varying width*. Physical Review B, **76**, 113409 (2007).
207. Nottingher, I. and Elfick, A., *Effect of sample and substrate electric properties on the electric field enhancement at the apex of SPM nanotips*. Journal of Physical Chemistry B, **109**, 15699-15706 (2005).
208. Anderson, N., Anger, P., Hartschuh, A., and Novotny, L., *Subsurface Raman imaging with nanoscale resolution*. Nano Letters, **6**, 744-749 (2006).
209. Saito, R., Fujita, M., Dresselhaus, G., and Dresselhaus, M.S., *Electronic structure of chiral graphene tubules*. Applied Physics Letters, **60**, 2204-2206 (1992).
210. Hiura, H., Ebbesen, T.W., Fujita, J., Tanigaki, K., and Takada, T., *ROLE OF SP(3) DEFECT STRUCTURES IN GRAPHITE AND CARBON NANOTUBES*. Nature, **367**, 148-151 (1994).
211. Bockrath, M., Hone, J., Zettl, A., McEuen, P.L., Rinzler, A.G., and Smalley, R.E., *Chemical doping of individual semiconducting carbon-nanotube ropes*. Physical Review B, **61**, R10606 (2000).
212. Miwa, R.H., Orellana, W., and Fazzio, A., *Substrate-dependent electronic properties of an armchair carbon nanotube adsorbed on H/Si(001)*. Applied Physics Letters, **86**, 213111 (2005).
213. Mota, F.D. and de Castilho, C.M.C., *Carbon nanotube adsorbed on a hydrogenated Si-rich beta-SiC(100) (3X2) surface: First-principles pseudopotential calculations*. Physical Review B, **74**, 165408 (2006).
214. Peng, G.W., Huan, A.C.H., Liu, L., and Feng, Y.P., *Structural and electronic properties of 4 angstrom carbon nanotubes on Si(001) surfaces*. Physical Review B, **74**, 235416 (2006).
215. Mews, A., Koberling, F., Basche, T., Philipp, G., Duesberg, G.S., Roth, S., and Burghard, M., *Raman imaging of single carbon nanotubes*. Advanced Materials, **12**, 1210-1214 (2000).
216. Hiura, H., Ebbesen, T.W., Tanigaki, K., and Takahashi, H., *Raman studies of carbon nanotubes*. Chemical Physics Letters, **202**, 509-512 (1993).
217. Miwa, R.H., Orellana, W., and Fazzio, A., *Carbon nanotube adsorbed on hydrogenated Si(001) surfaces*. Applied Surface Science, **244**, 124-128 (2005).
218. Oron-Carl, M., Hennrich, F., Kappes, M.M., Lohneysen, H.V., and Krupke, R., *On the electron-phonon coupling of individual single-walled carbon nanotubes*. Nano Letters, **5**, 1761-1767 (2005).
219. Maultzsch, J., Reich, S., Schlecht, U., and Thomsen, C., *High-energy phonon branches of an individual metallic carbon nanotube*. Physical Review Letters, **91**, 087402 (2003).
220. Brown, S.D.M., Jorio, A., Corio, P., Dresselhaus, M.S., Dresselhaus, G., Saito, R., and Kneipp, K., *Origin of the Breit-Wigner-Fano lineshape of the tangential G-band feature of metallic carbon nanotubes*. Physical Review B, **63**, 155414 (2001).
221. Olego, D. and Cardona, M., *Pressure-Dependence of Raman Phonons of Ge and 3c-Sic*. Physical Review B, **25**, 1151-1160 (1982).

References

222. Windl, W., Karch, K., Pavone, P., Schutt, O., Strauch, D., Weber, W.H., Hass, K.C., and Rimai, L., *2nd-Order Raman-Spectra of Sic - Experimental and Theoretical Results from Ab-Initio Phonon Calculations*. Physical Review B, **49**, 8764-8767 (1994).
223. Burton, J.C., Sun, L., Long, F.H., Feng, Z.C., and Ferguson, I.T., *First- and second-order Raman scattering from semi-insulating 4H-SiC*. Physical Review B, **59**, 7282-7284 (1999).
224. Frechette, J. and Carraro, C., *Resolving radial composition gradients in polarized confocal Raman spectra of individual 3C-SiC nanowires*. Journal of the American Chemical Society, **128**, 14774-14775 (2006).
225. Duesberg, G.S., Loa, I., Burghard, M., Syassen, K., and Roth, S., *Polarized Raman spectroscopy on isolated single-wall carbon nanotubes*. Physical Review Letters, **85**, 5436-5439 (2000).
226. Li, D. and Kaner, R.B., *Materials science - Graphene-based materials*. Science, **320**, 1170-1171 (2008).
227. Han, M.Y., Ozyilmaz, B., Zhang, Y.B., and Kim, P., *Energy band-gap engineering of graphene nanoribbons*. Physical Review Letters, **98**, 206805 (2007).
228. Son, Y.W., Cohen, M.L., and Louie, S.G., *Half-metallic graphene nanoribbons*. Nature, **444**, 347-349 (2006).
229. Yang, L., Cohen, M.L., and Louie, S.G., *Excitonic effects in the optical spectra of graphene nanoribbons*. Nano Letters, **7**, 3112-3115 (2007).
230. Moghaddam, A.G. and Zareyan, M., *Graphene-based superconducting quantum point contacts*. Applied Physics a-Materials Science & Processing, **89**, 579-585 (2007).
231. Han, M., Ozyilmaz, B., Zhang, Y., Jarillo-Herero, P., and Kim, P., *Electronic transport measurements in graphene nanoribbons*. Physica Status Solidi B-Basic Solid State Physics, **244**, 4134-4137 (2007).
232. Meyer, J.C., Geim, A.K., Katsnelson, M.I., Novoselov, K.S., Booth, T.J., and Roth, S., *The structure of suspended graphene sheets*. Nature, **446**, 60-63 (2007).
233. Ishigami, M., Chen, J.H., Cullen, W.G., Fuhrer, M.S., and Williams, E.D., *Atomic structure of graphene on SiO₂*. Nano Letters, **7**, 1643-1648 (2007).
234. Kittel, C., *Introduction to Solid State Physics, 8th Edition*. 2004: Wiley.
235. Yu, Q.K., Lian, J., Siriponglert, S., Li, H., Chen, Y.P., and Pei, S.S., *Graphene segregated on Ni surfaces and transferred to insulators*. Applied Physics Letters, **93**, 113103 (2008).
236. Ferrari, A.C., Meyer, J.C., Scardaci, V., Casiraghi, C., Lazzeri, M., Mauri, F., Piscanec, S., Jiang, D., Novoselov, K.S., Roth, S., and Geim, A.K., *Raman spectrum of graphene and graphene layers*. Physical Review Letters, **97**, 187401 (2006).
237. Cancado, L.G., Reina, A., Kong, J., and Dresselhaus, M.S., *Geometrical approach for the study of G band in the Raman spectrum of monolayer graphene, bilayer graphene, and bulk graphite*. Physical Review B, **77**, 245408 (2008).
238. Bunch, J.S., van der Zande, A.M., Verbridge, S.S., Frank, I.W., Tanenbaum, D.M., Parpia, J.M., Craighead, H.G., and McEuen, P.L., *Electromechanical resonators from graphene sheets*. Science, **315**, 490-493 (2007).
239. Ni, Z.H., Wang, H.M., Kasim, J., Fan, H.M., Yu, T., Wu, Y.H., Feng, Y.P., and Shen, Z.X., *Graphene thickness determination using reflection and contrast spectroscopy*. Nano Letters, **7**, 2758-2763 (2007).

References

- 240. Cancado, L.G., Pimenta, M.A., Neves, B.R.A., Dantas, M.S.S., and Jorio, A., *Influence of the Atomic Structure on the Raman Spectra of Graphite Edges*. Physical Review Letters, **93**, 247401 (2004).
- 241. Ozyilmaz, B., Jarillo-Herrero, P., Efetov, D., Abanin, D.A., Levitov, L.S., and Kim, P., *Electronic transport and quantum hall effect in bipolar graphene p-n-p junctions*. Physical Review Letters, **99**, 166804 (2007).